



Virginia Commonwealth University
VCU Scholars Compass

Theses and Dissertations

Graduate School

2019

Metal Nanoparticle Synthesis by Photochemical Reduction with a High-Intensity Focused Laser Beam

Victoria K. Meader
Virginia Commonwealth University

Follow this and additional works at: <https://scholarscompass.vcu.edu/etd>

 Part of the [Physical Chemistry Commons](#)

© Victoria Kathryn Meader

Downloaded from

<https://scholarscompass.vcu.edu/etd/6001>

This Thesis is brought to you for free and open access by the Graduate School at VCU Scholars Compass. It has been accepted for inclusion in Theses and Dissertations by an authorized administrator of VCU Scholars Compass. For more information, please contact libcompass@vcu.edu.

VIRGINIA COMMONWEALTH UNIVERSITY

MASTER'S THESIS

**METAL NANOPARTICLE SYNTHESIS BY
PHOTOCHEMICAL REDUCTION WITH A
HIGH-INTENSITY FOCUSED LASER BEAM**

Author: *Victoria Kathryn Meader*

Supervisor: *Dr. Katharine Moore
Tibbetts*

*A thesis submitted in fulfillment of the requirements
for the degree of Master of Science*

in the

**Tibbetts' Group
Department of Chemistry**

August 6, 2019



Declaration of Authorship

I, Victoria Kathryn MEADER, declare that this thesis titled, “Metal Nanoparticle Synthesis by Photochemical Reduction with a High-Intensity Focused Laser Beam” and the work presented in it are my own. I confirm that:

- This work was done wholly or mainly while in candidature for a research degree at this University.
- Where any part of this thesis has previously been submitted for a degree or any other qualification at this University or any other institution, this has been clearly stated.
- Where I have consulted the published work of others, this is always clearly attributed.
- Where I have quoted from the work of others, the source is always given. With the exception of such quotations, this thesis is entirely my own work.
- I have acknowledged all main sources of help.
- Where the thesis is based on work done by myself jointly with others, I have made clear exactly what was done by others and what I have contributed myself.

Signed: Victoria Kathryn Meader

Date: 20190806

“Why not start over, though? Time is going to keep going anyway, why not spend it working toward something that might make you happy?”

My mom, giving me the permission I didn’t know I needed to go back to school at 24.

$A + B \rightarrow C$

The reaction of A and B yields C

$A \wedge B \rightarrow C$

A, and if B then C

VIRGINIA COMMONWEALTH UNIVERSITY

Abstract

Dr. Katharine Moore TIBBETTS

Department of Chemistry

Master of Science

Metal Nanoparticle Synthesis by Photochemical Reduction with a High-Intensity Focused Laser Beam

by Victoria Kathryn MEADER

Colloidal, metallic nanoparticles have myriad applications, but they are most ideal when they are monodisperse, and demonstrate maximum catalytic utility when they are small (< 5 nm) and uncoated; because their surface area is accessible and maximized. Laser-assisted metal nanoparticle synthesis is a 'green' method that has become a topic of active research because it is able to produce uncoated or 'naked' products. The nanoparticles in this work are formed through the reduction of metal salts in aqueous solutions, but the reducing agent is an electron-dense microplasma generated by the laser pulse interacting with the media. Because no chemical reducing agents or stabilizers are needed, the products have no surfactants.

The underlying reaction mechanisms that drive this type of synthesis are generally understood, however, there is insufficient detail that would allow control over the formation of ultimate product morphologies and size distributions. The metals examined in this thesis are gold, whose formation follows an autocatalytic rate law, and silver, whose formation follows a first-order rate law. Through my research, I was able to explore the effects that physical parameters, such as laser pulse settings, and chemical parameters, such as radical scavenger addition, have on laser-assisted gold or silver nanoparticle synthesis. My research, outlined in this thesis, is therefore focused on elucidating such details and distilling them into methods of control in order to better predict and tune nanoparticle products.

First, I examined the effects of laser pulse duration and pulse energy on the formation mechanisms of gold nanoparticles. The reducing species formed in femtosecond laser-generated optical breakdown plasma directly control the kinetics of $[\text{AuCl}_4]^-$ reduction to form gold nanoparticles. Optical breakdown plasma contains free electrons, the primary reducing agents of $[\text{AuCl}_4]^-$; and hydroxyl radicals that recombine to form H_2O_2 , which drives the autocatalytic growth of gold nanoparticles. The formation rates of both free electrons and H_2O_2 are both dependent on the energy and duration of laser pulses over the experimental ranges of pulse energies (10–2400 μJ) and pulse durations (30–1500 fs). For laser pulse energies $\leq 600 \mu\text{J}$, at all pulse durations, the first-order rate constant, k_1 , was directly proportional to the theoretically calculated plasma volume, where the electron density surpasses the threshold value of $1.8 \times 10^{20} \text{ cm}^{-3}$. The second-order rate constant, k_2 , correlates with the measured H_2O_2 formation rate at all pulse energies and durations, resulting in the empirical relationship $k_2 \sim \text{H}_2\text{O}_2^{0.5}$.

Next, these results were applied to the formation of silver nanoparticles, whose reduction is hindered by one of the side-products formed during irradiation of water. Although H_2O_2 formed from optical breakdown is one of the key driving forces behind the reduction of gold ions, it back-oxidizes silver. To address this, we added a radical scavenger to our media in an attempt to compensate for the mechanisms blocking the formation of silver nanoparticles. In this project, we sought to control the hydroxyl-radical chemistry in femtosecond-laser generated plasma by adding liquid ammonia. Irradiating liquid ammonia solutions resulted in a reaction between NH_3 and $OH\cdot$, forming peroxyxynitrite, $ONOO^-$, and ultimately reduced amount of H_2O_2 generated. The liquid ammonia concentration directly affected Ag^+ reduction, forming 12.7 ± 4.9 nm silver nanoparticles at the optimal, 1 mM ammonia concentration.

Finally, using the results from the ammonia study, we applied the same ideas to the reduction of gold ions into nanoparticles to see how the chemical manipulation of the reducing species formed by the laser would affect the gold reduction mechanism. The reduction kinetics of gold follows an autocatalytic rate law, which is governed by rate constants: nucleation rate k_1 , dependent on e_{aq}^- ; and growth rate k_2 , dependent on the $OH\cdot$ recombination product, H_2O_2 . The hydroxyl radical scavengers used in this project were isopropyl alcohol and sodium acetate. Higher scavenger concentrations lowered k_2 values and produced smaller gold nanoparticles, as predicted. At the optimal concentration of 10 mM isopropyl alcohol (which was better of the two scavengers), the average particle diameter was 3.78 nm (PDI = 0.071). The equivalent surface area-normalized catalytic activity of the gold nanoparticles synthesized in the presence and absence of scavengers indicates that they do not coat the nanoparticle surfaces.

We were able to demonstrate control over final product morphologies by manipulating the generation of reducing species that contribute to different steps of metal ion reduction into nanoparticles. By optimizing size distributions and particle shapes, we managed to also show that our colloidal products remain stable and catalytically efficient for months after synthesis.

Acknowledgements

First I want to thank Dr. Katharine Moore Tibbetts for advising me and providing a lab environment that fosters collaboration, inquisitiveness, and transparency. Thank you to VCU's Chemistry Department for all the resources I've had access to; including the feedback, advice, and assistance of the faculty and my graduate peers, as well as the opportunity to mentor and teach undergraduate students. Thank you to VCU's Philosophy department, particularly Professor Ellis, for making me the thorough and logical person I am, even though it turned out to not mix as well with science as I had initially anticipated. Thank you wholeheartedly to the office of Student Accessibility and Educational Opportunity at VCU for making it possible for me to pursue this dream at all, and to all the professors who didn't treat my accommodations like an inconvenience.

Thank you in advance to my committee members, Drs. Bertino, Bratko, Lucas, and Tibbetts for their patience and understanding regarding my philosophy-brain and tolerance of the fact that I decided to put footnotes in this thesis which is not a conventionally chemistry-thing to do as far as I am aware.

I am grateful to my labmates and the friends I've made in the program for helping me not fail out of all my classes outright, keeping me encouraged, not letting me feel like an idiot, watching music videos with me, and playing Dungeons & Dragons with me.

Finally I want to thank my family. My mom and my little sister, Livi, have been paying my tuition, rent, and bills ever since I lost my stipend. My best friends, Laura, Evangeline, and Mallory have been making sure I've been taking care of myself properly. My family has supported and believed in me, and without that, I would probably be dead instead of defending my Master's thesis. I love them all very much.

Contents

Declaration of Authorship	i
Abstract	iii
Acknowledgements	v
1 Introduction	1
1.1 Background	1
1.2 Femtosecond Lasers	2
1.3 Objectives	3
AuNPs	3
AgNPs	3
2 Methods	5
2.1 Materials	5
Sample Preparation	5
2.2 Instrumentation	5
Experimental Setup	6
2.3 Procedures	7
2.3.1 Beam Settings	7
Microplasma Measurements	8
2.3.2 Catalysis	9
2.3.3 Hydrogen Peroxide Quantification	9
Radical Scavenger Effectiveness	10
3 Theory	11
3.1 Laser Pulse and Aqueous Media Interactions	11
3.1.1 Supercontinuum Emission	12
3.1.2 Optical Breakdown	13
3.2 Photoreduction Kinetics	17
3.2.1 Gold	17
Nucleation and Autocatalytic Growth	19
3.2.2 Silver	20
3.3 Experimental Parameters	21
3.3.1 Focus	21
High-NA Tight-Focus	22
3.3.2 pH	25
3.3.3 Hydroxyl Radical Scavengers	25
4 Pulse Study	27
4.1 Laser Parameters	27
4.1.1 Pulse Energy, Pulse Duration, and Intensity	27
Experimental Variables	27

4.2	Results	28
4.2.1	Products	30
4.3	Discussion	33
4.3.1	Nucleation	33
4.3.2	Autocatalytic Growth	34
	Beam-Focus and Size-Distribution	34
4.4	Summary	35
5	Radical Scavenger Studies	37
5.1	Silver	37
5.1.1	Ammonia	37
5.1.2	Results	38
	Irradiation of Ammonia Solutions	38
	AgNP Products	40
5.1.3	Discussion	41
	Peroxydinitrite Experiments	42
	Kinetics	43
5.1.4	Summary	45
5.2	Gold	45
5.2.1	Acetate and Isopropyl Alcohol	45
5.2.2	Results	46
	Reduction Kinetics	46
	AuNP Products	47
	Catalysis	50
5.2.3	Discussion	51
	Hydrogen Peroxide	51
	Scavenging Mechanism of Acetate	51
	Scavenging Mechanism of Isopropyl Alcohol	53
5.2.4	Summary	53
6	Conclusions	54
6.0.1	Pulse-Settings Experiments	54
6.0.2	Solution Experiments: Scavengers	55
	Silver	55
	Gold	55
6.1	Implications and Future Studies	56
A	Beam Parameters	57
A.1	Measurement of Pulse Duration (FROG)	57
A.2	Focusing Geometry	57
A.2.1	Electron Density Modeling	59
B	Hydrogen Peroxide Quantification	61
B.1	Quantification of H ₂ O ₂	61
C	AuNP: Laser Parameters	63
C.1	Calculation of the Time-Dependent Concentration of [AuCl ₄] ⁻	63
D	Hydroxyl Scavenging: Silver	66
D.1	Liquid Ammonia	66
E	Hydroxyl Scavenging: Gold	69

E.1 Additional TEMs	69
E.2 XPS Data	72
E.3 Rate Summaries	73
E.4 Catalytic Data	74
E.5 Hydrogen Peroxide	75
E.6 Solution-pH Effects	75
Bibliography	76

List of Figures

2.1	Illustration of the experimental high-NA laser setup and in situ UV-vis configuration.	6
2.2	OB and SCE measurements across focusing-geometries.	8
3.1	Illustration of self-focusing in an optical medium.	12
3.2	Generalized illustration of optical breakdown.	14
3.3	Spatial and temporal dependence of electron density generation.	16
3.4	Water irradiation with different beam-focusing	17
3.5	Explanation of AuNP Finke-Watzky kinetics	19
3.6	OB and SCE measurement data with tightly-focused setup.	21
3.7	Electron density as a function of time, across a range of pulse durations	23
3.8	Properties of electron density in the focused setup.	24
4.1	Graphical illustration of intensity-dependence on pulse energy and duration.	28
4.2	In situ AuNP plasmon growth spectra.	29
4.3	Kinetic plots.	29
4.4	Final spectra of AuNPs.	30
4.5	TEM images and histograms.	31
4.6	Effect of pulse energy on Finke-Watzky rates.	32
4.7	Rate constant k_1 and plasma volume.	33
4.8	Rate constant k_2 and H_2O_2 formation.	34
4.9	TEM images illustrating the effect of beam-focus on AuNP size distributions.	35
5.1	AgNP plasmon growth kinetics.	38
5.2	Quantification of hydrogen peroxide in water and in ammonia solution.	39
5.3	Absorbance spectra of liquid ammonia during irradiation.	40
5.4	Ammonia concentration optimization.	40
5.5	TEM images of AgNP product morphologies resulting from different ammonia concentrations.	41
5.6	Absorption spectra of nitrogen species.	43
5.7	Spectra comparison: $AgClO_4$ and $AgNO_3$	44
5.8	Fractional AuNP growth vs irradiation time, in IPA and acetate.	46
5.9	UV-vis spectra of AuNPs synthesized with IPA or acetate.	47
5.10	TEM images, histograms, and mass-weighted distributions of AuNPs synthesized in IPA.	48
5.11	TEM images, histograms and mass-weighted distributions of AuNPs synthesized in acetate solution.	49
5.12	XPS Au 4f peak spectra for AuNPs synthesized with and without radical scavengers.	50
5.13	Catalytic data for AuNPs synthesized in IPA or acetate.	51
5.14	Hydrogen peroxide formation in acetate and IPA solutions.	52
A.1	Frequency-Resolved Optical Gating.	58

A.2	Illustration of the Gaussian beam's geometric components.	58
A.3	Beam radius as a function of propagation distance.	59
A.4	CCD photos of microplasma in cuvette.	59
A.5	Photoionization rate as a function of peak intensity, in water.	60
A.6	Peak electron density as a function of propagation distance.	60
B.1	Titanium(IV) sulfate calibration curve.	61
B.2	Comparison of H ₂ O ₂ quantifications.	62
C.1	Isolation of [AuCl ₄] ⁻ precursor spectrum.	64
C.2	Gold salt vanishing concentrations.	64
C.3	Additional TEM images of AuNP products.	65
D.1	Comparison of irradiated AgNO ₃ and AgClO ₄ samples.	66
D.2	Irradiated NH ₃ solutions, with and without Ag.	67
D.3	A TEM image of AgNPs formed in 0.25 mM ammonia solution.	68
D.4	A TEM image of AgNPs formed in 1 mM ammonia solution.	68
D.5	A TEM image of AgNPs formed in 10 mM ammonia solution.	68
E.1	TEM images of AuNPs synthesized in IPA solution.	69
E.2	TEM images of AuNPs synthesized in optimal, 10 mM IPA solution.	70
E.3	TEM images and histograms of AuNPs synthesized in KCl solutions.	72
E.4	Fixed-pH experiments; AuNPs synthesized in IPA solution.	75

List of Tables

3.1	Reported laser focusing conditions and resulting AuNP sizes. Particles generally become more monodisperse as the focus is tightened.	22
4.1	Pulse durations τ_p , energies E_p , and calculated peak irradiance I	27
4.2	Values of rate constant k_1 from eq 3.19. Units are s^{-1}	30
4.3	Values of rate constant k_2 from eq 3.19. Units are $mM^{-1} s^{-1}$	30
5.1	Proposed reactions, rate constants, and references for photolysis of water and ammonia.	42
6.1	Summary of MNP products.	54
D.1	Solution pH and fractional concentrations of H_2O_2 for different liquid ammonia-containing precursors.	66
D.2	Silver NP SPR growth kinetics, k	67
D.3	AgNP SPR growth kinetics for $AgClO_4$ and $AgNO_3$, with and without NH_3	67
E.1	Average particle dimensions obtained from Gaussian function-fitting to size distributions of AuNPs synthesized with IPA.	70
E.2	Average particle dimensions obtained from log-normal function-fitting to size distributions of AuNPs synthesized with IPA.	71
E.3	Average particle dimensions obtained from Gaussian function-fitting to size-distributions of AuNPs synthesized with acetate.	71
E.4	Average particle dimensions obtained from log-normal function-fitting to size-distributions of AuNPs synthesized with acetate.	71
E.5	Average particle dimensions obtained from Gaussian function-fitting to size-distributions of AuNPs synthesized with KCl.	71
E.6	Average particle dimensions obtained from log-normal function-fitting to size-distributions of AuNPs synthesized with KCl.	71
E.7	XPS binding energy and atomic percent data of various Au species.	72
E.8	XPS atomic percent data for AuNP samples.	72
E.9	Kinetic data associated AuNP formation in IPA solutions.	73
E.10	Kinetic data associated AuNP formation in acetate solutions.	73
E.11	Kinetic data associated with AuNP formation in KCl solutions.	73
E.12	Catalytic data associated with AuNPs synthesized in IPA.	74
E.13	Catalytic data associated with AuNPs synthesized in acetate.	74
E.14	Fractional H_2O_2 generated in the presence of IPA or acetate.	75

List of Abbreviations

AgNP	silver nanoparticle
AuNP	gold nanoparticle
CCD	charge-coupled device
e_{aq}^-	hydrated or water-solvated electrons
FROG	frequency-resolved optical gating
fwhm	full width at half-maximum
IC	ion chromatography
IPA	isopropyl alcohol
LDP	low-density plasma
LMCT	ligand-to-metal charge transfer
LPR	laser photochemical reduction
MNP	metal nanoparticle
NA	numerical aperture
NLO	nonlinear optics
NPs	nanoparticles
OB	optical breakdown
PAP	<i>p</i> -aminophenol
PDI	polydispersity index
PLAL	pulsed laser ablation in liquid
PNP	<i>p</i> -nitrophenol
ROS	reactive oxygen species
SCE	supercontinuum emission
SERS	surface-enhanced Raman spectroscopy
SPR	surface plasmon resonance
SSTF	simultaneous spatial- and temporal-focusing

Physical Constants

speed of light in vacuum	$c_0 = 2.997\,924\,58 \times 10^8 \text{ m s}^{-1}$ (exact)
electron volt	$\text{eV} = 1.6 \times 10^{-19} \text{ J}$
electron mass	$m_e = 9.109\,383\,56 \times 10^{-31} \text{ kg}$
electron charge	$e = 1.602\,176\,62 \times 10^{-19} \text{ C}$
refractive index of water	$n_0 = 1.33$
water molecule mass	$M = 18.02 \text{ amu}$
permittivity constant	$\epsilon = 8.85 \times 10^{-12} \text{ F m}^{-1}$
exciton	$m = 0.5 m_e$ (approximate)
reduced planck constant	$\hbar = h/2\pi$

Simulation Values

beam wavelength	$\lambda = 800 \text{ nm}$
beam waist	$w_0 = 6.52 \text{ }\mu\text{m}$
Rayleigh range	$z_R = 7.77 \times 10^{-3} \text{ cm}$
recombination rate	$w_{\text{rec}} = 2 \times 10^{-9} \text{ cm}^3 \text{ s}^{-1}$
electron density/OB threshold	$\rho_e = 1.8 \times 10^{-20} \text{ cm}^{-3}$
band gap	$\Delta = 6.5 \text{ eV}$
time between collisions	$\tau_c = 1.7 \text{ fs}$

List of Symbols

P	power	$\text{W (J s}^{-1}\text{)}$
I	intensity (peak irradiance)	W cm^{-1}
τ_p	pulse duration	fs
E_p	pulse energy	J
τ	completion time	s
ρ_e	electron density	cm^{-3}
Δ	band gap	eV
γ	Keldysh adiabaticity parameter	(ratio)
ω	center laser frequency	rad s^{-1}
ω_t	electron tunneling frequency	rad s^{-1}
n_2	Kerr nonlinear refractive index	$\text{m}^{-2} \text{W}^{-1}$
n	total index of refraction	
c/n	beam propagation speed	m s^{-1}
\bar{x}	sample mean	
R^2	coefficient of determination	ideal = 1
Φ	Dawson integral	$e^{-x^2} \int_0^x e^{t^2} dt$

Rate Constants

k_1	Finke-Watzky nucleation	s^{-1}
k_2	Finke-Watzky autocatalytic growth	M s^{-1}
k	AgNP formation	s^{-1}
k_g	peak (400 nm) growth	s^{-1}
k_d	peak (400 nm) decay	s^{-1}
k_{Au}	moles Au normalized	$\text{s}^{-1} \mu\text{mol}^{-1}$
k_{app}	apparent catalytic	s^{-1}
k_{SSA}	surface area normalized	$\text{L s}^{-1} \text{m}^{-2}$
W_{photo}	photoionization rate	$\text{cm}^{-3} \text{s}^{-1}$
W_{casc}	cascade ionization rate	s^{-1}
W_{MPI}	multiphoton ionization rate	s^{-1}
W_{tun}	tunnel ionization rate	s^{-1}
W_{diff}	diffusion rate	s^{-1}
W_{rec}	recombination rate	$\text{cm}^3 \text{s}^{-1}$

Chapter 1

Introduction

1.1 Background

The macroscale characteristics of nanomaterials rely on their nanoscale properties, such as shape, dispersity, diameter, and mass. Metallic nanoparticles have myriad potential applications because of their tunable optical properties [1–4]. This optical activity is a consequence of the collective oscillations of surface conduction-band electrons that surround each individual nanoparticle. Gold nanoparticle (AuNP) spheres, for example, absorb a distinct and narrow range of the visible spectrum. This oscillating ‘electron cloud’ is called the localized *surface plasmon resonance* (SPR)¹, and its nanoparticle size- and shape-dependence opens a plethora of practical applications including *surface-enhanced Raman spectroscopy* (SERS) [5]; non-invasive diagnostic imaging [2]; biosensing [5, 6]; photothermal cancer therapy [3, 7]; drug delivery [8]; and catalytic reactions such as water-splitting [9–11]. In many ways similar to gold, silver is biocompatible, and silver nanoparticles (AgNPs) have a distinct SPR band that falls in the visible spectrum; but silver also has anti-microbial properties. This combination of qualities has motivated silver nanoparticle development, including the incorporation of silver nanostructures into medical devices [12–14]. Colloidal silver’s competitive optical properties also make it a more cost-effective SERS substrate-option than gold [15, 16].

Monodisperse nanoparticles are ideal. For catalytic purposes, *sub*-5 nm spherical AuNPs are particularly useful because a significant fraction of atoms have low-coordination on the particle surface, improving catalytic activity [17–21]. Many applications (such as catalysis) also require direct access to the nanoparticle surface. Nanoparticles are often synthesized using benchtop methods. To achieve small particle sizes, many wet-chemical synthetic methods incorporate organic surfactants and capping agents [22–26]. These methods allow a considerable degree of control over product-development, and yield relatively small, monodisperse, *protected* AuNPs [27–29]. However, these products are surface-passivated and unsuitable for biomedical [30] or catalytic [31] applications until ligand-exchange or removal procedures are performed. Surfactant-removal and motility processes involve multiple time-consuming steps, and often require the use of more organic solvents, which are frequently toxic [32–34]. They also require thermal or oxidative measures that change the physical properties of the AuNPs [35, 36].

Sufficiently energetic laser pulses are capable of producing high-energy reagents through their interactions with aqueous media. These photochemical reagents can reduce metal ions, synthesizing nanoparticles while entirely avoiding the need to add organic reducing

¹The frequency of electron-cloud oscillation determines the SPR absorbance band.

agents, capping agents, or surfactants. Ultrafast laser-assisted nanoparticle synthesis is capable of producing uncoated, ‘naked’ particles while also saving time and materials.

1.2 Femtosecond Lasers

Interactions between femtosecond-laser pulses and condensed media² induce nonlinear optical phenomena³; through which other applications may be achieved, including: white light lasers [37], remote optical sensing [38, 39], nanostructure writing onto solid surfaces [40, 41], and cellular nanosurgery [42–44]. Laser-energy deposition starts with the generation of a concentrated, weakly-ionized plasma [44–48], causing white-light-producing *supercontinuum emission* (SCE), cavitation-bubble formation in the medium through *optical breakdown* (OB), or often both [49, 50]. These plasmas are generated through a process called photolysis⁴, which energetically breaks apart the solvent molecules and produces high-energy reducing species. It is through these laser-generated energetic reducing species that metal nanoparticle (MNP) synthesis is driven.

Two approaches to colloidal AuNP-synthesis using laser-assisted methods are common. The first is bulk-metal ablation, in which the laser beam is focused onto a metal target, and metal atoms are etched off, to subsequently consolidate and form nanoparticles [51]. One of the most popular variations of this technique is *pulsed laser ablation in liquid* (PLAL), which involves irradiating a metal target immersed in solvent to generate plasma, vapor, and metal micro- or nano-sized droplets, which can further react with the liquid medium to form NPs [52, 53]. Size-control is *somewhat* achievable with PLAL by modifying laser fluence, changing the solvent [54], introducing salts [51, 55, 56], using successive laser fragmentation step treatments [57, 58], or adding surfactants [59–61]. However, high product dispersity is a problem. Despite the popularity of PLAL, it is difficult to avoid organic additives, and colloids are typically very polydisperse [52, 56]. It is possible to reduce AuNP polydispersity with post-synthesis laser fragmentation [58, 62], but a laser wavelength resonant with the AuNP SPR frequency ($\lambda \sim 520$ nm) is required.

The *second method* is direct photochemical reduction of metal-salts in solution, sometimes referred to as *laser photochemical reduction* (LPR) [53]. By irradiating a metal-salt *solution*, reducing agents are created using solvent-molecule photolysis which drives nanoparticle formation [24, 63]. The experiments in this thesis are all performed using this method. The primary advantage of laser-assisted photochemical reduction synthesis is that it can achieve ‘pure’ nanoparticles, which are free of surfactants. Despite the clear drawbacks of organic additives, they are most direct method for product control during traditional NP synthesis. However, product-tuning without direct chemical stop-and-go mechanisms can be exerted in the context of photochemical reduction synthesis. Control can even be achieved chemically; through the modification of conditions like metal-ion concentration, pH, or the addition of other species to the precursor solution that will influence synthesis chemistry without coating the products [2, 22, 63–65]. Morphology and

²This is a physics term loosely denoting materials that are in a solid or liquid state.

³It is difficult to find definitions of this term that explain the phenomena without self-referencing, or which don’t just sound like a definition of general spectroscopy. Briefly, *nonlinear optical phenomena* (NLO) is the effect of disproportionate output relative to initial input, of an ‘intense’ light, as it is passed through a medium. The medium is definitionally nonlinear by virtue of the fact that initial and final light-related measurements (which might be something like frequency, amplitude, etc.) are disproportionate; or have not changed in a way that a linear equation would predict. ‘Intense’ usually refers to an electric field with a magnitude on the order of 1×10^8 V m⁻¹. It can also be defined as processes requiring simultaneous interaction with more than one photon.

⁴Photolysis is a compound word comprised of ‘photo’ meaning *light*, and ‘lysis’ meaning *loosening*.

size-dispersity can also be influenced **physically**—laser parameters such as the **focusing-geometry**, pulse durations, and beam energies all affect outcomes [23–26, 62, 66–73]. Because of the heavy reliance of many practical applications on SPR absorbance, it is pivotal to any nanoparticle synthesis method that the dimensional product outcomes are controllable and predictable [74, 75].

1.3 Objectives

My work in Dr. Tibbetts' lab was focused on determining strategies to more clearly understand and steer MNP synthesis, by manipulating their formation kinetics during photoreduction. I will outline three key experiments performed; the first (Chapter 4) was oriented around the effects of the laser beam itself on the solution chemistry. The metal used in this experiment was gold, which we will return to in the second part of Chapter 5. After examining the physical parameters, we looked at some of the chemical parameters. In Section 5.2, we sought to address the issue of silver oxidation in the presence of H_2O_2 .

Outline I want to start as simply as possible and expand into the more complex ideas. Therefore, the next chapter is the **methods** section, where I will explain the chemical materials and procedures, the physical instrumentation and setups used, and our measurement and characterization techniques. After that I will elaborate on **theory**: physical and chemical experimental parameters like the focus-geometry and precursor solution pH influence the nature of the laser-generated microplasma, which influences the reduction kinetics of metal ions, determining the properties of the nanoparticle products. In the theory section I will first explain the mechanisms of laser-assisted NP formation, then I will cover the details of microplasma generation, and finally, I will discuss the effects that beam-focus and solution pH have on microplasma generation. After that, I will move on to the content chapters, which will discuss and analyze experimental results.

AuNPs

The photoreduction of $Au^{3+} \rightarrow AuNPs$ follows a **two-step mechanism**, in which each step is governed by a different laser-generated **reducing agent**. Because there are two **distinct** rate laws and each is governed by a separate species, we looked to the specific effects that the laser beam had on the production of these species. If by changing the beam parameters we are able to selectively favor or suppress some of the high-energy reagents that drive Au^{3+} reduction, then we should at minimum improve our understanding of the interactions between these rate laws and product morphologies. Hydrogen peroxide (H_2O_2) is a byproduct of high-intensity laser beam propagation in water; it fuels the **second step** of AuNP formation and is a species whose control might allow further control over AuNP product sizes.

AgNPs

Silver ions reduce to AgNPs following a single-step rate law. However, a byproduct of water photolysis is H_2O_2 , which **oxidizes** silver atoms, degrading AgNPs and regenerating salt concentrations in solution during irradiation. To address this shortcoming, we add hydroxyl-radical **scavengers** to our precursor solutions and inhibit H_2O_2 formation. By

varying the concentration of our scavenger, we hope to optimize our product outcomes and better understand the radical chemistry that occurs during irradiation of silver solutions. Furthermore, H_2O_2 is a contributor to Au^{3+} reduction. By adding hydroxyl radical scavengers to precursor gold solutions we seek to develop a chemical strategy to edit AuNP formation kinetics as well.

Chapter 2

Methods

2.1 Materials

All materials were used as received, without further purification. Metal salts used were potassium tetrachloroaurate(III) (Strem Chemicals), silver perchlorate (Fisher), and silver nitrate (Acros). Potassium hydroxide, HPLC-grade water, sodium nitrite, potassium nitrate, hydrogen peroxide (30%, Fisher), sulfuric acid, isopropyl alcohol, and sodium oxalate were all obtained from Fisher Scientific. The potassium permanganate and sodium acetate are from Alfa Aesar, the ammonia solution (32%) is from Emplura, titanium dioxide was from Sigma Aldrich. Both stock and working solutions were made using Milli-Q filtered water ($18 \text{ M}\Omega \text{ cm}^{-1}$).

Sample Preparation

Working solutions were prepared from stock solutions. Solutions containing gold were prepared 18–24 h before use, stored in the dark at 6°C , and allowed to warm to room temperature before experiments were performed. Silver metal solutions were prepared directly in cuvettes prior to irradiation.

Gold solutions all contained 0.1 mM KAuCl_4 and 0.35 mM KOH . The pH of these working gold solutions was measured to confirm that it was in the range of 5.3 ± 0.2 [63]. The gold solutions used in radical scavenger experiments involving IPA ($\text{CH}_3\text{CHOHCH}_3$) and acetate (CH_3COO^-)—Chapter 5 contained 0.1 mM KAuCl_4 , concentrations of either sodium acetate or IPA ($0.1\text{--}100 \text{ mM}$) and enough KOH to keep pH within 6.7 ± 0.2 . Silver precursor solutions used in Chapter 5 contained 0.1 mM Ag^+ , as either AgNO_3 or AgClO_4 , and ammonia ($0\text{--}20 \text{ mM}$). Synthesis of peroxyxynitrite (ONOO^-) was adapted from [76], in which 0.58 M NaNO_2 was added to a stirring solution of $0.31 \text{ M H}_2\text{O}_2$ and $0.15 \text{ M H}_2\text{SO}_4$, followed by immediate addition of 2.5 M KOH .

2.2 Instrumentation

Laser irradiation was performed using a titanium-sapphire-based chirped-pulse amplifier (Astrella, Coherent, Inc., Santa Clara, CA, USA) delivering 7 mJ , 30 fs pulses with bandwidth centered at 800 nm at a 1 kHz repetition rate¹. Beam power was measured with a PM10V1 Thermopile power sensor connected to a Coherent FieldMate power meter.

¹Pulse repetition rate describes the number of pulses the laser emits each second. This is relevant because it affects the intensity calculations. The power is read by a meter that can only register the average power per

Experimental Setup

The laser beam exits an external compressor with a diameter of 11 mm ($1/e^2$), and is enlarged to $D = 29$ mm ($1/e^2$) before being focusing with a $f = 50$ mm aspheric lens² (Figure 2.1a). The resulting focal-geometry is $f/1.7$, similar to the tightest focusing condition reported by Liu et al. [49] with a microscope objective; and it is tighter than other reported Gaussian beam focusing-geometries [77, 78]. The beam waist (w_0) and Rayleigh range (z_R) in air were measured with a CCD³ camera (ThorLabs, Inc.) to be $w_0 = 6.52$ μm and $z_R = 77.7$ μm (Appendix A). The focusing conditions correspond to a geometric numerical aperture⁴ ($\text{NA} = n \sin \arctan(D/2f) = 0.37$ in water and a Gaussian beam $\text{NA} = w_0/z_R = 0.084$). This is a high-NA focus. Using known pulse energies and pulse durations (summarized in Table 4.1 in Chapter 4), the peak irradiance at the focus (discounting losses and plasma-induced defocusing in front of the focus [49, 50, 79]) are calculable, and range from $I = 2.5 \times 10^{13}$ W cm^{-2} when $\tau_p = 1500$ fs and the beam energy is $E_p = 50$ μJ ; to $I = 6.0 \times 10^{16}$ W cm^{-2} when $\tau_p = 30$ fs and $E_p = 2400$ μJ .

Metal precursors were allowed to convert to NPs, therefore irradiation times varied according to each experimental condition set. Completion time ranged between 60 and 3600 s, and complete conversion could be confirmed with optical absorption spectra by checking the local SPR for continuing absorption changes. Reaction kinetics were observable in situ because our experiments were all performed in a home-built UV-vis spectrometer—with a stabilized deuterium-tungsten light source (Ocean Optics, DH2000-BAL), optical fibers, two pairs of off-axis parabolic mirrors, and a compact spectrometer (Ocean Optics, HR4000). This rig is illustrated in Figure 2.1. Solutions were processed in 3 mL volumes, in $10 \times 10 \times 40$ mm quartz fluorescence cuvettes.

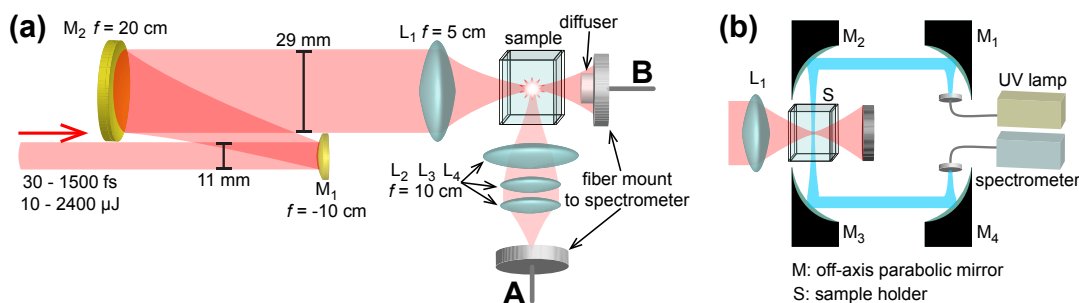


FIGURE 2.1: Experimental beam setup (a) and home-built in situ UV-vis cuvette holder (b).

Ultraviolet–Visible Spectroscopy (UV-vis). A second deuterium-tungsten lamp UV-vis (Ocean Optics, DH2000-DUV) was used to monitor H_2O_2 quantification and catalysis

second, so it will register 7 mJ pulses as being equivalent to 7 W ($7 \frac{\text{J}}{\text{s}}$)—because 1000 of them are delivered in a second.

² The word ‘lens’ is derived from the latin word meaning ‘lentil’. An *aspheric* lens is convex on the side that receives incoming light, and flat on the outgoing side. Aspheric lenses correct for some chromatic aberrations, allowing a tighter focal-spot. The symbol f indicates the focal length, the distance from the lens where the light converges into the focal point.

³Charge-Coupled Device

⁴Numerical aperture ($\text{NA} = n \sin \theta$ where n is the refractive index of the environment and θ is the maximum workable angle) is a relative descriptor of the number of angles at which light can enter or exit a lens (or other optical pathway). For a gaussian beam, $\text{NA} \approx \lambda_0/\pi w_0$ where λ_0 is the beam wavelength in vacuum.

experiments, consisting of a sample holder for $10 \times 10 \times 40$ mm cuvettes placed on a stir plate, and a compact spectrometer (Ocean Optics, USB4000) connected with optical fibers. Spectra were recorded once per 1.2 s using LabVIEW software (National Instruments).

Transmission Electron Microscopy (TEM). Nanoparticles were visualized using TEM (JEOL JEM-1230 TEM) at 120 kV. The colloidal AuNPs were drop-casted onto carbon-coated grid (Ted Pella, Inc.) and left to dry for a minimum of 24 h. Average sizes and size-distributions of the samples were measured using ImageJ software, which referenced a minimum of 500 particles from images taken from three separate areas of the TEM grid.

Ion Chromatography (IC). The chromatographic equipment consisted of a DIONEX ICS-1000 ion chromatogram, coupled to a mass spectrometer. Chromatographic separations were carried out using an AS14A column (maintained at 30 °C) and an AS14 guard column running through a AERS 500 4 mm suppressor. The eluent was 8 mM aqueous sodium bicarbonate and 1 mM aqueous sodium carbonate; the flow rate was 1.2 L/min, and the injection volume was 0.5 μ L. All measurements were performed at room temperature.

X-Ray Photoelectron Spectroscopy (XPS). Spectra in Chapter 5 were collected on a PHI VersaProbe III Scanning XPS Microprobe with a monochromated Al $K\alpha$ X-ray source (1486.6 eV) and a pass energy of 50 eV. Charge neutralization was done by running an ion gun and a flood gun during sample analysis. The measurement spot diameter was 0.5 mm. Spectra were analyzed and deconvoluted using CasaXPS employing Gaussian and Lorentzian convolutions to fit the line profiles. All spectra were corrected using a C 1s peak-shift to center at 284.8 eV.

2.3 Procedures

2.3.1 Beam Settings

For the experiments in Chapter 4, the pulse energy, E_p , was varied from 10 to 2400 μ J using a zero-order $\lambda/2$ waveplate (ThorLabs, Inc.) and broadband thin-film polarizer (Altechna); and, when necessary, a dispersion-compensated 90:10 (R:T)⁵ beamsplitter (Newport, Inc.) to reach $E_p \leq 300$ μ J. The linear chirp⁶ of the laser pulse was controlled by detuning the compressor grating from its zero-dispersion position ($\tau_p = 30$ fs) to produce positive- and negative-chirped 200 fs, and negative-chirped 750 and 1500 fs pulses. In the experiments investigating *chemical* parameters (Chapter 5), the pulse energy was set to $E_p = 1000$ μ J, and the pulse duration to $\tau_p = 30$ fs. All pulse durations were measured by Frequency Resolved Optical Gating [80] (Figure A.1).

⁵R:T means Reflection/Transmission. A 90:10 beamsplitter will reflect 90% of incoming light, and transmit the remaining 10%.

⁶Chirped pulse amplification is a technique for boosting ultrafast laser pulse power. It describes frequency-ordering within a pulse: negative or down-chirped pulses contain faster frequencies before slower frequencies; and positive chirp or up-chirped pulses start with slow frequencies and end with faster frequencies. When our pulse is at its shortest, there is no chirp—the pulse is too compressed and the frequency remains constant.

To quantify the roles of plasma-generated reducing species—hydrated electrons (e_{aq}^-) and H_2O_2 —in driving the photochemical reduction of $[\text{AuCl}_4]^- \rightarrow \text{AuNPs}$, Chapter 4 investigates the effects of the femtosecond-laser E_p and τ_p on the reduction kinetics of $[\text{AuCl}_4]^-$. For this investigation, it is critical to *minimize* the generation of SCE-produced white-light filaments in the medium [49], which cause intensity-clamping and limit the concentration of reactive species in the focal region [25, 81]. As discussed in Section 3.3.1, SCE filamentation in aqueous media, which disperses plasma density, can be restricted by using a tight-focusing geometry obtained with large numerical aperture [49], *simultaneous spatial- and temporal-focusing* (SSTF) [82], or spatial beam shaping [41, 83]. Both tight-focusing [24, 67] and SSTF with pulse-stretching to 36 ps [22, 25, 63–65] have been used for this purpose in previous studies of femtosecond laser-induced $[\text{AuCl}_4]^-$ reduction. In our experiments, we use a tight-focusing geometry for filamentation-prevention, because it affords easy and continuous adjustment to the pulse durations.

Microplasma Measurements

To illustrate the conditions in which OB, SCE, or both are present, both tightly-focused pulses and unfocused, collimated pulses were measured using the setup in Figure 2.2a. The results and implications are discussed in greater detail in Section 3.3.1. Emission spectra from the laser in water were collected with the compact spectrometer at position (i) for OB, and position (ii) for SCE [37, 49].

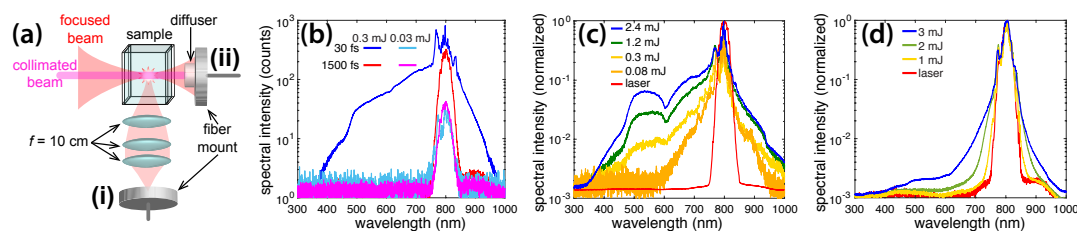


FIGURE 2.2: (a) Setup for OB and SCE measurements. (b) OB spectra for tightly focused 30 fs and 1500 fs pulses. (c) SCE spectra for tightly focused 30 fs pulses. (d) SCE spectra for collimated 30 fs pulses.

Because OB forms an *opaque* plasma that scatters the incident laser radiation, it can be detected by the presence of light scattered perpendicular to the direction of beam propagation. Therefore, the fiber mount position (i) is at a 90° angle to the laser beam [49]. A series of lenses was used to focus the light into the fiber mount. For SCE detection, the fiber mount is placed along the beam path at position (ii), behind the sample; and a diffuser is attached to the fiber mount to avoid saturating the spectrometer, and self-phase modulation associated with SCE can be detected through its white-light output. Figure 2.2b shows spectra obtained at detector (i) for tightly-focused 30 fs and 1500 fs pulses at 0.3 mJ and 0.03 mJ pulse energy. The broadened spectrum for 30 fs pulses indicates the presence of both SCE and OB, while the narrow spectrum with 1500 fs pulses indicates that no SCE occurs. Figure 2.2c,d shows evidence of SCE with 30 fs pulses across a range of pulse energies, for both tightly-focused and collimated pulses. Under both conditions, asymmetric broadening towards the visible region of the spectrum grows with increasing pulse energy. The spectral broadening saturates for tightly-focused pulses at energies above 1.2 mJ (Figure 2.2c), while greater pulse-energies would be needed to saturate the spectral width for the unfocused beam (Figure 2.2d). No OB is observed when the beam is collimated, indicating that an LDP with $\rho_e \sim 10^{18} \text{ cm}^{-3}$ is present in the filaments

(Section 3.1.1) [84, 85]. LDP conditions have been used by research groups to synthesize AuNPs [60, 62, 72, 86]; however, for all the experiments in this thesis, a **tightly-focused geometry** was used.

2.3.2 Catalysis

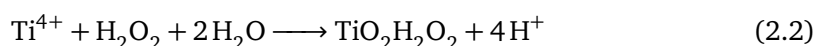
The model catalytic reaction involving *p*-nitrophenol (PNP) reduction by sodium borohydride (NaBH₄) is a common way to test the efficiency of AuNPs [87]. The product, *p*-aminophenol (PAP), is (virtually⁷) only achieved with an MNP catalyst, according to



Catalysis is reliant on access to active sites on the metal nanoparticle surface, therefore it is more efficient when the MNP surface area is maximized. Smaller nanoparticles with good size dispersions will perform well, but their efficiency will obviously decrease if they agglomerate over time. Experimental working solutions made directly in cuvettes, immediately before each trial, contained 0.1 mM PNP (from a stock solution) and 10 mM NaBH₄ (prepared in fresh, 50 mM batches immediately before each reaction). Working solutions totaling 3 mL contained 0.1 mM PNP, 10 mM NaBH₄, and were made directly in cuvettes. For each experiment, these solution-filled cuvettes were placed in the UV-vis sample-holder where data recording was started, and then 500 μL of freshly-irradiated colloidal AuNPs were added to the sample with constant stirring (i.e. the cuvettes were prepared with everything except for the NP catalyst, and data collection immediately before the addition of MNPs). Data-collection was stopped when the absorption peak-decay of the *p*-nitrophenolate ion (400 nm) stopped and remained stationary for 30 s.

2.3.3 Hydrogen Peroxide Quantification

For all of our experiments, it was necessary to confirm the presence of hydrogen peroxide, or to in some way quantify the amount of H₂O₂ produced in the OB plasma. The method we used to accomplish this [88–90] was titanium(IV) sulfate titration⁸, following the equation



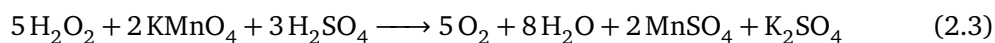
in which titanium(IV) sulfate (Ti⁴⁺) reacts with H₂O₂, yielding a yellow solution of per-titanic acid. The saturation of yellow color in solution is directly related to the H₂O₂ content; therefore the concentration of H₂O₂ can be quantified by measuring solution absorbance at 407 nm. These concentrations are calculated using a calibration curve, which was created by titrating varying concentrations from a hydrogen peroxide stock solution (itself standardized by a titrated KMnO₄ solution [89], which had been standardized via titration using weighed amounts of sodium oxalate [90]) against a fixed concentration of titanium(IV) sulfate solution. This quantification method was adapted primarily from ref [88]. The UV-vis spectra of the different solutions are in Appendix B, Figure B.1. The titanium sulfate solution was synthesized by dissolving TiO₂ in concentrated H₂SO₄ over heat for 16 h.

⁷Strictly speaking, the reaction will proceed without a catalyst; but we'll all be dead by the time it finishes.

⁸It isn't exactly a titration, but a calibration curve was constructed and using this curve we were able to determine concentrations of added H₂O₂ solutions.

After the titanium(IV) sulfate had been calibrated against the standardized H_2O_2 solution, any H_2O_2 produced from irradiation could be quantified. Three milliliter volumes of distilled water were irradiated for 180 s in cuvettes, over the range of laser pulse conditions used in Chapter 4 ($E_p = 2400, 1200, 600, 300,$ and $150 \mu\text{J}$; and $\tau_p = 30, 200, 750,$ and 1500 fs). Once the water was irradiated, 0.4 mL titanium(IV) sulfate (25 mM) was added to the cuvette, mixed, and the solution absorbance at 407 nm was measured. The data are reported and discussed in Section 4.3. Each laser condition set was measured in triplicate.

A second method for H_2O_2 quantification was also implemented for the sake of comparison. It involved titration with KMnO_4 [89]. The same condition sets as used in the first quantification method were used again in triplicate with 3 mL volumes of distilled water. Immediately after termination of laser-irradiation, 0.1 mL H_2SO_4 (2 M) was added to the cuvette, and KMnO_4 was stirred in dropwise until the endpoint was signified when solution maintained a light-pink color.



The KMnO_4 was prepared by dissolving KMnO_4 into deionized water, and was standardized by titrating with pre-weighed solid sodium oxalate stocks as a reference standard, following the procedure in ref [90]. The data from this method was compared to the data from the titanium(IV) sulfate quantification method, to confirm that these H_2O_2 concentrations were reliable (Appendix B).

Radical Scavenger Effectiveness

Experiments testing the amount of H_2O_2 produced in the OB plasma in solutions containing different concentrations of ammonia (0–600 mM) were also performed. The ammonia samples were made directly into each cuvette from a stock, and immediately irradiated for 60 to 600 s to determine how much hydrogen peroxide is able to form. When irradiation was complete, 400 μL of 25 mM titanium(IV) sulfate was added to the cuvette, and the absorption spectrum was recorded. Hydrogen peroxide production as a function of laser energy and pulse duration is discussed in Section 4.3. To quantify the scavenging activity of IPA and acetate, the same $\text{Ti}(\text{SO}_4)_2$ calibration method was used. Aqueous solutions of each scavenger (acetate and IPA) were irradiated for 180 s, and the resulting concentrations of H_2O_2 formed in each sample were calculated from the UV-vis absorption spectra according to a calibration curve. The details for these two scavengers are in Appendix E, Table E.14.

Chapter 3

Theory

3.1 Laser Pulse and Aqueous Media Interactions

Water photolysis is crucial to the photochemical reduction of $[\text{AuCl}_4]^-$ and other metal salts [22, 24, 25, 63, 66–68, 70, 72, 73, 91], and occurs when water is irradiated with high-intensity femtosecond laser pulses [22, 24, 92]. There are two commonly-proposed mechanisms that explain aqueous $[\text{AuCl}_4]^-$ reduction to Au^0 under high-intensity laser irradiation. These mechanisms are (1) direct homolysis of the Au-Cl bonds by multiphoton absorption to form Au^{2+} and Au^+ intermediates, and (2) chemical reduction of Au^{3+} ions by the reactive species formed from water photolysis [22, 63, 66, 67, 69, 72]. The second mechanism is more likely to occur in aqueous solutions where water molecules exponentially outnumber $[\text{AuCl}_4]^-$ molecules. The reactions involved in the photolysis of water include [73, 92–97]



In a dielectric medium¹ with a band gap exceeding laser photon-energy, ultrashort laser pulses can produce quasi-free electrons² in the conduction band by two processes: (1) nonlinear multiphoton ionization and tunneling photoionization [98], and (2) high-kinetic-energy free electron collisions with neutral molecules, causing cascade (or avalanche) ionization [45]. The formation of free electrons generates a local, weakly-ionized plasma [44, 45, 48], which can then initiate OB, SCE, or both [37, 49, 99].

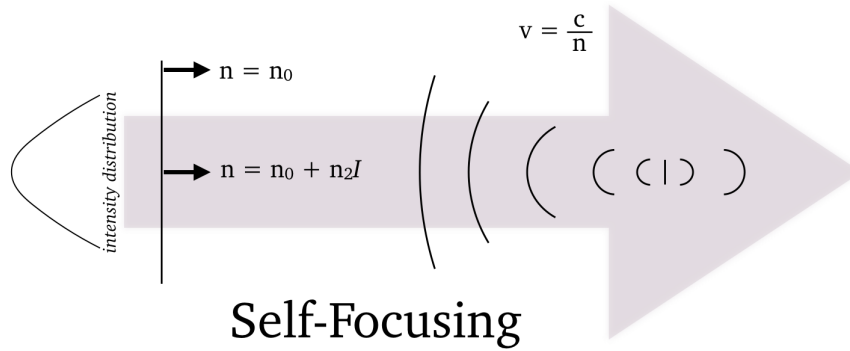


FIGURE 3.1: A diagram adapted from ref [100] where the propagating beam is shown in 'slices'. Due to the Kerr effect, the middle portion of the beam moves more slowly, so as the beam propagates it curls in on itself until it forms a new focal point before the actual focal point. This is the basis of filamentation and intensity-clamping.

3.1.1 Supercontinuum Emission

SCE is produced by the Kerr effect³—induced self-focusing and subsequent filamentation in a nonlinear medium [37, 49, 99, 100]. Self-focusing, and therefore filamentation, depends on the laser power, P , and initiates when P exceeds the critical power P_{crit} [101]

$$P_{\text{crit}} = \frac{3.77\lambda^2}{8\pi n_0 n_2} \quad (3.7)$$

where λ is the laser's wavelength, n_0 is the refractive index of the medium, and n_2 is the nonlinear Kerr coefficient [100]. In water, P_{crit} has been measured at 4.2×10^6 W for 800 nm pulses [102], which translates to very low pulse energies of 0.13 and 0.42 μJ at 30 and 100 fs. The interactions that occur in the medium during filamentation cause self-phase modulation, resulting in spectral broadening to both the red and blue direction of the center laser wavelength. Self-phase modulation in nonlinear media is caused by temporal variance in n_0 [100]. Redshift is caused by rotational and vibrational motion of the molecules in the medium, and a blueshift happens when the power P is high enough to form a shockwave at the trailing temporal edge of each pulse [37]. Blueshifts produce a broad pedestal as far as 400 nm in the output-spectrum for pulses shorter than 100 fs [37, 49, 60, 62, 69, 73, 99] (see also Figure 2.2). Because SCE depends on power instead of

¹A dielectric material is something that's 'insulating' in the sense that it doesn't readily allow energy to escape from it, but not necessarily electrically resistant. When an electric field is applied to it, the atoms within the material polarize readily and energy is able to flow in (or out) and be stored (or removed). It's a material that is manipulable by electric field influence, such that some energy can be transferred within the field, but not so structurally lax that it will allow all the energy-input to escape.

²Free electrons in condensed media are actually quasi-free electrons. They behave similarly to free charge particles, but strictly speaking they are not unbound by surrounding forces.

³The Kerr effect is an optical phenomenon describing the generation of an electric field by an intense beam of light. The variation of intensity across the wavefront of the beam causes a corresponding variation in propagation speed. Beam propagation speed is c/n where c is the speed of light in a vacuum and n is the refractive index. The refractive index at the edge of the beam is $n = n_0$, and at the center region of the beam where the Gaussian intensity-distribution is highest, the refractive index is $n = n_0 + n_2 I$; where n_0 is the refractive index of the medium, n_2 is the nonlinear Kerr coefficient, I is the local intensity, and $n_2 I$ represents the Kerr nonlinear index of refraction. The center region moves more slowly than the the edges of the wavefront, curling the beam inward on itself until it self-focuses.

peak intensity⁴, filamentation may occur at intensities below the OB threshold; especially when the laser beam is weakly-focused or collimated [37, 49, 60, 84, 85, 99, 103, 104]. For laser beams with peak-intensities on the order of 10^{12} W cm⁻², the filament electron-density has been measured at $1 - 3 \times 10^{18}$ cm⁻³ [84, 85]. Such weakly-ionized SCE plasmas can drive $[\text{AuCl}_4]^-$ reduction even in the absence of OB [62, 72, 73], while the white light from the SCE has been shown to induce AuNP-fragmentation through resonant absorption and Coulomb explosion⁵ [60, 103, 104].

3.1.2 Optical Breakdown

Optical breakdown of a medium occurs when free-electron density (ρ_e) in plasma exceeds a critical value. This density generates through the interactions of ultrashort laser pulses with a transparent, dielectric medium that has a band gap whose energy exceeds the energy of the photons. Depending on the peak intensity I of the excitation pulses, quasi-free electrons can be produced in the conduction band, forming an opaque plasma and cavitation bubbles when the free-electron density exceeds the critical OB threshold of $\rho_e \sim 10^{18} - 10^{21}$ cm⁻³ [43–48].

Conventionally, the laser pulse propagates in the z direction. The focusing conditions are largely what determines the parameters of the time-dependent Gaussian intensity envelope [105, 106]

$$I(z, t) = \frac{P(t, z)}{A_z} = \frac{E_p}{\tau_p \pi w_z^2} \exp \left[(-4 \ln 2) \left(\frac{t - z/c}{\tau_p} \right)^2 \right] \quad (3.8)$$

where E_p is the pulse energy, τ_p is the pulse duration, and c is the speed of light. The beam waist w_z (at position z) modeled on the propagation of a Gaussian beam

$$w_z = w_0 \sqrt{1 + \frac{z^2}{z_R^2}} \quad (3.9)$$

where w_0 is the beam waist (the radius at its narrowest point) is the at the focal point, and z_R is the Rayleigh range. These quantities were measured to be $w_0 = 6.52 \times 10^{-4}$ cm and $z_R = 7.77 \times 10^{-3}$ cm for our focusing conditions (Section 2.2 and Figure A.3). To calculate the electron density resulting from the laser–medium interaction, media are typically modeled as dielectric with band gap Δ . The band gap of water is $\tilde{\Delta} = 6.5$ eV [44, 46–48, 106, 107], although some recent experiments have placed the effective band gap as high as 9.5 eV for direct excitation into the conduction band [108, 109]. The effective⁶ ionization potential $\tilde{\Delta}$ must account for the oscillation energy of the electron caused by the intense laser electric field [98],

$$\tilde{\Delta} = \Delta + \frac{e^2 E^2}{4m\omega^2} \quad (3.10)$$

⁴In some cases, pulse duration and intensity do correlate with the presence of SCE, however, isolated SCE is a product of filamentation, which is independent of intensity as evident in eq 3.7.

⁵Coulomb explosion is a phenomenon where a mass of particles becomes uniformly charged to the point where the repulsion force between particles overcomes the strength of the bonds that keep the particles together.

⁶Direct band-gap excitation can only be achieved with a higher ionization energy than the minimum or ‘actual’ band gap energy value.

where e is the electron charge, E is the electric field strength, ω is the center laser frequency, and m is the reduced mass of the exciton $1/m = 1/m_e + 1/m_h \simeq 0.5m_e$ based on the electron and hole masses m_e and m_h , respectively.

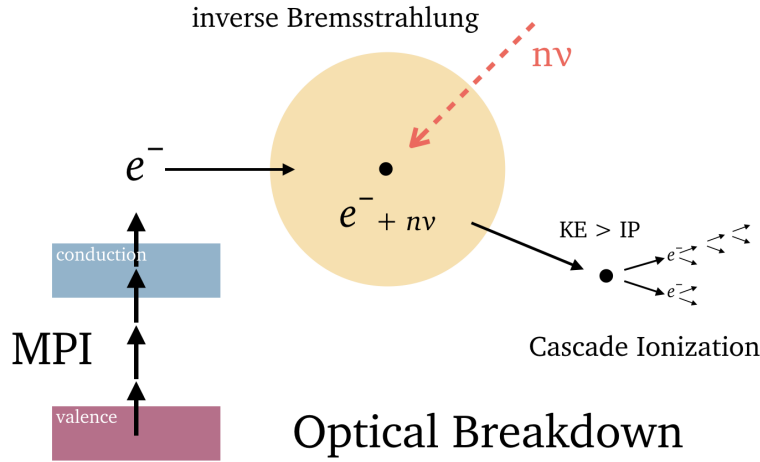


FIGURE 3.2: Free electrons from multiphoton ionization (or electron tunneling) participate in inverse Bremsstrahlung, causing cascade ionization. This simplified diagram was adapted from ref [100].

Free electrons accrue in the focal volume through the photoionization (W_{photo}) and cascade ionization (W_{casc}) rates, and are concurrently lost through the diffusion (W_{diff}) and recombination (W_{rec}) rates [44, 48]. The time-evolution of free-electron density (ρ_e) generated through laser–water interactions is described by [47, 48]

$$\frac{\partial \rho_e}{\partial t} = W_{\text{photo}} + W_{\text{casc}}\rho_e - W_{\text{diff}}\rho_e - W_{\text{rec}}\rho_e^2 \quad (3.11)$$

Nonlinear multiphoton absorption and electron tunneling comprise photoionization [98]; and collisions between high-kinetic-energy free electrons and neutral molecules cause cascade ionization [45]. Regardless of laser wavelength, the peak-intensity necessary to reach the critical electron density for OB depends on the pulse duration, because of the interactions between photoionization and cascade ionization rates [44, 48]. A very simple illustration of OB can be seen in Figure 3.2.

Photoionization occurs by multiphoton absorption, electron tunneling, or both: depending on the peak irradiance and wavelength of the laser pulse. Keldysh adiabaticity parameter, γ , defines the transition from multiphoton ionization (dominant when $\gamma \gg 1$) to tunnel ionization (dominant when $\gamma \ll 1$). The Keldysh adiabaticity parameter is the ratio

$$\gamma = \frac{\omega}{\omega_t} = \omega \frac{\sqrt{2m_e\Delta}}{eE} \quad (3.12)$$

where ω is the laser frequency, ω_t is the electron tunneling frequency [98]. The associated multiphoton ionization rate is given by [98]

$$W_{\text{MPI}} = \frac{2\omega}{9\pi} \left(\frac{m\omega}{\hbar}\right)^{3/2} \left(\frac{1}{16\gamma^2}\right)^n \Phi \left(\sqrt{2n - 2\frac{\tilde{\Delta}}{\hbar\omega}} \right) \exp \left[2n \left(1 - \frac{1}{4\gamma^2} \right) \right] \quad (3.13)$$

in which n is the multiphoton order $n = [\frac{\tilde{\Delta}}{\hbar\omega} + 1]$, $\tilde{\Delta}$ is given by eq 3.10, γ by eq 3.12, and

the portion in square brackets represents the integer part. The function Φ is the Dawson integral, calculated using an opensource MATLAB code [110]. At high enough intensities, $\gamma \ll 1$ and the tunnel ionization rate applies [98]

$$W_{\text{tun}} = \frac{2\Delta}{9\pi^2\hbar} \left(\frac{m\Delta}{\hbar^2}\right)^{3/2} \left(\frac{\hbar\omega}{\Delta\gamma}\right)^{5/2} \exp\left[-\frac{\pi\gamma\Delta}{2\hbar\omega} \left(1 - \frac{\gamma^2}{8}\right)\right] \quad (3.14)$$

There is also an intermediate range, where $1 \leq \gamma \leq 1.3$, and a weighted average of both the ionization rates, eqs 3.13 and 3.14, are used [107], which ensures that the photoionization rate is correct at any value of γ (Figure A.5).

The rate of cascade ionization rate depends on the ratio of free electrons in the focal volume with enough kinetic energy to undergo inverse Bremsstrahlung absorption of photons, and then generate more free electrons through collisions. The time between e_{aq}^- -water collisions is $\tau_c \sim 1.6-1.7$ fs [44, 111]—we use $\tau_c = 1.7$ fs. The critical kinetic energy of the electrons for inverse Bremsstrahlung⁷ to occur is taken as $3/2\tilde{\Delta}$ [44]. Using these values, the cascade-ionization rate is [44, 106]

$$W_{\text{casc}} = \frac{1}{\omega^2\tau_c^2 + 1} \left[\frac{e^2\tau_c}{cn_0\varepsilon_0 m(3/2)\tilde{\Delta}} I(t - \tau_{\text{ret}}, z) - \frac{m\omega^2\tau_c}{M} \right] \quad (3.15)$$

where $\tau_{\text{ret}} = n\tau_c$ (with n being the multiphoton order), $n_0 = 1.33$ is the refractive index of water, ε_0 is the vacuum permittivity, and M is the mass of a water molecule.

If the focal volume is assumed to be ellipsoidal⁸, then defining its dimensions using beam waist w_0 and Rayleigh range z_R , the diffusion rate (W_{diff}) is [44, 47]

$$W_{\text{diff}} = \frac{5\tau_c\tilde{\Delta}}{6m} \left[\frac{6}{w_0^2} + \frac{2}{z_R^2} \right] \quad (3.16)$$

The recombination rate (W_{rec}) we used is a commonly accepted empirical value, [112]

$$W_{\text{rec}} = 2 \times 10^{-9} \text{ cm}^3/\text{s} \quad (3.17)$$

Although eq 3.17 has been simplified by overlooking e_{aq}^- decay [94, 96], the rate of recombination loss is slow compared to the pulse durations used in our work, and therefore only minimally involved.

The calculated time-dependent electron density ($\rho_e(t)$) for pulses at $I = 10^{13} \text{ W cm}^{-2}$, with durations of 30 fs (dark blue), 100 fs (light blue), 200 fs (green), 1.5 ps (orange), and 36 ps (red), are compared in Figure 3.3a. The zero-value on the abscissa corresponds to the pulse center, and the time axis has been normalized to the respective pulse durations. The dashed line is an indicator of OB threshold density ($\rho_e = 1.8 \times 10^{20} \text{ cm}^{-3}$). Peak electron density rises with pulse duration because the contribution of cascade ionization increases as the pulse lengthens [44, 48]. The inset in Figure 3.3a illustrates the effect that pulse duration has on the intensity required to pass threshold ρ_e . As the pulse duration increases from 30 fs to 36000 fs, the necessary, threshold intensity for OB ρ_e decreases by two orders of magnitude.

⁷Inverse Bremsstrahlung, or free-free transition, is a process through which free e^- in a strong laser field can collide with heavier particles, such as atoms or ions, while absorbing or emitting photons. Through these collisions, the free e^- increases its kinetic energy until it exceeds the ionization energy of the heavier particle, knocking an electron loose, and resulting in a net gain of two lower energy electrons—This is cascade ionization [100].

⁸The shape of the focal volume does not impact the growth rate of the plasma volume.

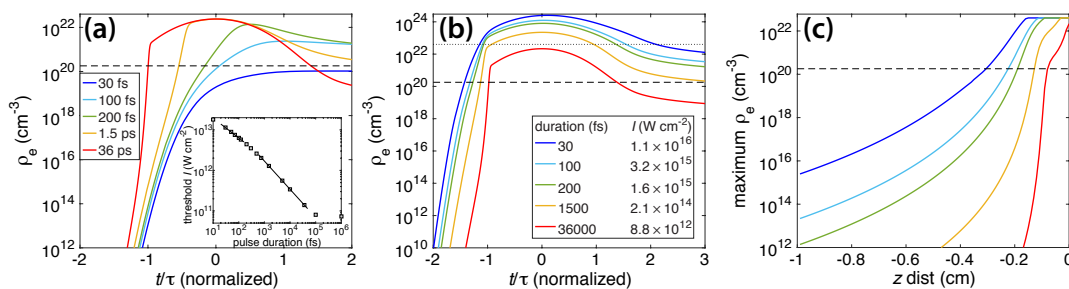


FIGURE 3.3: Electron density vs. time for 1×10^{13} W cm⁻² pulses (a), with a series of durations from 30 fs to 36 ps. Inset: threshold intensity required to achieve OB as a function of pulse duration. Electron density vs. time for 1 mJ pulses (b). Electron density vs. propagation distance z from the geometric focus for 1 mJ pulses (c).

When pulse energy is high (up to 5 mJ) and tight-focusing conditions are used, peak intensities far exceed the OB threshold. These high-energy, tight-focused conditions are commonly used for $[\text{AuCl}_4]^-$ reduction experiments [22, 24, 25, 63, 66–69]. However, even irradiation performed with 1 mJ pulses under the described conditions produces an ρ_e that exceeds the OB threshold by a factor of 50. It even exceeds the maximum ρ_e achievable in water with shorter pulses ($\rho_e = 4 \times 10^{22}$ cm⁻³, indicated by the dotted line in Figure 3.3b) [107]. To model e_{aq}^- availability for $[\text{AuCl}_4]^-$ reduction, the volume of plasma in which the electron-density exceeds the OB threshold should be estimated. As will be shown in Chapter 4, plasma volume can be estimated by calculating the critical distance, z_{crit} , just in front of the focal point—where the OB threshold is passed.

The value of z_{crit} for any given pulse energy, duration, and focusing-geometry can be calculated by solving eq 3.11 for a Gaussian beam (like described in eq 3.9) at a series of propagation distances $z < 0$ cm (because the focus itself is at $z = 0$ cm) to determine the highest electron density achieved. Equation 3.11 coupled to eqs 3.13–3.17 was solved using The Runge-Kutta integrator ode45 was incorporated into MATLAB and used to solve eq 3.11 coupled to the electron density rate formulas (eqs 3.13–3.17). This allows us to calculate the irradiance necessary at a given pulse duration to achieve optical breakdown by crossing the cavitation-bubble formation threshold $\rho_e = 1.8 \times 10^{20}$ cm⁻³, determined by experiments in water [43]. The resulting peak electron-density, as a function of z , is shown for the 1 mJ pulses (from Figure 3.3b) in Figure 3.3c. Plasma volume is proportional to z_{crit}^3 , and depends on both the energy and duration of the pulses. As the pulse duration decreases, OB occurs farther from the focus, with z_{crit} increasing from 0.1 cm for 36000 fs pulses to 0.3 cm for 30 fs pulses. In other words, at shorter pulse durations, the volume of plasma is larger; and the volume decreases, with OB only occurring very close to the focus, when longer pulses are used. Our simulations in Chapter 4 will show that for a series of pulse durations all using the same focusing-geometry, z_{crit} grows with peak-intensity as $z_{\text{crit}} \propto I^{1/2}$ —so plasma volume grows as $I^{3/2}$ [69]. Plasma volume growth is directly proportional to the rate of $[\text{AuCl}_4]^-$ reduction.

Tight-foci produce electron densities that exceed the OB threshold, $\sim 10^{20}$ cm⁻³, where loosely-focused geometries produce SCE through self-focusing and filamentation processes. These SCE processes, at low-NA, can cause intensity-clamping⁹, which limits

⁹Intensity-clamping is SCE self-sabotage. Essentially, SCE involves self-focusing—that’s how filamentation occurs. Intensity clamping happens when self-focusing prevents a desired intensity at the *actual* focal point, because too much intensity is lost at pre-focal, self-focused points. If some endeavor is made to correct

the availability of reducing species by capping the peak-intensity at $I \sim 10^{13} \text{ W cm}^{-2}$ [25, 99]. In contrast, tight-focusing (high-NA) geometries open SSTF [82] and spatial beam-shaping [83] options, which make filamentation and intensity clamping avoidable. Frequency components of the laser¹⁰ are spatially separated before the beam is focused. Both high-NA [24, 67, 69] and SSTF [22, 25, 63] have been used for the purpose of filamentation-avoidance. Figure 3.4 shows schematic diagrams (top) and photographs (bottom) of fs-laser irradiation of water using (a) collimated beam geometry [62], (b) low-NA focusing [25], (c) high-NA focusing [69], and (d) SSTF [22]. The absence of visible filaments in panels (c) and (d), compared to (b), suggest less intensity-clamping, and so a higher peak-intensity at the focal spot.

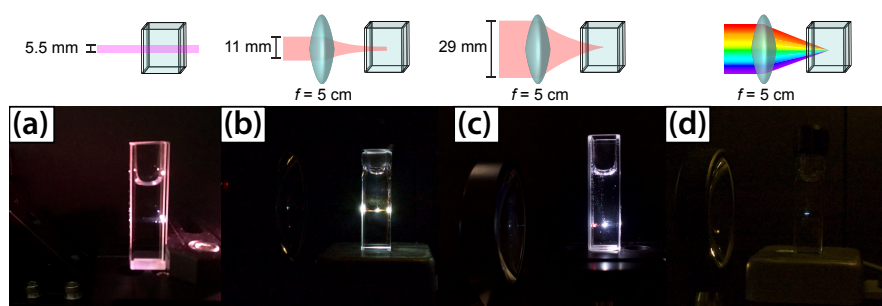


FIGURE 3.4: Diagrams (top) and photographs (bottom) of irradiated water using (a) collimated beam, (b) low-NA focusing, (c) high-NA focusing, and (d) SSTF.

Another phenomenon to consider during experimentation with focusing-conditions is cavitation bubble formation. Cavitation bubbles form when the OB electron-density threshold is exceeded [43], and are sensitive to the shape of the laser plasma [25, 83]. Under low-NA focusing-conditions with lots of SCE, the bubbles are ejected with low kinetic energy from the focus by plasma filaments, and are visible in Figure 3.4b as small streams of bubbles rising from the center of the cuvette. This condition results in inefficient, asymmetrical mixing of the reactive species in the solution, but can be mitigated with a magnetic stir-bar [25]. In general, stir bars are necessary when using LDP conditions, to disperse products mechanically throughout the solution [62, 72]. High-NA focusing and SSTF both produce plasmas with more spherical volume shapes, which radiate high kinetic energy bubbles into the solution [83], causing enough turbulence that additional mixing is unnecessary (Figure 3.4c) [25, 69].

3.2 Photoreduction Kinetics

3.2.1 Gold

Control over the morphology of AuNP products can be accomplished by manipulating the kinetics of nanoparticle formation. AuNP formation was first described in 1950 by LaMer's

the issue through compensation (for example, more energy is added to the beam), more pre-focal-point self-focused points will simply form.

¹⁰The output beam of the laser is centered at 800 nm but has a bandwidth of about 30 nm. Passing the output beam through the diffraction gratings of the external compressor not only allows ordering of potentially anomalous chromatic diffraction, but also the ability to expand or compress chirp and pulse durations.

nucleation and growth theory [113]; a foundational model that is still widely used [4, 74, 114]. Turkevich's studies on HAuCl_4 reduction with sodium citrate in 1951 produced more accurate formation mechanisms, such as autocatalysis and aggregate growth [115–117]. Numerous studies of metal nanoparticle growth-kinetics since then support autocatalytic [118–120] or aggregative [121, 122] growth mechanisms, or both. In 1997, Finke and Watzky reduced transition metal ions with H_2 and found nanoparticle formation to occur in a two-step rate law consisting of an initial, slow nucleation step, and an overlapping fast autocatalytic-growth phase [123]. Studies of femtosecond laser-induced photochemical Au^{3+} reduction since then [63, 72] have supported the specific application of the Finke-Watzky autocatalytic nucleation-growth rate law to this synthesis method particularly. This mechanism is described as

$$-\frac{d[A]}{dt} = \frac{d[B]}{dt} = k_1[A] + k_2[A][B] \quad (3.18)$$

where $[A]$ is the precursor (in our experiment, KAuCl_4) concentration; $[B]$ is the metal nanoparticle (AuNP) concentration; k_1 is the constant for slow, metal-cluster nucleation; and k_2 is the rate constant describing faster autocatalytic nanoparticle growth [118, 123]. Integration of eq 3.18 yields the time-dependent precursor and metal nanoparticle concentrations $[A_t]$ and $[B_t]$ [123]

$$[A_t] = \frac{\frac{k_1}{k_2} + [A_0]}{1 + \frac{k_1}{k_2[A_0]} e^{(k_1+k_2[A_0])t}} \quad (3.19)$$

$$[B_t] = 1 - \frac{\frac{k_1}{k_2} + [A_0]}{1 + \frac{k_1}{k_2[A_0]} e^{(k_1+k_2[A_0])t}} \quad (3.20)$$

where the 0-subscript indicates initial concentrations, and t -subscript is the concentration at time t . The rate law in eq 3.19 has been used to describe AuNP formation from reducing ionic precursors via wet chemical routes [29, 118, 123] and for femtosecond laser-induced $[\text{AuCl}_4]^-$ reduction under a variety of laser conditions and solution compositions [62, 63, 69, 72]. Equation 3.20 follows if it is assumed that the conversion of Au^{3+} to Au^0 is fast enough that no significant concentration of intermediate species like Au^+ builds up.

The time-dependent concentrations of $[\text{AuCl}_4]^-$ and AuNPs needed to determine the reaction kinetics can be extracted from *in situ* UV-vis spectra recorded during laser irradiation [63]. Figure 3.5a shows representative absorbance spectra of $[\text{AuCl}_4]^-$ after different irradiation times. The arrow labeled '250 nm' corresponds to the decrease in the *ligand-to-metal charge transfer* (LMCT) band of $[\text{AuCl}_4]^-$, while the arrow labeled '450 nm' corresponds to the growth of AuNPs [63, 69, 124]. To obtain the time-dependent $[\text{AuCl}_4]^-$ concentration in eq 3.19, the absorbance of $[\text{AuCl}_4]^-$ is recorded at $\lambda = 250$ nm. However, AuNPs also absorb in the UV range, so the absorbance at 250 nm contains contributions from both the $[\text{AuCl}_4]^-$ precursor and AuNP product species. The $[\text{AuCl}_4]^-$ spectrum can be isolated from the 250 nm absorbance by subtracting off the AuNP contribution, as described in refs [63] and [69]. Alternatively, monitoring the absorbance at $\lambda = 450$ nm, where only AuNPs absorb [124], allows direct monitoring of time-dependent AuNP growth. Both representations of the reaction kinetics are shown in Figure 3.5: normalized absorbance of $[\text{AuCl}_4]^-$ at 250 nm in Figure 3.5b, and 450 nm as a function of laser irradiation time for focused 30 fs laser pulses at a series of pulse

energies in Figure 3.5c [69]. The spots are the plotted experimental data, and the solid lines are fits to eq 3.19 (Figure 3.5b) and eq 3.20 (Figure 3.5c). The disappearance rate of $[\text{AuCl}_4]^-$ and growth rate of AuNPs mirror each other, reflecting that the rate constants may be extracted from either spectral absorbance. In practice, small amounts of intermediate species such as Au^+ are present during photochemical reduction [63], so the rate constants extracted from fitting the normalized 450 nm absorbance to eq 3.20 are 20–50% lower than those from fitting the normalized 250 nm absorbance to eq 3.19.

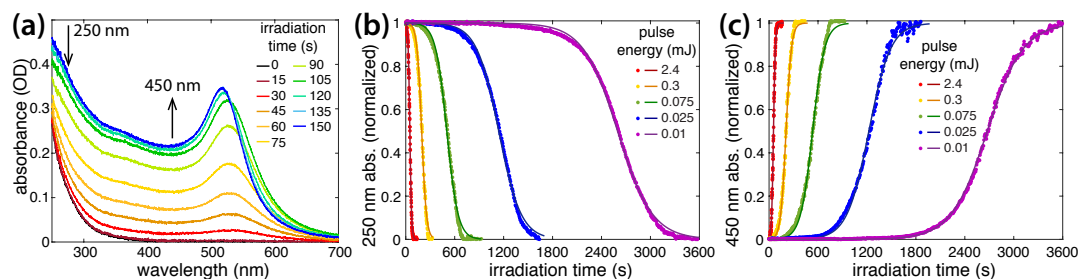


FIGURE 3.5: (a) UV-vis spectra of $[\text{AuCl}_4]^-$ solution irradiated for different times. Representative plots of normalized absorbance at 250 nm (b) and 450 nm (c), (d) (dots) as a function of irradiation time for the pulse energies labeled in the legend, with fits to eq 3.19 (b), eq 3.20 (c). Data taken from refs [69] and [62].

Extracting the rate constants at a series of experimental conditions (like solution pH [63] or pulse energy [62, 69]) illuminates the roles that the reactions in eqs 3.1–3.6 play in the conversion of $[\text{AuCl}_4]^-$ to AuNPs. The rate constants k_1 and k_2 can be extracted from fits to eq 3.19 for each set of pulse conditions, and plotted as functions of pulse energy. This will yield information about the relationships between the rate constants and peak intensity I .

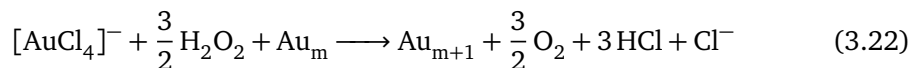
Nucleation and Autocatalytic Growth

Hydrated-electrons (e_{aq}^-) and hydrogen radicals are both capable of reducing $[\text{AuCl}_4]^-$, but the rapid consumption of $\text{H}\cdot$ via eq 3.6 observed using picosecond pulses [94] suggests that the contribution by $\text{H}\cdot$ to $[\text{AuCl}_4]^-$ reduction is insignificant. In contrast, hydrated electrons are formed from both the free electrons generated in OB plasma in eq 3.2, within several hundred femtoseconds [95, 96], and from the reaction between water and $\text{H}\cdot$ in eq 3.6. Hydrated electrons have lifetimes as long as hundreds of nanoseconds in pure water [97] and react with $[\text{AuCl}_4]^-$ with a diffusion-controlled rate constant of $6.1 \times 10^{10} \text{ M}^{-1} \text{ s}^{-1}$ [125]. Therefore, hydrated electrons are the dominant $[\text{AuCl}_4]^-$ reducing agent, and the reaction is [73]



Another product of water photolysis, H_2O_2 , is generated from the recombination of two hydroxyl radicals, shown in eq 3.5. It drives $[\text{AuCl}_4]^-$ reduction and AuNP formation [22, 25, 63, 69]. Tangeysh et al. explored the role that H_2O_2 played in $[\text{AuCl}_4]^-$ reduction by monitoring the UV-vis absorbance of $[\text{AuCl}_4]^-$ samples *after* laser-irradiation termination, but before all of the $[\text{AuCl}_4]^-$ had been consumed [22]. They explained the post-irradiation $[\text{AuCl}_4]^-$ reduction and SPR absorbance-peak growth by proposing that

the H_2O_2 produced during irradiation reduced the remaining $[\text{AuCl}_4]^-$, in the presence of the existing AuNPs [22]. This hypothesis was developed further by Tibbetts et al. [63], using previous work showing that H_2O_2 reduces $[\text{AuCl}_4]^-$ in the presence of AuNPs by [126, 127]



where the already-existing AuNPs catalyze $[\text{AuCl}_4]^-$ reduction. This process underlies the observed autocatalytic reduction kinetics of $[\text{AuCl}_4]^-$.

3.2.2 Silver

Hydrogen peroxide-formation hinders the application of this technique to other metals, because H_2O_2 generally behaves as an oxidant. For instance, Ag^0 will oxidize back to Ag^+ (Section 5.1) in the presence of H_2O_2 [86, 128, 129], and inhibit silver nanoparticle (AgNP)-formation by photochemical reduction in an OB plasma [130, 131]. This is the topic of Chapter 5. Back-oxidation¹¹ of Ag^0 to Ag^+ in the presence of H_2O_2 has been pre-empted in the context of some γ radiation AgNP-synthesis methods by using secondary alcohols to scavenge or stabilize hydroxyl radicals [128, 132]. Because of this silver- H_2O_2 dynamic, it is only possible to prepare AgNPs in OB plasma with some modification to the Ag^+ precursor solution. Examples of these solution-additives have included TiO_2 [133], sodium citrate [15], and sodium dodecylsulfate surfactant [134]. Colloidal AgNPs have been synthesized in OB plasma from aqueous AgNO_3 solutions containing polyvinylpyrrolidone; but only in the presence of ammonia [131]. In Chapter 5, aqueous solutions containing ammonia and silver ions are irradiated, and their radical chemistry is examined. By modulating the concentration of ammonia in solution, we were able to explore the possible radical mechanisms and products formed in OB plasma.



Radical scavengers have previously been shown to manipulate particle sizes in laser-synthesized silver nanoparticles [130, 131, 135, 136]. Whereas AgNP develop according to a first-order rate law, radical scavenging has a much more pronounced effect on specifically the k_2 of AuNP formation. In Chapter 6, the addition of hydroxyl radical scavengers to gold precursor solutions is examined, and the effects on the resulting AuNP products are analyzed. Because autocatalytic growth of gold nuclei is driven by H_2O_2 , it was predicted that $\text{OH}\cdot$ scavengers would be especially effective at controlling AuNP sizes, because they should limit H_2O_2 formation. In Chapter 6 hydroxyl radical scavengers *isopropyl alcohol* (IPA) and acetate were added to precursor solutions with the expectation that hindered H_2O_2 -formation would slow AuNP growth kinetics, make it possible to tune their diameters and size dispersities. This experiment shows that both IPA and acetate are capable of tuning the size distribution of AuNP products without

¹¹The meaning here is simply 'oxidation to a former oxidized state, after desirable reduction had been achieved'.

leaving a surfactant layer—specifically by controlling the rate of autocatalytic growth, k_2 . Reaction kinetics and the mechanisms underlying radical scavenging activity of IPA and acetate are discussed.

3.3 Experimental Parameters

3.3.1 Focus

A more detailed [examination](#) of the presence of OB and SCE in water using *specifically* the [tightly-focused](#) geometry was performed for Chapter 4 and is re-referenced in Figure 3.6a; where emission spectra from the laser in water were collected with the compact spectrometer at position (i) for OB, and position (ii) for SCE [37, 49]. An [illustration](#) of the parameters related to the focus-geometry can be found in Appendix A.

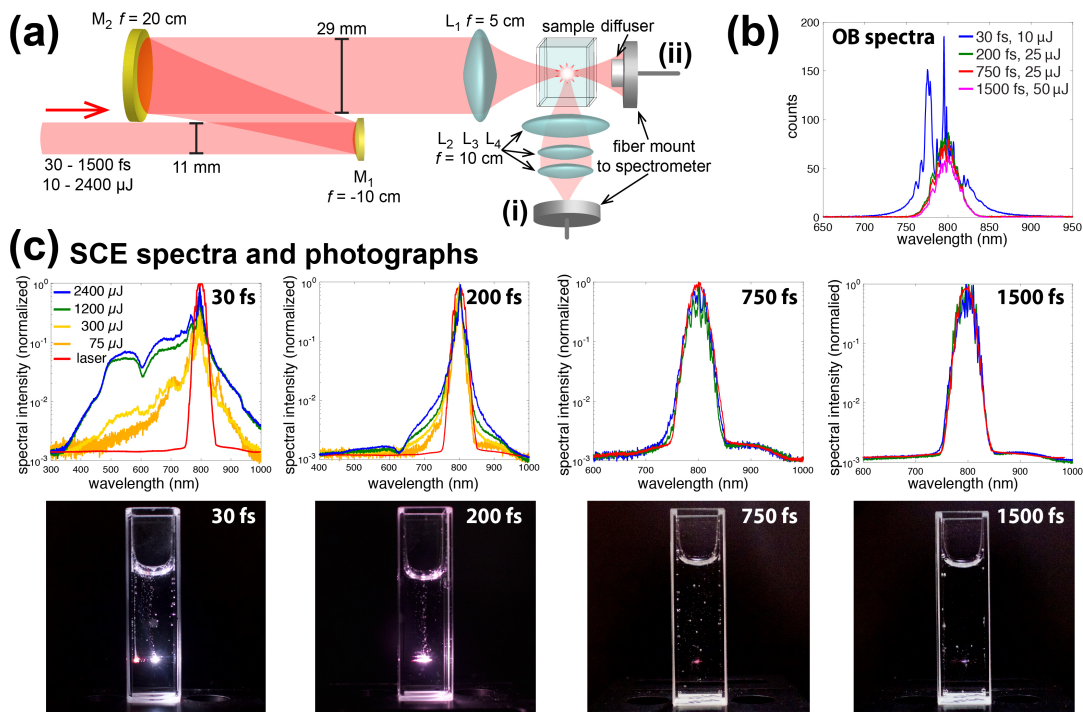


FIGURE 3.6: (a) Experimental setup showing locations of spectral measurements for OB (position (i)) and SCE (position(ii)). (b) Spectra of OB measured at lowest pulse energies for each pulse duration. (c) SCE spectra for each pulse duration at selected pulse energies.

In the [focused setup](#), significant spectral emission was recorded at that position, even at the [lowest pulse energies](#), for all τ_p (Figure 3.6b). This is evidence of cavitation bubble formation, which occurs after a threshold electron density ($\rho_e = 1.8 \times 10^{20} \text{ cm}^{-3}$) has been passed [43, 49, 50]. These cavitation bubbles are pictured in Figure 3.6c where $E_p = 2400 \mu\text{J}$ and $\tau_p = 30 \sim 50 \text{ fs}$. Spectra associated with the tightly-focused beam following interaction with water show SCE production when τ_p is 30 and 200 fs, but no SCE when τ_p is 750 or 1500 fs; even at the highest available energy (Figure 3.6c). The SCE spectra recorded with 30 fs pulses emit at wavelengths below 400 nm, agreeing with existing literature [78, 81]. Another note regarding SCE in the tightly-focused setup: the photograph of the 30 fs pulse in Figure 3.6c shows a secondary bright spot to the left

of the brighter focal-point, near the wall of the quartz cuvette. This is not a result of white-light or SCE in the quartz itself—it is in the solvent, and might be a result of the beam having self-focused through the quartz wall. There are additional images in Figure A.4. For tightly-focused beams in general, OB is expected at any pulse duration, and SCE may also be present if the pulse is short¹². However, when the beam is loosely-focused or collimated, only SCE is expected.

As explained in Section 2.2, and illustrated in Figure 3.6, our 11 mm beam was first expanded to 29 mm before focusing into the sample cuvette. The purpose for this was to ensure that the plasma generated at the focal point is as dense as possible. Focusing-geometries influence the nature of nonlinear laser pulse–solution interactions (Section 1.1). If the focus is weak, SCE yields a LDP environment with electron-densities on the order of $\rho_e \sim 10^{18} \text{ cm}^{-3}$. LDP setups have been used for photochemical Au^{3+} reduction experiments [62, 72] and gold ablation experiments [60, 86]. Weakly-focused, LDP conditions are relatively well-suited to applications like AuNP synthesis, because second-order reactions (like those that generate H_2O_2) are suppressed [72, 86]. Without an excess of reducing species, Au^{3+} conversion to AuNPs is slowed. However, focused-geometries will also form AuNPs [22, 24, 25, 63, 66, 67, 69].

Ref	condition	energy (mJ)	size (nm)
[72]	LDP	1.35	29.1 ± 17.3
[62]	LDP	2.7	27.1 ± 7.0
[25]	low-NA	1.8	13.6 ± 8.0
[67]	high-NA	5.6	4.0 ± 1.7
[69]	high-NA	2.4	3.5 ± 1.9
[25]	SSTF	1.8	10.2 ± 4.1
[63]	SSTF	2.5	9.2 ± 4.1

TABLE 3.1: Reported laser focusing conditions and resulting AuNP sizes. Particles generally become more monodisperse as the focus is tightened.

Intensity, in detail, was explained with eq 3.8 in Section 3.1.2. However, intensity can be approximated as $I = J \text{ s}^{-1} \text{ cm}^{-2}$, or power divided by the area of the focal point. The plasma area can be approximated as a sphere where $A = 4\pi r^2$ and the power is the energy delivered per pulse or E_p/τ_p .

High-NA Tight-Focus

Solving eq 3.11 for a range of (experimentally used) pulse durations of 30, 200, 750 and 1500 fs (fwhm), the critical irradiance to cause OB at each pulse duration was determined using the threshold of $\rho_e = 1.8 \times 10^{20} \text{ cm}^{-3}$ based on the cavitation bubble threshold recorded in a recent study.[43] Figure 3.7 shows the time-evolution of the free-electron density ρ_e at 30 fs (blue), 200 fs (green), 750 fs (red), and 1500 fs (magenta); the associated peak-irradiances in W cm^{-2} are indicated in the legend. The value of zero on the time-axis corresponds to the center of the pulse. The decreasing irradiance needed to reach the OB threshold as the pulse duration lengthens from 30 to 1500 fs is due to the increasing participation of cascade ionization (eq 3.15) in the production of free electrons at longer pulse durations, as noted in earlier work [44, 48].

¹²This isn't because SCE depends on pulse durations, but because OB tends to dominate (via tunnel ionization) as the pulse is lengthened.

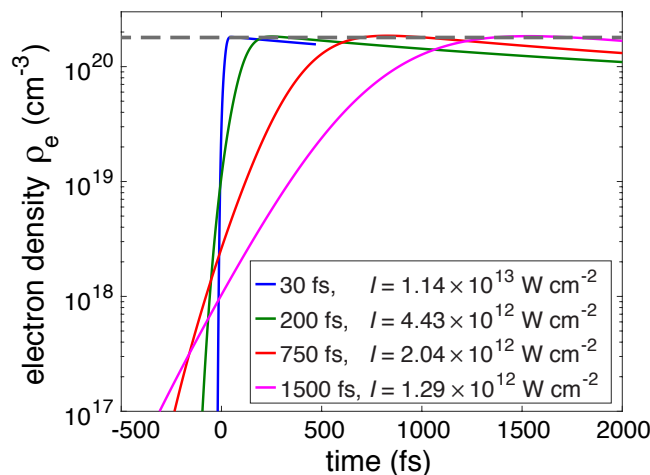


FIGURE 3.7: Time evolution of the free-electron density ρ_e as a function of time immediately following interaction with pulses with durations of 30 fs (blue), 200 fs (green), 750 fs (red), and 1500 fs (magenta), at the irradiances indicated in the legend. The maximum value of ρ_e is $1.8 \times 10^{20} \text{ cm}^{-3}$, as indicated by the gray-dashed line.

Because the peak-irradiance range of 2.5×10^{13} to $6.0 \times 10^{16} \text{ W cm}^{-2}$ significantly exceeds the threshold-irradiance for optical breakdown at all pulse durations, we wish to estimate the plasma volume in which the electron density exceeds the OB threshold under our experimental conditions. Of particular interest is the growth of the plasma volume with peak-irradiance due to the widely recognized role of electrons generated from OB and SCE in the photochemical reduction of $[\text{AuCl}_4]^-$ and other metal salts [22, 24, 63, 66, 70, 72, 73]. To estimate the plasma volume, we first calculate the critical propagation distance z_{crit} in front of the focus where OB begins, based on Gaussian beam propagation via eq 3.9. While the approximation of Gaussian beam propagation at high irradiance near the geometric focus neglects nonlinear beam propagation phenomena and thus will result in a crude approximation of z_{crit} and the true plasma volume [44, 49, 50, 79], our goal is to estimate the growth of the plasma volume with pulse energy over a wide range of pulse durations and not to model the propagation of any particular pulse in the medium nor calculate the exact plasma volume. Thus, we must assume that the error in the value of z_{crit} does not change dramatically over the experimental pulse energy range. This assumption is reasonable because the peak-irradiance range exceeds the optical breakdown threshold by a factor of 10 at even the lowest pulse energy used for each pulse duration in the experiments (Figure 3.7 and Table 4.1).

To identify z_{crit} , eq 3.11 was propagated for each pulse energy and duration used in our experiments at a series of propagation distances $z < 0 \text{ cm}$ (just before the focal point at $z = 0 \text{ cm}$) in order to determine the highest electron density achieved as a function of propagation distance z . The results for time-dependent electron density produced by 750 fs, 25 μJ pulses at a series of z values is shown in Figure 3.8(a). The maximum electron density as a function of z is shown in Figure 3.8(b) (blue line, right ordinate axis), superimposed on the spatial profile of the Gaussian beam (red volume, left ordinate axis). In both panels, the electron density threshold of $\rho_e = 1.8 \times 10^{20} \text{ cm}^{-3}$ is indicated by a gray-dashed line. The peak electron density achieved as a function of z was calculated using these methods for each pulse energy and duration used in the experiments (Supporting

Information, Figure S7) and the associated values of z_{crit} determined at each pulse duration and energy. At all pulse durations, the absolute value of z_{crit} was found to grow with irradiance I as approximately $I^{1/2}$ as shown in Figure 3.8(c).

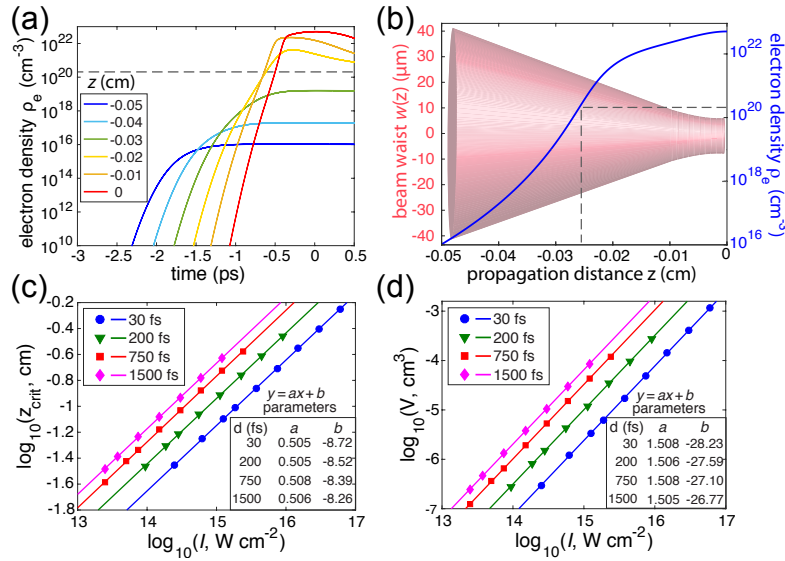


FIGURE 3.8: (a) Calculated electron density ρ_e as a function of time for a 750 fs, 25 μJ pulse at a series of propagation distances between $z = -0.05$ cm and the focus at $z = 0$ cm. (b) Peak ρ_e as a function of z (blue curve) overlaid with the spatial profile of the Gaussian beam. In both panels, the dashed gray lines denote the plasma threshold $\rho_e = 1.8 \times 10^{20} \text{ cm}^{-3}$. Calculated values of z_{crit} (c) and plasma volume V (d) as a function of irradiance I for 30 fs (blue \circ), 200 fs (green ∇), 750 fs (red \square), and 1500 fs (magenta \diamond) pulses, with linear fits (solid lines) and fitting coefficients given in the legends.

While rigorous calculations of the spatial distribution of electron density obtained from propagating femtosecond pulses in water reveal a variety of plasma volume shapes depending on the focusing-geometry and pulse duration [49, 79], the plasma volume can be approximated by simple geometric shapes such as an ellipsoid with dimensions based on the numerical aperture [44, 137]. Here, we estimate the plasma volume using the obtained values of z_{crit} ; approximating the plasma volume with any three-dimensional shape such as an ellipsoid, cylinder, or cone will result in the plasma volume growing as z_{crit}^3 . Thus, while the particular choice of shape will determine the calculated value of the plasma volume at any given pulse duration and irradiance, the choice of shape will not affect the growth of the plasma volume with peak irradiance I , which will grow as $V \propto I^{3/2}$ based on the relation $z_{\text{crit}} \propto I^{1/2}$. For simplicity, we approximate the volume by a cone with height $|z_{\text{crit}}|$ and radius $w(z_{\text{crit}})$ based on the measured beam diameters fit with eq 3.9. The resulting plasma volumes and fit values are shown in Figure 3.8(d), confirming that the volume grows as $I^{3/2}$. We will connect these results on the growth of the plasma volume with peak irradiance at each pulse duration with the observed $[\text{AuCl}_4]^-$ reduction kinetics in Section 4.3.

3.3.2 pH

Apart from the presence or absence of radical scavenger, and the working concentration of $[\text{AuCl}_4]^-$, a major chemical consideration is the pH of precursor solutions. Changing the pH of aqueous $[\text{AuCl}_4]^-$ solutions by adding either HCl or KOH affects the reduction kinetics and by extension the resulting AuNP sizes [63]. The effects are a consequence of Au^{3+} complex speciation: $[\text{AuCl}_4]^-$ dominates under acidic conditions, $[\text{Au}(\text{OH})_4]^-$ dominates under basic conditions, and mixtures of $[\text{AuCl}_x(\text{OH})_{4-x}]^-$, $x = 1 - 3$, species exist under neutral conditions [138, 139]. Different complex stabilities were thought to be the driving force for Au^{3+} reduction with chemical reducing agents, where $[\text{Au}(\text{OH})_4]^-$ was less reactive because of stronger Au-OH bonds, compared to Au-Cl bonds [138, 139]. With increasing pH, as solution was irradiated with 36 ps, 2.5 mJ pulses under SSTF focusing conditions, the reverse trend occurred, and higher $[\text{AuCl}_4]^-$ reduction rates formed smaller AuNPs [63]. At low pH, the hydrated-electron lifetime is reduced [96] and H_2O_2 oxidizes AuNPs [140], causing a slow $[\text{AuCl}_4]^-$ reduction rate that produced large, poly-disperse 19.4 ± 7.1 nm AuNPs (at pH 2.5). When pH was higher (pH 5.4), the hydrated-electron lifetime is longer [96] and the oxidation potential of H_2O_2 increases as it is deprotonated to HO_2^- [127], leading to faster reduction of $[\text{AuCl}_4]^-$ and small AuNPs with size distributions of 4.8 ± 1.9 nm. Slightly larger 6.6 ± 3.1 nm AuNPs were formed at pH 8.4 due to the acceleration of the autocatalytic growth rate constant k_2 in eq 3.19.

For comparison with the results in ref [63], experiments performed in our laboratory using the tight-focusing conditions in ref [69] also showed that the AuNP size depends on solution pH. Aqueous solutions (0.1 mM KAuCl_4) with varying amounts of KOH (up to 0.75 mM, pH 4.0–9.3) were irradiated with 50 μJ , 30 fs pulses for 10–33 min, sufficient to convert all $[\text{AuCl}_4]^-$ to AuNPs. By monitoring UV-vis spectra and observing that as solution pH increases, the product SPRs blueshift and decrease in intensity; indicating the production of smaller AuNPs [124]. The most monodisperse AuNPs were obtained at pH 9.3, with a size-distribution of 9.2 ± 4.5 nm. The slightly large average AuNP size (relative to other products in the study) is because there were very few < 4 nm particles compared to what had been seen at lower pH. This absence of extremely small particles is likely due to the high concentration of H_2O_2 produced in the plasma, as discussed in ref [63].

3.3.3 Hydroxyl Radical Scavengers

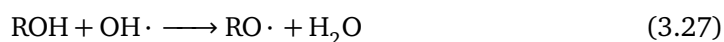
The three scavengers examined in this thesis are liquid ammonia, acetate, and isopropyl alcohol. Preliminary experiments were performed to give us a general idea of how these scavengers might affect the formation of gold and silver nanoparticles. Originally, our attention was on silver and Au-Ag alloys, as photoreduction–synthesis of Ag^+ is unable to complete without H_2O_2 suppression. We ran preliminary experiments with sodium acetate and liquid ammonia, finding the results to be somewhat comparable at lower concentrations, but found ammonia to ultimately be a more stable and predictable additive. For isolated gold, we tried sodium acetate and isopropyl alcohol; mainly because they were inexpensive and accessible, and preliminary trials with liquid ammonia didn't yield particularly interesting results.

The hydrated-electron scavenger N_2O , and hydroxyl radical scavengers 2-propanol and ammonia, were originally studied in water radiolysis using X-rays and γ rays [141]. More recently, they have been used to control the photochemical synthesis of Au and Ag nanoparticles in femtosecond-laser plasmas [68, 72, 131, 136]. The addition of N_2O

to aqueous $[\text{AuCl}_4]^-$ is expected to limit the availability of hydrated electrons and slow the $[\text{AuCl}_4]^-$ reduction rate, forming fewer Au^0 nuclei in solution. This situation would result in a significant number of Au^{3+} ions being reduced on the surface of the Au^0 nuclei in the presence of H_2O_2 , promoting the surface-mediated autocatalytic growth into larger AuNPs. In contrast, the addition of a hydroxyl radical scavenger such as 2-propanol should not only limit the production of H_2O_2 via eq 3.5, but also prevent the quenching of hydrated electrons via eq 3.3 (although, as will be discussed, this is not always the case). As a result, $[\text{AuCl}_4]^-$ reduction should be fast and autocatalytic AuNP growth should be limited, resulting in smaller AuNPs. These predictions have been laid out in literature [68, 72]. One of our peer-reviewers offered feedback before the final form of our Molecules article was submitted for publication: an additional challenge to forming AgNPs from AgNO_3 with radiation-based methods may lie in the activity of the nitrate ion as a hydrated-electron scavenger [142, 143]. For that reason, some of studies have used AgClO_4 as their Ag^+ AgNP precursor in radiolysis experiments [144–146]. Accordingly, we performed an experimental subset in which AgClO_4 was used as the precursor material.

Belmouaddine et al. [72] investigated the effect of adding N_2O or 2-propanol to aqueous $[\text{AuCl}_4]^-$ solutions they irradiated with 1.35 mJ, 112 fs pulses. They monitored the reduction kinetics to determine the k_1 and k_2 rate constants in eq 3.19. By comparing the k_2/k_1 ratios obtained in the two scavenger experiments, they were able to relate each scavenger to its role in the reduction and autocatalytic growth processes. In the presence of the hydrated-electron scavenger N_2O , the k_2/k_1 ratio was two orders of magnitude higher than it was when the radical scavenger 2-propanol was used. This is consistent with the dependence of k_1 and k_2 on hydrated-electrons and H_2O_2 , discussed in Section 3.1. The resulting AuNPs synthesized in the presence of N_2O and 2-propanol were 54.4 ± 9.8 nm, and 28.5 ± 5.9 nm. These results are consistent with the predictions that (1) slow nucleation and significant autocatalytic growth in the presence of N_2O will produce large AuNPs, and (2) fast nucleation and limited autocatalytic growth in the presence of 2-propanol will produce small AuNPs.

In another study, Uwada et al. [68] investigated the effects of alcohols (1-propanol, 2-propanol, ethanol) on aqueous $[\text{AuCl}_4]^-$ solutions irradiated with 120 fs pulses, using a series of pulse energies from 1 to 50 μJ . At low pulse energies, with intensity below $7 \times 10^{15} \text{ W cm}^{-2}$, no AuNPs formed without alcohols. AuNP size-dependence on pulse energy followed the *opposite* trend to that observed in ref [25]; and in our own study in Chapter 5: the AuNPs formed in solutions containing 1-propanol increased in diameter from 24 to 37 nm when the intensity increased from 2×10^{15} to $7 \times 10^{15} \text{ W cm}^{-2}$ [68]. Uwada et al. proposed that the alcohol radicals formed from the $\text{OH}\cdot$ scavenging reaction



act as the primary reducing agents of $[\text{AuCl}_4]^-$ at low laser intensities, where relatively few hydrated electrons are formed. This could mean that radical scavengers not only manage ultimate AuNP size outcomes, but also bolster photochemical reduction of $\text{Au}^+ \rightarrow \text{AuNPs}$ at low laser intensities, by providing another free-radical reducing agent.

Chapter 4

Pulse Study

4.1 Laser Parameters

4.1.1 Pulse Energy, Pulse Duration, and Intensity

Several research groups have studied size-control in AuNPs synthesized by photochemical Au³⁺ reduction. Routes to achieving control require manipulation of experimental conditions: the laser setup itself, the solution composition, or both. Laser parameters that might affect AuNP growth rates include the focusing-geometry, the pulse energy (E_p), and the pulse duration (τ_p), because they are all factors that determine the [generation of OB and SCE](#) [25, 62, 69]. We already selected a tight, high-NA [focusing-geometry](#) that will remain consistent throughout all trials. The adjusted parameters will be the pulse energy and duration, both of which affect intensity. The range of conditions is outlined in Table 4.1.

Because a pulse can be plotted as a Gaussian distribution, it is easy to visualize with a graph where the y-axis is intensity and the x-axis is time, such as in Figure 4.1. The peak broadens as the pulse duration is lengthened, and narrows when the pulse is shortened. Energy is represented as the area under each curve, so, between two pulses containing the same amount of energy, a longer pulse will have lower intensity than a pulse with a shorter duration.

Experimental Variables

The relationship between pulse duration, pulse energy, and peak-intensity is reflected in Table 4.1. The conditions with short pulse durations and high energy produce our maximum peak-intensities. It was confirmed during our examination of [microplasma generation](#) that even the lowest intensities produced under our [experimental conditions](#) surpass the electron density threshold, $\rho_e = 1.8 \times 10^{20} \text{ cm}^{-3}$, so OB is achieved in all cases.

d (fs)	E (μJ)	I (W cm^{-2})
30	10 – 2400	$2.5 \times 10^{14} - 6.0 \times 10^{16}$
200	25 – 2400	$9.4 \times 10^{13} - 9.0 \times 10^{15}$
750	25 – 2400	$2.5 \times 10^{13} - 2.4 \times 10^{15}$
1500	50 – 2400	$2.5 \times 10^{13} - 1.2 \times 10^{15}$

TABLE 4.1: Pulse durations τ_p , energies E_p , and calculated peak irradiance I .

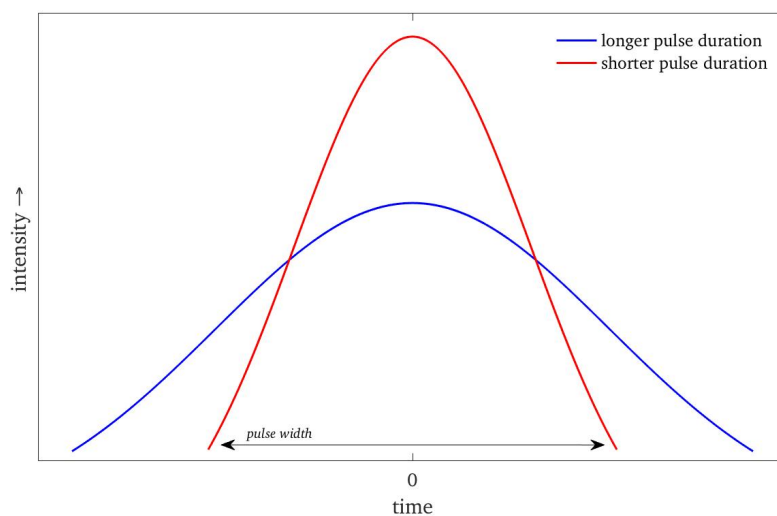


FIGURE 4.1: The area under each curve represents the energy, E_p , contained in each pulse, and the width of the base of each curve is the pulse duration, τ_p . Assuming each pulse carries the same energy, the total intensity I of the longer pulse is lower than the intensity of the shorter pulse.

4.2 Results

The photochemical conversion of Au^{3+} to AuNPs is easily monitored with UV-vis spectroscopy by tracking the time-dependent consumption of the LMCT peak of $[\text{AuCl}_4]^-$ and the growth of the AuNP SPR peak. Figure 5.9a-e shows representative UV-vis spectra of $\text{Au}^{3+} \rightarrow \text{AuNP}$ conversion in the focal plasma, using 2400 μJ pulses with durations 30 fs, 200 fs (both negative and positive chirp), 750 fs, and 1500 fs. From these spectra, the irradiation time required for complete conversion of Au^{3+} to AuNPs (τ) is designated as the time at which the SPR peak-absorbance growth ceases; shown by the plot of SPR absorbance versus irradiation time in Figure 5.9f, where τ for each pulse duration can be visually approximated according to the point where the slope plateaus. Using the determined value of τ and the corresponding UV-vis spectrum that contained only AuNPs, the concentration of Au^{3+} at intermediate times, when both Au^{3+} and AuNPs are present in the solution, is obtainable. By isolating the $[\text{AuCl}_4]^-$ absorbance-contribution in the UV-region of the spectra [63], where both $[\text{AuCl}_4]^-$ and AuNPs are present in solution, the recorded absorbance at $\lambda = 250$ nm will reflect the sum of the absorbances of both species. By quantifying the fractional AuNP content using absorbance at $\lambda = 450$ nm (where $[\text{AuCl}_4]^-$ doesn't absorb) and subtracting off the expected corresponding AuNP absorbance at $\lambda = 250$ nm, the $[\text{AuCl}_4]^-$ absorbance-contribution at $\lambda = 250$ nm may be isolated. Further details are provided in Appendix C and in Figure C.1. The resulting time-dependent concentration of $[\text{AuCl}_4]^-$ is used to evaluate the reaction kinetics in this study.

The nucleation rate constant k_1 depends on the OB plasma; specifically the availability of electrons to reduce Au^{3+} . The autocatalytic growth rate constant k_2 depends on the availability of H_2O_2 to drive the surface-mediated Au^{3+} reduction on existing AuNPs or gold nuclei in the solution [126, 127, 147]. Figure 4.3 shows the concentration of Au^{3+} as a function of irradiation time for representative experiments conducted with (a) 2400 μJ pulses, (b) 75 μJ pulses, and (c) 6×10^{14} W cm^{-2} pulses. The experimental data

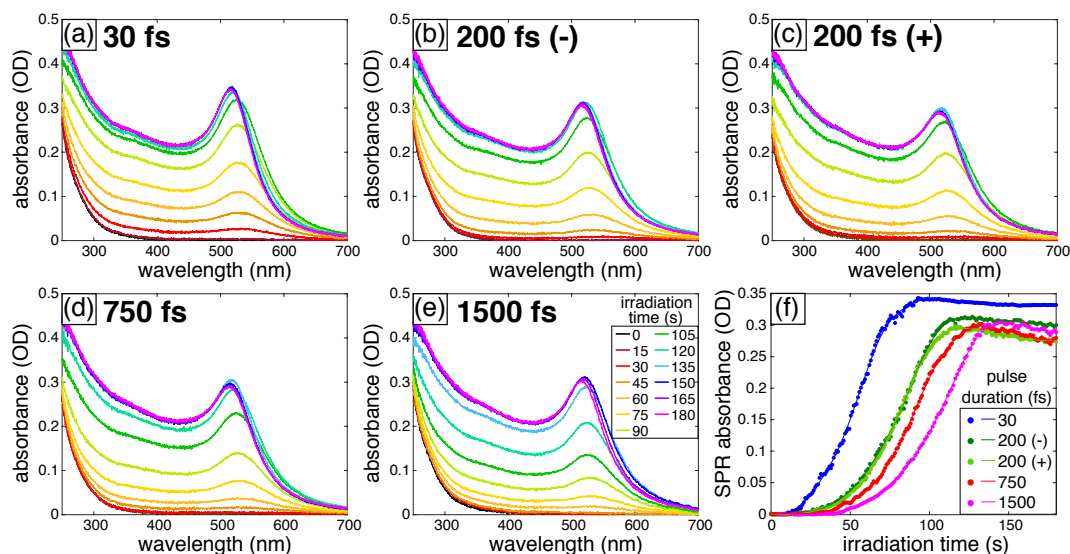


FIGURE 4.2: UV-vis spectra recorded during irradiation of aqueous $[\text{AuCl}_4]^-$ with 2400 μJ pulses with durations 30 fs (a); 200 fs, negative chirp (b); 200 fs, positive chirp (c); 750 fs (d), and 1500 fs (e). The spectra recorded at different irradiation times are indicated by the colors associated with the legend in panel (e). Panel (f) shows the time-dependent absorbance of the SPR feature in the spectra (a) through (e), showing the required irradiation time for complete conversion of $[\text{AuCl}_4]^-$ to AuNPs.

are shown as circles and fit to eq 3.19 as solid lines. Representative plots for each pulse duration and energy are shown in Appendix C, Figure C.2. The extracted rate constants fit to eq 3.19 at each pulse energy and duration are indexed in Tables 4.2 (k_1) and 4.3 (k_2). Reported errors denote the rate constant standard deviations across more than five different experiments, which were conducted on at least three separate days. The kinetics results for pulses with positive and negative chirp (200 fs duration; light and dark green curves in Figures 5.9f and 4.3) are the same, which indicates that the direction of chirp has no effect on the kinetics. The discussion for this chapter only examines the results for negatively chirped pulses. The significance of the relations between the k_1 and k_2 values and the peak irradiance I will be discussed individually in Sections 4.3.1 and 4.3.2.

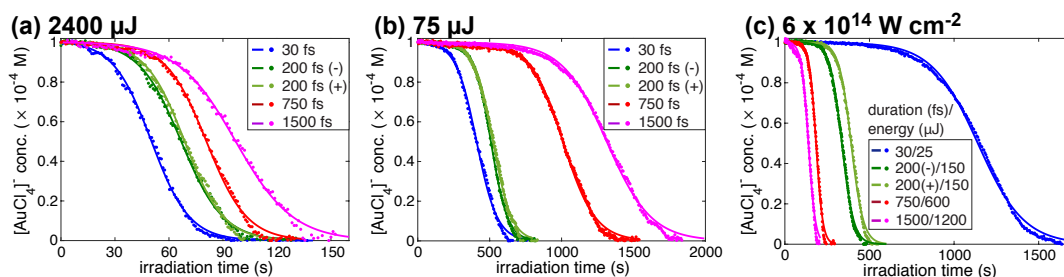


FIGURE 4.3: Representative plots of $[\text{AuCl}_4]^-$ versus irradiation time (circles), with fits to eq 3.19 (solid lines) for pulses with duration 30 fs (blue), 200 fs (negative/positive chirp, dark/light green), 750 fs (red), and 1500 fs (magenta). Panel (a) contains data for the 2400 μJ pulses, (b) is the 75 μJ pulses, and (c) shows normalized $I=6 \times 10^{14} \text{ W cm}^{-2}$ pulses.

E (μJ)	30 fs	200 fs (-)	200 fs (+)	750 fs	1500 fs
2400	$8 \pm 3 \times 10^{-4}$	$1.9 \pm 0.8 \times 10^{-4}$	$2 \pm 1 \times 10^{-4}$	$8 \pm 5 \times 10^{-5}$	$1.4 \pm 0.2 \times 10^{-4}$
1200	$4 \pm 2 \times 10^{-4}$	$9 \pm 5 \times 10^{-5}$	$9 \pm 5 \times 10^{-5}$	$5 \pm 2 \times 10^{-5}$	$7 \pm 2 \times 10^{-5}$
600	$3 \pm 1 \times 10^{-4}$	$5 \pm 2 \times 10^{-5}$	$6 \pm 4 \times 10^{-5}$	$3 \pm 1 \times 10^{-5}$	$3 \pm 1 \times 10^{-5}$
300	$1.4 \pm 0.5 \times 10^{-4}$	$3 \pm 1 \times 10^{-5}$	$3 \pm 2 \times 10^{-5}$	$1.1 \pm 0.6 \times 10^{-5}$	$1.0 \pm 0.6 \times 10^{-5}$
150	$7 \pm 3 \times 10^{-5}$	$9 \pm 5 \times 10^{-6}$	$1.0 \pm 0.9 \times 10^{-5}$	$5 \pm 4 \times 10^{-6}$	$3 \pm 2 \times 10^{-6}$
75	$1.6 \pm 0.8 \times 10^{-5}$	$3 \pm 2 \times 10^{-6}$	$3 \pm 2 \times 10^{-6}$	$1.4 \pm 0.9 \times 10^{-6}$	$1.1 \pm 0.9 \times 10^{-6}$
50	$8 \pm 6 \times 10^{-6}$	$1.9 \pm 0.8 \times 10^{-6}$	$1.3 \pm 0.9 \times 10^{-6}$	$9 \pm 6 \times 10^{-7}$	$6 \pm 4 \times 10^{-7}$
25	$2 \pm 1 \times 10^{-6}$	$5 \pm 4 \times 10^{-7}$	$7 \pm 6 \times 10^{-7}$	$2 \pm 1 \times 10^{-7}$	
10	$5 \pm 4 \times 10^{-7}$				

TABLE 4.2: Values of rate constant k_1 from eq 3.19. Units are s^{-1} .

E (μJ)	30 fs	200 fs (-)	200 fs (+)	750 fs	1500fs
2400	1.00 ± 0.08	0.89 ± 0.06	0.92 ± 0.04	0.92 ± 0.07	0.73 ± 0.07
1200	0.64 ± 0.09	0.65 ± 0.05	0.59 ± 0.04	0.64 ± 0.06	0.50 ± 0.02
600	0.41 ± 0.05	0.45 ± 0.03	0.46 ± 0.06	0.42 ± 0.03	0.32 ± 0.03
300	0.31 ± 0.03	0.36 ± 0.04	0.32 ± 0.6	0.27 ± 0.03	0.18 ± 0.02
150	0.22 ± 0.02	0.24 ± 0.02	0.21 ± 0.03	0.18 ± 0.02	0.126 ± 0.008
75	0.14 ± 0.02	0.15 ± 0.03	0.13 ± 0.02	0.10 ± 0.01	0.072 ± 0.006
50	0.113 ± 0.008	0.12 ± 0.02	0.10 ± 0.02	0.077 ± 0.008	0.037 ± 0.002
25	0.074 ± 0.009	0.067 ± 0.005	0.057 ± 0.009	0.053 ± 0.004	
10	0.043 ± 0.006				

TABLE 4.3: Values of rate constant k_2 from eq 3.19. Units are $\text{mM}^{-1} \text{s}^{-1}$.

4.2.1 Products

The particles were characterized for their sizes and size-distributions by comparing the SPR peaks of the finished AuNP colloids to their corresponding TEM images. Figure 4.4a-d shows the final UV-vis spectra of AuNPs produced with 30 fs; 200 fs; 750 fs; and 1500 fs pulse durations over the 25-2400 μJ range of pulse energies. For all pulse durations, an increase of the SPR peak-height is observed as the laser energy is decreased, corresponding to an increase in spherical AuNP diameter [124]. There is also SPR peak-broadening wavelength redshift in the AuNPs formed with lower laser energies, suggesting not only that the AuNP sizes are increasing, but that the particles are agglomerating [25, 124].

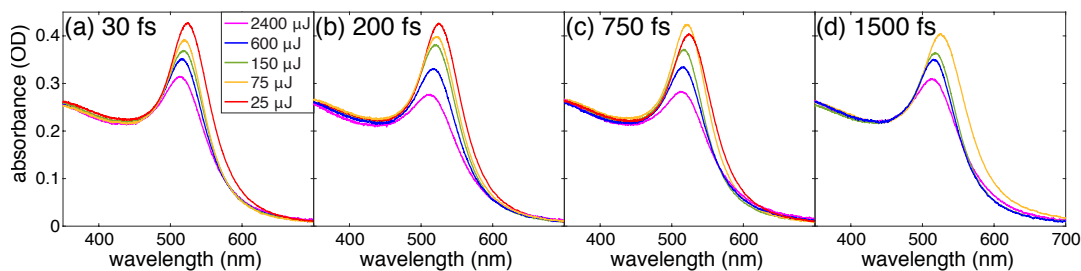


FIGURE 4.4: UV-vis spectra, recorded post-completion of aqueous KAuCl_4 irradiation, with pulse durations of 30 fs (a); 200 fs, negative chirp (b); 750 fs (c); and 1500 fs (d). The spectra recorded at different laser energies are indicated by the colors associated with the legend in panel (a).

The trends of increasing AuNP size and agglomeration are also observed in the TEM images displayed in Figure 4.5. The histograms and average AuNP sizes displayed were calculated from ~ 500 AuNPs per sample, using ImageJ software. The average AuNP sizes vary within a 2.7 – 6.4 nm diameter range, with some distributions having very broad

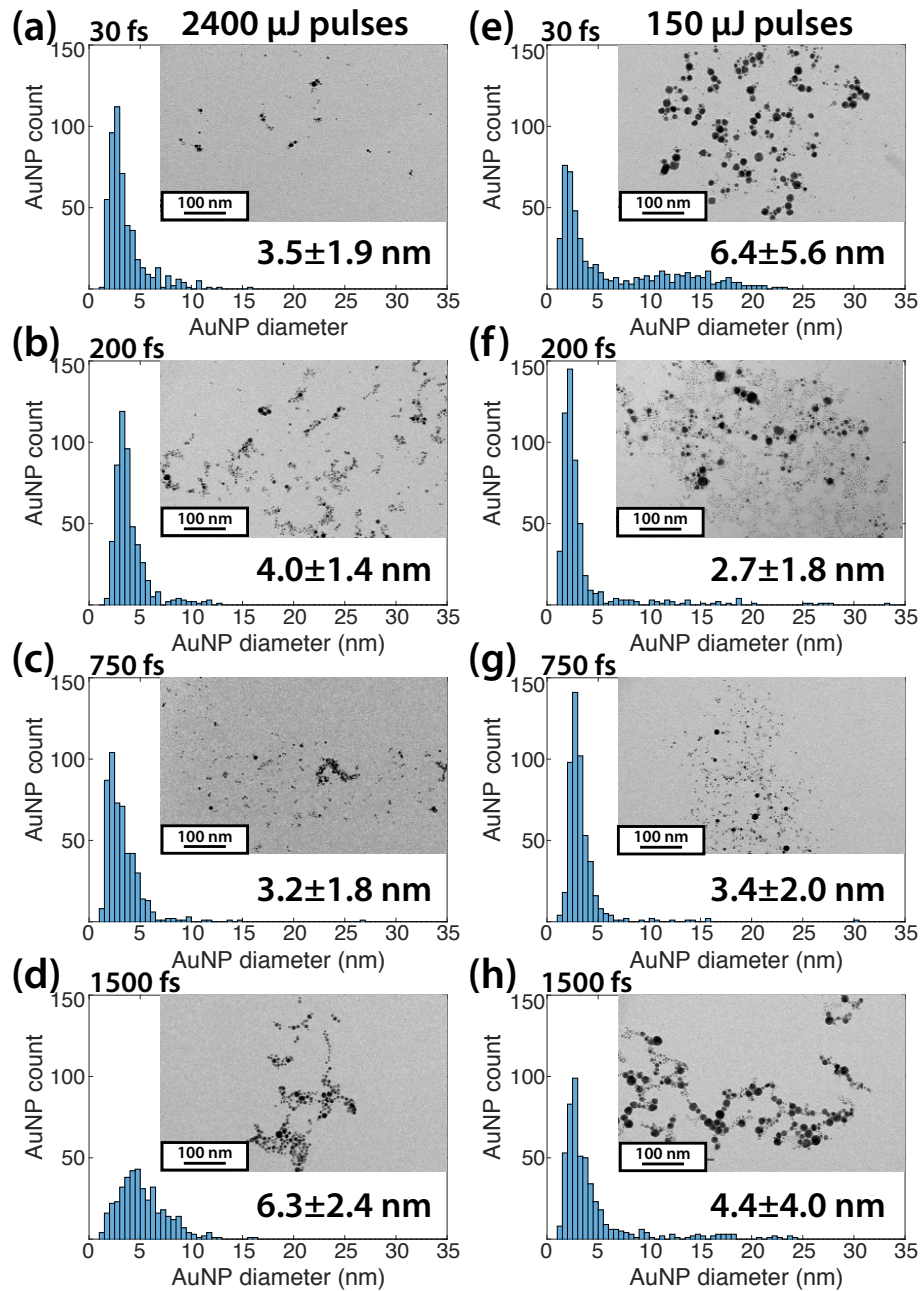


FIGURE 4.5: Representative TEM images and corresponding size-distribution histograms of AuNPs produced using $2400 \mu\text{J}$ with $\tau_p = 30 \text{ fs}$ (a), 200 fs negative chirp (b), 750 fs (c), 1500 fs (d); and $150 \mu\text{J}$ for $\tau_p = 30 \text{ fs}$ (e), 200 fs negative chirp (f), 750 fs (g), and 1500 fs (h). All size-distribution histograms were obtained by counting ~ 500 particles with ImageJ software.

standard deviations. Although there is no distinct trend between the average AuNP sizes at the two laser energies, visual observation of the TEM images shows that the AuNPs produced at 150 μJ contain larger AuNPs than their 2400 μJ counterparts for each τ_p .

The AuNPs formed with the 2400 μJ pulses had narrower size distributions and standard deviations (Figure 4.5a-d) relative to the AuNPs formed with the 150 μJ pulses (Figure 4.5e-h). While the particle size distributions in Figure 4.5e-h all exhibit tails that spread out toward larger diameters, the particle size increased most significantly for 30 fs pulses (Figure 4.5e). Histogram (e) shows a bimodal size distribution with a very distinct population around 2 – 3 nm and second much more broad population around 12 nm, suggesting that small AuNPs (with 2 – 3 nm diameters) start to agglomerate into masses with 12 nm average diameters. These observations align with the broadened SPR peak in Figure 4.4, and the redshifted tail forming for all spectra associated with AuNPs produced with low beam energy using any pulse duration. This observed AuNP size-increase associated with low pulse energies is consistent with results obtained from a study using 36 ps pulses and the addition of a capping-agent to help control size: the AuNP diameters increased from 5.8 ± 1.1 nm when $E_p = 1800$ μJ to 9.6 ± 2.7 nm when $E_p = 400$ μJ [25]. At the highest pulse energy, 2400 μJ , AuNPs formed with the long, 1500 fs pulse (Figure 4.5d) are noticeably larger than those formed at all other τ_p (30 – 750 fs, Figure 4.5a-c). With sufficiently high energy, long pulses may produce slightly larger AuNPs, which agrees with previous results showing 4.8 ± 1.9 nm AuNP formation when a 0.1 mM Au^{3+} solution with a similar pH was irradiated using 2500 μJ , 36 ps laser pulses [63]. Collectively, these results suggest that both the pulse energy and duration may be exploitable for size and dispersity control of AuNPs.

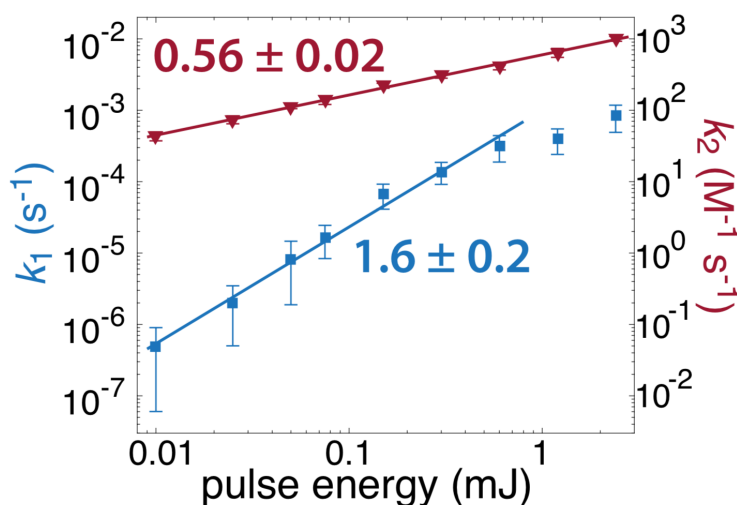


FIGURE 4.6: As pulse energy decreases, the difference between k_1 and k_2 increases as k_1 becomes disproportionately slower at low energies.

Figure 4.6 illustrates the effect of decreasing pulse energy on k_1 (blue ■) and k_2 (maroon ▼). At high E_p , the difference between the two rate constants is not terribly pronounced. As E_p drops, the difference between the two values becomes much more dramatic as the nucleation rate plummets, but the rate of particle growth only decreases slightly. We also found that as this discrepancy became larger, AuNP products became more polydisperse. This is likely because nuclei formation is too slow to guarantee stable, plentiful metal cluster generation, but for any nuclei that are stable, they are being grown at a comparatively fast pace.

4.3 Discussion

The primary importance of water photolysis in OB microplasmas to the photochemical reduction of Au^{3+} and other metal ions is well-established [22, 24, 63, 66, 70, 72, 73]. While both hydrated electrons and hydrogen radicals are capable of reducing Au^{3+} , the fast consumption of $\text{H}\cdot$ via eq 3.6 observed in water photolysis with picosecond pulses [94] suggests that the contribution of $\text{H}\cdot$ to the Au^{3+} reduction rate is negligible. Hydrated electrons, however, are produced both from the free electrons generated in OB plasma via eq 3.2 within a few hundred femtoseconds [95, 96], and from the reaction between water and $\text{H}\cdot$ via eq 3.6. Hydrated electrons have lifetimes of hundreds of nanoseconds in pure water [97] and react with Au^{3+} with a diffusion-controlled rate constant of $6.1 \times 10^{10} \text{ M}^{-1} \text{ s}^{-1}$ [125]. Hydrated electrons, e_{aq}^- , are therefore expected to be the dominant Au^{3+} reducing agent, via eq 3.21 [73].

In addition to Au^{3+} reduction by e_{aq}^- , the H_2O_2 generated in eq 3.5 can reduce Au^{3+} in the presence of AuNPs [22, 63, 126, 127, 147] through the autocatalytic reaction eq 3.22. The formation of electrons in the OB microplasma is directly proportional to the observed value of the first-order rate constant k_1 in eq 3.19, and the formation rate of H_2O_2 parallels the value of the k_2 rate constant.

4.3.1 Nucleation

The experimental k_1 values from Table 4.2 for pulses with $\tau_p = 30$ fs (blue \circ), 200 fs (green ∇), 750 fs (red \square), and 1500 fs (magenta \diamond) are plotted as functions of I in Figure 4.7a. For pulse energies of 600 μJ and below (1200 μJ for 1500 fs pulses), the k_1 values were fit to linear functions in log-log space (solid lines, Figure 4.7a) and the resulting slopes are listed in the legend. The slopes are all approximately 1.5, which is consistent with the slope of the calculated plasma volumes with peak intensity (Figure 3.8d). This result indicates that the k_1 values are related to the volume of the OB plasma in which ρ_e exceeds the critical threshold of $1.8 \times 10^{20} \text{ cm}^{-3}$ (Section 3.1.2).

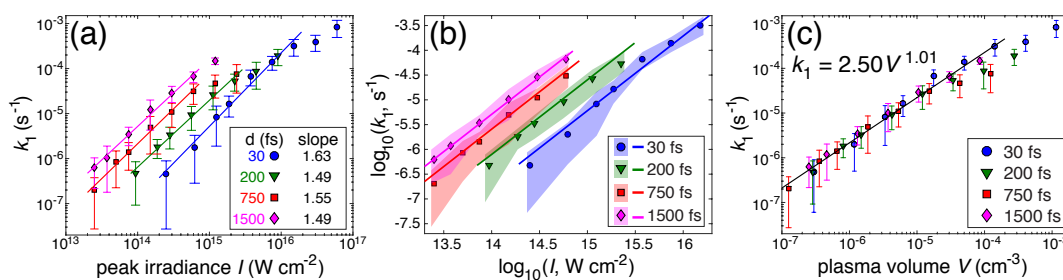


FIGURE 4.7: Rate constant k_1 as a function of peak laser intensity I for each pulse duration (a) and overlaid with calculated plasma volumes (solid lines, b). Rate constant k_1 versus calculated plasma volume, showing a direct correlation with the power law of 1.01 (c).

To further explore the link between the plasma volume and k_1 value, the calculated plasma volumes were compared directly to the k_1 values by plotting both quantities as functions of I in log-log space (Figure 4.7b). The plasma volumes (solid lines) are shifted by 0.4 units on the y -axis to most closely match the experimental k_1 values (colored symbols) and error ranges (transparent shaded regions). Importantly, the relative spacing of

the plasma volumes for each pulse duration from Figure 3.8d was not changed in Figure 4.7b, showing that the same relationship between plasma volume and k_1 value holds, regardless of τ_p . To confirm this assertion, the experimental k_1 values were plotted as functions of calculated plasma volume at the same τ_p and I values (Figure 4.7c), with the best fit equation for E_p below 600 μJ (black solid line) confirming the direct proportionality of plasma volume with k_1 values. At high pulse energies, k_1 values are lower than would be expected on the basis of plasma volume, implying electron saturation—likely due to **intensity clamping**, which occurs at high powers [49, 50, 81].

4.3.2 Autocatalytic Growth

While the **contribution of H_2O_2** to the formation of gold nanoparticles by photochemical reduction of Au^{3+} has been well-documented [22, 25, 63–65, 127, 147], a quantitative relationship between H_2O_2 formation rate and the autocatalytic reduction rate has yet to be established. For each experimental pulse duration, for pulse energies of 150 μJ and above, the amount of H_2O_2 generated from 180s of focused laser irradiation in pure water was **quantified** using titanium sulfate titrations. The formation rate of H_2O_2 was extracted from these measurements based on the previously observed linear increase in H_2O_2 concentration with irradiation time upon femtosecond laser irradiation of pure water [22].

The k_2 values for pulses with duration 30 fs (blue \circ), 200 fs (green ∇), 750 fs (red \square), and 1500 fs (magenta \diamond) are plotted as functions of I in Figure 4.8a. For each pulse duration, the growth of k_2 with I was fit to a linear function in log-log space (solid lines on Figure 4.8a); the resulting slopes are indicated in the legend. The k_2 values exhibit a weaker dependence on peak irradiance I than the k_1 values, with the values growing as $k_2 \sim I^{0.5} - I^{0.6}$, depending on τ_p ; as opposed to $k_1 \sim I^{1.5}$. The formation rate of H_2O_2 exhibits a stronger dependence on the peak irradiance at all pulse durations, with $[\text{H}_2\text{O}_2] \sim I$ (Figure 4.8b). As a result, the k_2 values grow with H_2O_2 concentration, but approximately as $k_2 \sim [\text{H}_2\text{O}_2]^{0.5}$ (Figure 4.8c).

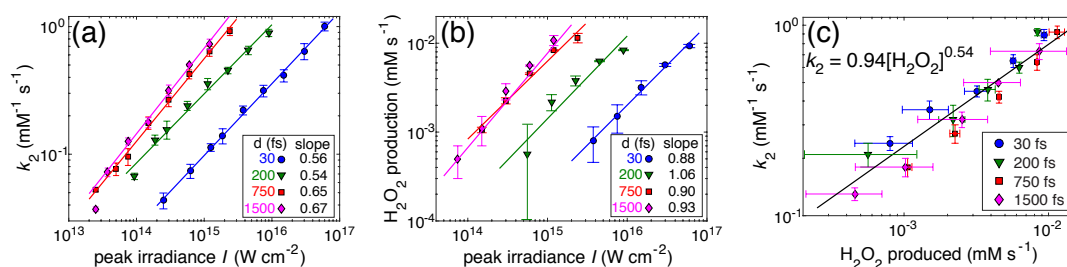


FIGURE 4.8: Rate constant k_2 as a function of peak laser intensity I for each pulse duration (a). Hydrogen peroxide formation-rate as a function of I (b). Rate constant k_2 versus H_2O_2 formation-rate (c).

Beam-Focus and Size-Distribution

Studies on focusing-conditions have demonstrated that increasing the pulse energy reduces AuNP size [25, 62]. When tight-focusing geometry was used in the experiment in Chapter 3, increasing the energy of a 30 fs pulse from 0.15 mJ to 2.4 mJ decreased AuNP size from 6.4 ± 5.6 nm to 3.5 ± 1.9 nm (Figure 4.9a,b). This trend was also seen

when LDP conditions were used: increasing the energy of 30 fs pulses from 2.7 mJ to 3.3 mJ reduced AuNP size from 27 ± 7 nm to 14 ± 6 nm [62] (Figure 4.9c,d). These results are consistent with earlier reports using SSTF with 36 ps pulses to irradiate solutions of $[\text{AuCl}_4]^-$ and polyethylene glycol, a capping agent. Increasing E_p from 0.45 mJ to 1.8 mJ reduced the average particle size from 9.6 ± 2.7 nm to 5.8 ± 1.1 nm [25].

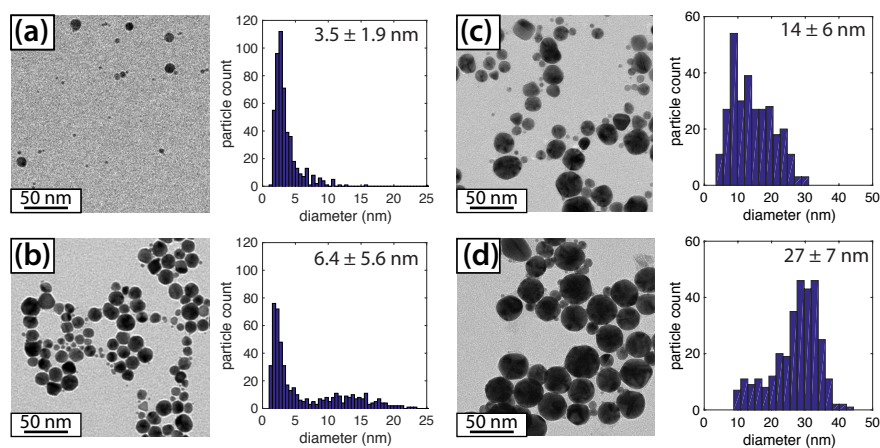


FIGURE 4.9: Representative TEM images and histograms for AuNP synthesized with 30 fs pulses under the following conditions: (a) tightly-focused beam, 2.4 mJ; (b) tightly-focused beam, 0.15 mJ; (c) LDP, 3.3 mJ; and (d) LDP, 2.7 mJ.

While E_p strongly influences the size of the AuNPs from photochemical reduction of Au^{3+} ; τ_p , or linear frequency chirp, has *at most* a modest effect on the AuNP size at fixed E_p and focusing condition [25, 69]. Under tight-focusing conditions, τ_p was stretched from 30 fs to 1500 fs (negatively chirped) at a 0.15 mJ pulse energy slightly decreased the AuNP sizes from 6.4 ± 5.6 nm to 4.4 ± 4.0 nm [69]. When the experiment was repeated at a high pulse energy (2.4 mJ), the AuNP size increased from 3.5 ± 1.9 nm for 30 fs pulses to 6.3 ± 2.4 nm for 1500 fs pulses [69]. In a separate experiment using low-NA focusing conditions, 1.8 mJ pulses with chirp coefficients of $+20,000 \text{ fs}^2$, 0 fs^2 , and $-20,000 \text{ fs}^2$ (corresponding to 35 fs unchirped pulses and 2 ps chirped pulses) produced 8.2 ± 3.5 nm, 8.1 ± 3.4 nm, and 8.1 ± 6.5 nm AuNPs, respectively [25]. Collectively, these results suggest that for sufficiently high peak-intensities generating OB conditions, the pulse duration does not significantly affect the size of AuNPs produced by photochemical reduction of Au^{3+} .

4.4 Summary

In this experiment, we found that the dimensional product outcomes had much to do with the way each of the two rate laws changed in relation to each other. The parameter associated with k_1 , electron density, was directly connected to plasma volume and could be controlled by adjusting the pulse energy; but k_2 responded much more dramatically to changes in overall intensity. When k_1 decreased too much in relation to k_2 we saw particle agglomeration, which rendered our colloidal products polydisperse. When k_1 is allows fast nucleation, there are multiple, small gold atom clusters onto which k_2 can autocatalytically build nanoparticles. If k_2 can be slowed to an extent where nuclei can be stabilized into NPs before they agglomerate and compromise size-dispersity, an ideal, small-diameter, monodisperse AuNP colloid might be achieved—which we will pursue in

the second part of Chapter 5. However, before we examine the fine-tuning possibilities of AuNP laser synthesis, we look at the photoreduction obstacles associated with Ag^+ in the first part of Chapter 5. Silver atoms are oxidized by H_2O_2 , but silver does not reduce according to the Finke-Watzky mechanism. To confirm the usefulness of metallic nanoparticle synthesis with ultrafast laser photoreduction, it is practical to show that this method is applicable to metals apart from gold.

Chapter 5

Radical Scavenger Studies

The reactive species produced through water photolysis are what drive metal cation reduction during laser-assisted nanoparticle formation. Scavengers can selectively hinder the production of water photolysis byproducts such as H_2O_2 , so they have been used to control reduction kinetics [72]. In the case of silver, H_2O_2 formed by hydroxyl radical recombination in eq 3.5 inhibits particle development by back-oxidizing Ag^0 to its ionic form. To address this problem, we added $OH\cdot$ scavengers to our silver precursor solutions, with the goal of hindering H_2O_2 formation and stopping AgNP deterioration. Because AuNP morphology is also influenced by the concentration of H_2O_2 as determined in Chapter 4; experiments were also performed in which radical scavengers were added to gold precursor solutions to slow autocatalytic particle growth.

5.1 Silver

All solutions in this study were irradiated using a tightly focused high-NA geometry and $I = 2.5 \times 10^{16}$ pulses.

5.1.1 Ammonia

The radical scavenger of interest in this study was liquid ammonia; although other scavengers such as isopropyl alcohol have been used as reducing agents to assist the formation of AgNPs [128, 132]. Initially, we ran experiments with both ammonia solution and sodium acetate, but found in our preliminary trials that acetate gave less dramatic¹ results than did ammonia solution, and worked with silver under a much narrower range of conditions than ammonia did. There are already examples of IPA being used as a scavenger for AgNP formation [148]. Previous studies reported complexation of the Ag^+ ion with ammonia to form $Ag(NH_3)_2^+$ [145, 149]. The Herbani research group [131] credits ammonia with enabling the formation AgNPs. The lower reduction-potential of $Ag(NH_3)_2^+$ compared to uncomplexed Ag^+ [145] is the main indicator that manipulating NH_3 concentration can predictably alter AgNP growth rates, and resulting AgNPs morphologies.

¹Ultimately, the decision to examine ammonia solution only was arbitrary. It was decided that focusing on one scavenger to begin with was a wiser course of action than running a comparative study. As I am writing this thesis (summer 2019) there are currently other graduate students in Tibbetts lab examining the combinations of gold with sodium acetate, and silver with IPA, in greater detail.

5.1.2 Results

Precursor solutions containing AgNO_3 were irradiated with focused femtosecond pulses. For solutions without NH_3 , AgNP formation was erratic. If any particles formed, they agglomerated quickly and precipitated out of solution; but it was more likely that no AgNPs would form at all (Appendix D D.1a). These results were expected [131], because hydrogen peroxide back-oxidizes Ag^0 to Ag^+ [86, 128, 129], arresting AgNP synthesis [130, 131] by deteriorating and destabilizing forming NPs. This process can be observed through the low final concentration of H_2O_2 in an irradiated 0.1 mM AgNO_3 solution, compared to pure irradiated water (Appendix D, D.1b). Adding NH_3 to AgNO_3 solutions enabled AgNPs to form. Their growth rate and physical characteristics are reliant on NH_3 concentration.

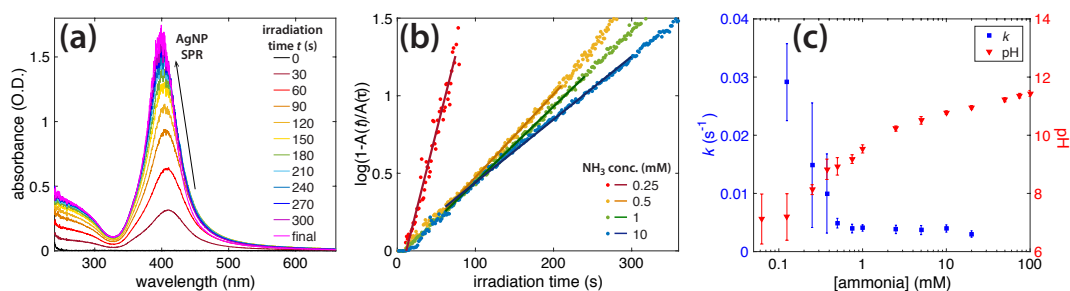


FIGURE 5.1: The developing absorbance peak of AgNPs in 1 mM NH_3 during irradiation (a). AgNP formation rates in different concentrations of ammonia (b). Rate constant as a function of NH_3 concentration, overlaid with the initial pH of Ag- NH_3 solutions (c).

Figure 5.1a shows the AgNP SPR peak-growth at around 400 nm, with irradiation time t for a 1 mM NH_3 sample. Plasmon growth stops at 300 s, indicating complete conversion of Ag^+ to AgNPs. Figure 5.1b shows the rate of AgNP SPR growth in different NH_3 concentrations as a semi-log plot, according to eq 5.1. The AgNP growth-rate constant k is extracted from the slope of the least-squares fit line, according to eq 5.1. Surprisingly, the fastest growth occurs at lower concentrations of NH_3 , and as more NH_3 is added, the kinetics slow. Figure 5.1c shows both the AgNP growth-rate k , and initial solution pH as functions of NH_3 concentration. Numerical values are provided in Appendix D, Table D.2.

Irradiation of Ammonia Solutions

To obtain the baseline rate of H_2O_2 generation under these experimental conditions, water samples were irradiated for $t = 60 - 600$ s, and titanium(IV) sulfate was added to the samples afterwards. Figure 5.2a shows the absorption spectrum of $\text{TiO}_2\text{H}_2\text{O}_2$ formed after specified times (0–300 s). The increased absorbance at ~ 400 nm with irradiation time reflects the production of H_2O_2 [69, 88]; which is produced in higher quantities as irradiation proceeds. Figure 5.2b shows the H_2O_2 concentration as a function of irradiation time, t . Experimental data were fit to both linear (green) and power (blue) functions, by nonlinear least-squares methods. The power law gives a closer fit, demonstrating that H_2O_2 concentration grows relative to time as $t^{0.8}$. The sub-linear growth of H_2O_2 concentration could result from H_2O_2 molecule-fragmentation within the laser plasma; or a reaction between hydrogen peroxide and additional $\text{OH}\cdot$; or possibly both.

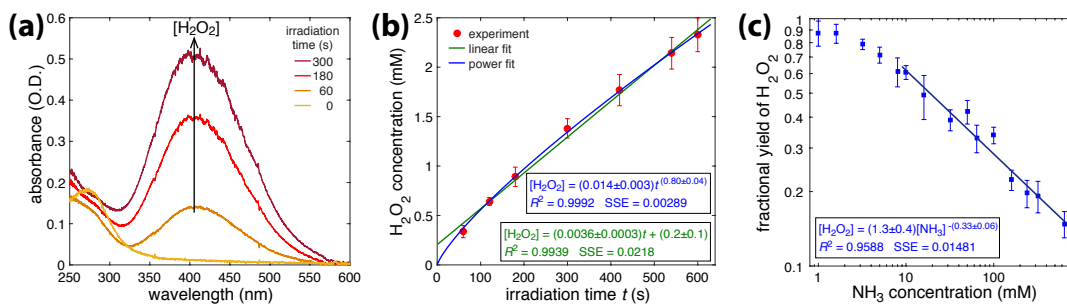


FIGURE 5.2: Absorption spectrum of the $\text{TiO}_2\text{H}_2\text{O}_2$ complex formed after adding titanium(IV) sulfate to irradiated water (a). Hydrogen peroxide concentration vs. irradiation time (b). Experimental data points (red) fit with with linear (green) and power (blue) functions. Log-log plot of fractional H_2O_2 yield vs. NH_3 concentration, with linear fit a 10–600 mM NH_3 range (c). The error bars in (b) and (c) denote standard deviation over four independent experiments.

To quantify the radical-scavenging capabilities of ammonia, NH_3 solutions (1–600 mM) were irradiated for 300 s and the H_2O_2 concentrations were quantified with titanium(IV) sulfate. The fractional yields of H_2O_2 produced at different NH_3 concentrations, relative to the yield in irradiated pure water for the same duration, is shown in Figure 5.2c. The corresponding numerical values are reported in Table D.1 of Appendix D. There is a linear fit to the log-log data in the range of 10 to 600 mM NH_3 , allowing us to describe the concentration of hydrogen peroxide as $[\text{H}_2\text{O}_2] \sim [\text{NH}_3]^{-0.33}$. This relationship confirms that ammonia reacts with $\text{OH}\cdot$, or H_2O_2 , or both; and that the yield of H_2O_2 decreases as ammonia concentration rises.

An unexpected absorbance peak emerged when solutions containing ≥ 10 mM NH_3 were irradiated. This species absorbed at 302 nm; its absorption peak rose during laser-beam interaction with the medium, and disappeared again once the laser was turned off. Figure 5.3a shows UV-vis spectra collected at 60 s intervals during the irradiation of a 10 mM NH_3 solution. A growth-rate constant, k_g , may be calculated using the slope

$$-\log_{10} \left(1 - \frac{A_t}{A_{600}} \right) = k_g t \quad (5.1)$$

where A_t is the 302 nm absorbance at time t (s), and A_{600} is the 302 nm absorbance after 600 s. To prevent the quantity on the left side of eq 5.1 to become unwieldy as $t \rightarrow 600$ s, the reference quantity, A_{600} , was taken to be the mean value plus standard deviation obtained over four experiments. The inset in Figure 5.3a shows a plot of eq 5.1 over time for both 10 and 100 mM NH_3 solutions, with $k_g = 1.8 \pm 0.1 \times 10^{-3} \text{ s}^{-1}$. Raising the NH_3 concentration above 10 mM did not affect the growth rate; the absorbance values in the Figure 5.3a inset overlap for both 10 and 100 mM ammonia solutions. Therefore, the growth of the 302 nm peak is likely zeroth order with respect to NH_3 within the concentration range of 10–100 mM.

When irradiation was stopped, the 302 nm absorbance-peak slowly sank and disappeared. Figure 5.3b shows spectra from a 10 mM ammonia solution, collected every 300 s after the initial 600 s irradiation. The decay rate constant, k_d , may be calculated by extracting the slope of

$$\log_{10} \left(\frac{A_t}{A_0} \right) = k_d t \quad (5.2)$$

where A_t is the deteriorating 302 nm absorbance and A_0 is the 302 nm absorbance immediately following irradiation. The inset in Figure 5.3b shows the decaying 302 nm peak for 10 mM and 100 mM NH_3 solutions. The linear region (1000 s for 100 mM and 1500 s for 10 mM NH_3) shows a decay rate constant value of $k_d = 4.6 \pm 0.3 \times 10^{-4} \text{ s}^{-1}$. The most likely chemical species behind this 302 nm peak is peroxyxynitrite, ONOO^- , which is known to absorb at 302 nm [150, 151]. Further discussion of the radical reactions leading to the formation of this transient product is presented in Section 5.1.3.

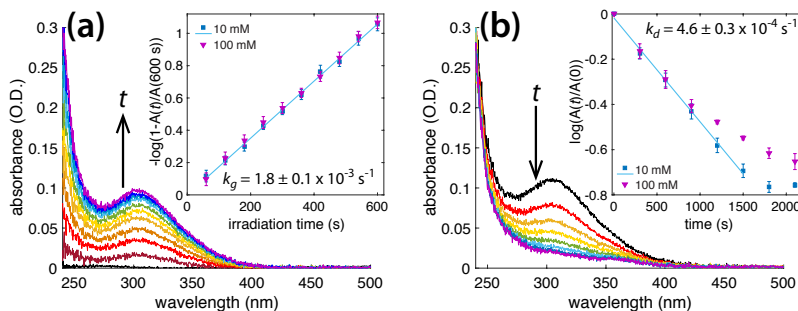


FIGURE 5.3: Absorbance spectra, taken every 60 s during irradiation of 10 mM NH_3 solution (a). Inset: eq 5.1 plotted for 10 and 100 mM NH_3 solutions vs. irradiation time, with linear least-squares fit. Absorbance spectra, taken every 300 s following termination of initial 600 s laser irradiation of 10 mM NH_3 solution (b). Inset: eq 5.2 plotted for 10 and 100 mM NH_3 with linear least-squares fit.

AgNP Products

Figure 5.4a shows the final AgNP absorbance spectra for products synthesized with different concentrations of NH_3 . Kinetics were fast at 0.25 mM and slow at 10 mM, relative to the kinetics of formation in 1 mM solution (Figure 5.1b). The SPR absorbance peaks for the products formed at both 0.25 and 10 mM NH_3 are redshifted, broad, and lower than the SPR peak of the 1 mM sample, suggesting that these two concentrations formed larger nanoparticles, possible with worse size-distributions and more agglomeration. Figure 5.4b shows the relationship between the AgNP SPR absorbance and wavelength for each of the NH_3 concentrations. The SPR peak with the highest absorbance and the most blueshift is the 1 mM NH_3 sample; therefore this concentration is optimal for producing small, monodisperse AgNPs.

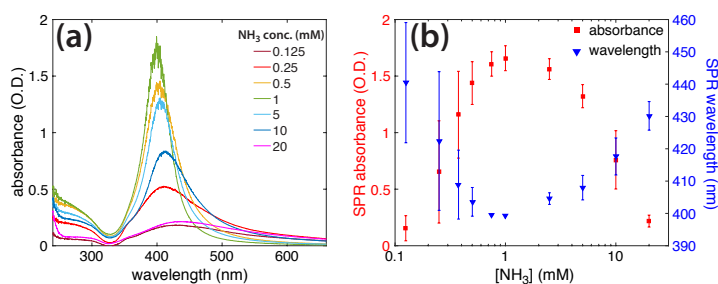


FIGURE 5.4: Absorbance spectra of AgNPs prepared with different (labeled) amounts of NH_3 (a). SPR absorbance (red, left) and SPR wavelength (blue, right) as functions of NH_3 concentration (b).

TEM analysis of AgNP products agrees with the absorption spectra. Figure 5.5 contains representative TEM images of AgNPs prepared with (a) 0.25, (b) 1, and (c) 10 mM NH_3 . At the optimal 1 mM concentration, AgNPs have a mean size of 12.7 ± 4.9 nm. This size distribution is more monodisperse than a previous report of 10.3 ± 8.5 nm AgNPs synthesized by femtosecond laser-irradiation of solutions containing AgNO_3 , NH_3 , and PVP as a capping agent [131], although no capping agent was used in our experiment. Lower NH_3 concentrations, in which the kinetics are faster, yielded large, amorphous plate-like particles. Higher concentrations yielded particle agglomerations in a variety of shapes, including star-like structures. There are additional TEM images in Appendix D, Figures D.3 through D.5.

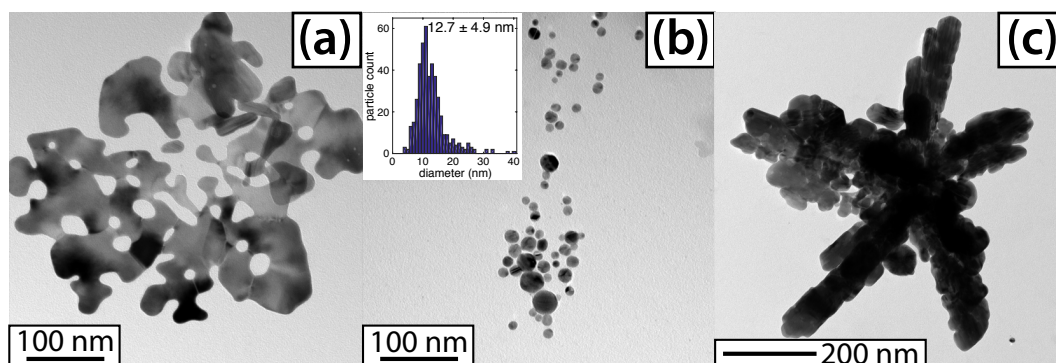


FIGURE 5.5: TEM images of AgNPs produced in (a) 0.25, (b) 1, and (c) 10 mM NH_3 . The histogram overlay corresponds to panel (b).

5.1.3 Discussion

We demonstrated in Section 5.1.2 that adding liquid ammonia to water reduces the amount of H_2O_2 produced in OB plasma (Figure 5.2c). This result confirms that ammonia is an effective $\text{OH}\cdot$ and H_2O_2 scavenger—which agrees with literature [152–154]. For ammonia solutions ≥ 10 mM and higher, an absorbance peak centered at 302 nm appeared during irradiation and then slowly disappeared when the laser was turned off (Figure 5.3a,b). The 302 nm absorbance is likely peroxyxynitrite, ONOO^- (which absorbs at 302 nm) [76, 142, 150, 151, 153–156]. The goal of this section is to explore the possible reactions involved between NH_3 and $\text{OH}\cdot$ or H_2O_2 which occur during multiphoton absorption in water. The relevant reactions taken from literature are summarized in Table 5.1.

Reactions involving ammonia in the laser plasma are most likely initiated by the hydroxyl radicals (reaction 1 in Table 5.1). Previous research shows that NH_3 reacts with H_2O_2 only when a solution is irradiated with UV light to produce $\text{OH}\cdot$ [154]. Subsequent reactions of the NH_2 radical can yield hydroxylamine (NH_2OH , reaction 2) and hydrazine (N_2H_4 , reaction 3); which are known to reduce Ag^+ ions and form AgNPs [167, 168]. Although hydroxylamine and hydrazine were not detected in our experiments, it is possible that they were formed in small quantities and contributed in part to Ag^+ reduction. The NH_2 radicals can also react with H_2O_2 and O_2 , eventually forming nitrous acid (HNO_2) and nitrate (NO_3^-), shown in reactions 4–8. Nitrate can scavenge hydrated electrons (reaction 9); and nitrite (NO_2^-) and nitrate both form peroxyxynitrous acid (ONOOH) or peroxyxynitrite (ONOO^-) through reactions 10–12. In the pH range of 10.62–11.42 where we see what we think is ONOO^- (Table D.1 of Appendix D), any peroxyxynitrous acid formed

Reaction No.	Equation	Rate Constant ($M^{-1}s^{-1}$)	Ref
1	$NH_3 + \cdot OH \longrightarrow \cdot NH_2 + H_2O$	1×10^8	[157]
2	$\cdot NH_2 + \cdot OH \longrightarrow NH_2OH$	9.5×10^9	[157]
3	$2 \cdot NH_2 \longrightarrow N_2H_4$		[158]
4	$\cdot NH_2 + H_2O_2 \longrightarrow \cdot NHOH + H_2O$	9×10^7	[157]
5	$\cdot NH_2 + O_2 \longrightarrow \cdot NH_2O_2$		[159]
6	$\cdot NH_2O_2 + \cdot OH \longrightarrow HNO_2 + H_2O$		[159]
7	$NO_2^- + \cdot OH \longrightarrow \cdot NO_2 + OH^-$		[160]
8	$\cdot NO_2 + \cdot OH \longrightarrow NO_3^- + H^+$	1×10^{10}	[160]
9	$NO_3^- + e_{aq}^- \longrightarrow NO_3^{2-}$		[142]
10	$NO_2^- + \cdot OH \longrightarrow ONOOH$	4.5×10^9	[161]
11	$NO_2^- + H_2O_2 \longrightarrow ONOO^- + H_2O$		[76]
12	$NO_3^- + h\nu \longrightarrow ONOO^-$		[162]
13	$ONOO^- + h\nu \longrightarrow NO_3^-$	$0.9 s^{-1}$	[163]
13'	$ONOO^- \longrightarrow NO_3^-$	$\sim 10^{-5} s^{-1}$	[161]
14	$ONOO^- \longrightarrow NO_2^- + 1/2O_2$		[151]
15	$H_2O_2 \longrightarrow HO_2^- + H^+$	$pK_a = 11.6$	[164]
16	$HO_2^- + \cdot OH \longrightarrow OH^- + \cdot O_2H$	7.5×10^9	[165]
17	$HO_2^- + \cdot NH_2 \longrightarrow NH_2O_2\cdot + H^+$		[153]
18	$NH_2O_2\cdot \longrightarrow \cdot NO + H_2O$		[158]
19	$\cdot NO + \cdot OH \longrightarrow HNO_2$	8.9×10^9	[166]

TABLE 5.1: Proposed reactions, rate constants, and references for photolysis of water and ammonia.

through reaction 10 quickly deprotonates to peroxyxynitrite. Peroxyxynitrite has a pK_a of 6.7, and is somewhat stable in basic pHs [151, 169, 170]. It decays spontaneously according to reactions 13–19. To determine which reactions leads to $ONOO^-$ formation in the OB plasma, and to confirm that the species absorbing at 302 nm is $ONOO^-$, followup experiments were conducted.

Peroxyxynitrite Experiments

First, $NaNO_2$ (1 mM) and KNO_3 (0.05 mM) solutions, both with pH 10 (adjusted by adding KOH), were irradiated for 600 s under identical experimental conditions. Figure 5.6a shows the initial and final absorbance spectra of the KNO_3 solution (light and dark green) and the $NaNO_2$ solution (light and dark blue), along with the final absorption spectrum of irradiated NH_3 (red). Irradiated KNO_3 had a broad absorption increase below 350 nm, while irradiated $NaNO_2$ produced an absorption peak that was nearly identical to that of the irradiated NH_3 solution. This implies that nitrite, not nitrate, is the dominant $ONOO^-$ precursor in our experiments. The presence of both $OH\cdot$ and H_2O_2 in the OB plasma is consistent with both reactions 10 and 11 in Table 5.1, making them possible pathways to $ONOO^-$ formation.

Next, to verify that the species absorbing at 302 nm was peroxyxynitrite, we chemically synthesized $ONOO^-$ by following the procedure in ref [76] involving a reaction between acidic H_2O_2 and alkaline nitrite. Figure 5.6b compares the absorption spectrum of our chemically-synthesized $ONOO^-$ to one of a 10 mM NH_3 solution irradiated for 600 s. The spectra align at around 302 nm, suggesting that the unknown species is peroxyxynitrite. The shoulder-peak in the chemically-synthesized $ONOO^-$ spectrum (Figure 5.6b), centered at

~370 nm, is from remaining NO_2^- in the chemically-synthesized solution—it matches the absorbance of the initial 1 mM NaNO_2 solution in Figure 5.6a (light blue spectrum).

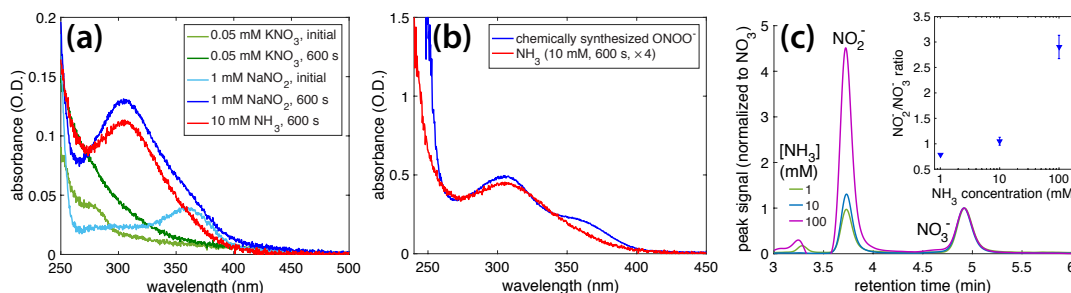


FIGURE 5.6: (a) Absorption spectra of initial and irradiated KNO_3 and NaNO_2 solutions, with irradiated NH_3 for comparison. Absorption spectra of irradiated NH_3 and chemically synthesized ONOO^- (b). Ion chromatograms overlaid for 1, 10, and 100 mM NH_3 solutions irradiated for 600 s (c). Peak heights normalized to NO_3^- peak (labeled). Inset shows $\text{NO}_2^-/\text{NO}_3^-$ peak height ratio as a function of NH_3 concentration.

Finally, to determine whether NO_2^- and NO_3^- were produced as the final products in our experiments, ion chromatography of irradiated NH_3 solutions was performed. Figure 5.6c shows overlaid ion chromatograms for three irradiated NH_3 solutions, normalized to the NO_3^- peak height. The inset in Figure 5.6c shows the $\text{NO}_2^-/\text{NO}_3^-$ peak-height ratio as a function of ammonia concentration, and reveals a dramatic increase in the amount of NO_2^- produced in the 100 mM NH_3 solution. This is consistent with previous reports of increased NO_2^- production relative to NO_3^- when high-pH NH_3 and H_2O_2 solutions are irradiated with UV light [142, 154]. Solution pH (11.42, Table D.1) could explain this result, as it is approaching the pK_a of 11.6 for H_2O_2 [154, 164]. The radical mediated reactions 15–19 in Table 5.1 occur near the pK_a of H_2O_2 , and produce HNO_2 as one of the products (reaction 19).

Kinetics

Our observed ONOO^- decay rate, $k_d = 4.6 \times 10^{-4} \text{ s}^{-1}$, is much higher than the reported thermal decay rates of 1.3, and $3.2 \times 10^{-5} \text{ s}^{-1}$ at pH 13 and 12 [161, 163]. While these differences might be caused by the lower pH range of 10.62–11.42 in our experiments, it is also possible that the long-lived photolysis products in our experiments accelerate ONOO^- decomposition. The presence of H_2O_2 is known to speed up the degradation of peroxyxynitrite [76], which makes it the likely cause of the fast decay. We note that our ONOO^- decay experiments, reported in Figure 5.3b, were carried out in darkness except for periodic UV-vis measurements of the absorption spectra, every 300 s, so photochemical decomposition according to reaction 12 [151] is unlikely to cause accelerated ONOO^- decay. In any case, the ultimate products of nitrite and nitrate (Figure 5.6c) suggest that our experiments follow similar mechanisms to those observed in previous reports about the conversion of ammonia to nitrite and nitrate through UV irradiation, in the presence of H_2O_2 [153, 154, 171].

It is difficult to interpret experimental observations related to the formation and decay mechanisms of peroxyxynitrite, so findings are controversial [151, 153–155, 158, 162, 163, 172]. Full discussions of the step-by-step mechanisms under different irradiation conditions is elaborated upon elsewhere [151, 154, 158, 172]. Our results demonstrate a new

way to form this species, and opens avenues to its further investigation on the ultrafast timescale.

The reactive species produced from ammonia photolysis, summarized in Table 5.1, assist the photochemical reduction of AgNO_3 to generate AgNPs; and the final AgNP morphology is determined in part by the ammonia concentration (Figure 5.5). No AgNP formation was observed when ammonia was not present (Appendix D, D.1). Since nitrate is known to readily accept hydrated electrons (reaction 9, Table 5.1) [142, 143], the nitrate group of the AgNO_3 precursor could be hindering AgNP formation. To test this contention, we irradiated solutions containing AgClO_4 (0.1 mM), a salt used in earlier radiolysis experiments because the ClO_4^- ion does not scavenge hydrated electrons [144–146]. Figure 5.7a shows absorption spectra of an AgClO_4 solution irradiated for 600 s, with no AgNP formation. When ammonia (1 mM) was added to the AgClO_4 solution and irradiated for 420 s, the 400 nm SPR absorption feature of AgNPs grew with irradiation time, at a rate constant of $k = 3.3 \pm 0.3 \times 10^{-3} \text{ s}^{-1}$ (Figure 5.7b), which is comparable to the rate constant of $k = 4.1 \pm 0.6 \times 10^{-3} \text{ s}^{-1}$ for AgNO_3 . Finally, the absorption spectra of AgNPs are closely similar regardless of whether they were synthesized through irradiated AgClO_4 or AgNO_3 (Figure 5.7c). These experiments support ammonia as the driving force behind full reduction of $\text{Ag}^+ \rightarrow \text{AgNPs}$, and reinforce the negligible role played by the nitrate group of AgNO_3 in hindering product-formation in the absence of ammonia.

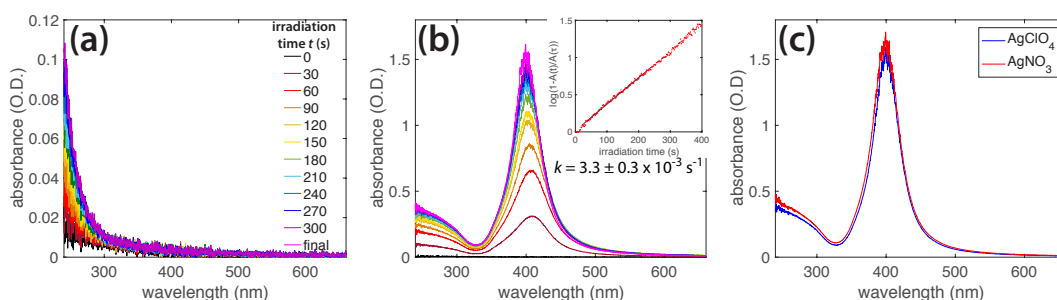


FIGURE 5.7: (a) Absorption spectra of AgClO_4 in water irradiated for 600 s, showing no AgNP formation in the absence of ammonia. (b) Absorbance peak of AgNPs from AgClO_4 (0.1 mM) in NH_3 (1 mM) as it grows during irradiation. (c) Absorbance spectra of AgNPs formed from irradiating AgClO_4 (red) and AgNO_3 (blue) in 1 mM NH_3 .

The similarity in formation rates and spectral properties among both 1 mM ammonia Ag^+ precursor solutions suggests that the counterions play no major role. Instead, reduction is controlled by the reducing species produced from water and NH_3 photolysis in OB plasma. Because of the high water concentration (55 M) compared to low (1 mM) NH_3 , the likeliest reducing species is the hydrated electron, which can be formed up to decimolar concentrations in OB plasma [96]. The dependence of the experimentally observed Ag^+ reduction kinetics on NH_3 concentration is counterintuitive, as reduction kinetics are fast in low NH_3 concentrations, and slow as NH_3 molarity is increased (Figure 5.1).

At NH_3 concentrations below 1 mM, solution pH (5.71–8.42, Figure 5.1c and Table D.1) is below the 9.26 pK_a of NH_4^+ —too low to support Ag^+ and ammonia complexation, which would allow $\text{Ag}(\text{NH}_3)_2^+$ formation [149]. The faster reduction kinetics may therefore be attributed to the high reduction potential of free Ag^+ compared to the complexed $\text{Ag}(\text{NH}_3)_2^+$ [145, 149]. These conditions cause rapid formation of amorphous, plate-like particles as seen at 0.25 mM in Figures 5.5a and D.3. At 1 mM NH_3 , the solution pH is

raised to 9.47, where only a small amount of NH_4^+ is present, and most Ag^+ is in the $\text{Ag}(\text{NH}_3)_2^+$ complex. This complexation, because of its lower reduction potential, slows the reduction kinetics enough to produce more uniform spherical AgNPs like in Figures 5.5b and D.4. As NH_3 concentration increases further, a competing reaction mechanism can occur where excess NH_3 starts to form significant amounts of ONOO^- . The consequential decrease in the Ag^+ reduction rate can be explained by back-oxidation of Ag^0 because ONOO^- also acts as a strong oxidant [151, 173]. This slow reduction causes the formation of large, agglomerated AgNPs (Figure 5.5c and D.5), and no AgNP colloids are formed at all at NH_3 concentrations above 20 mM. The absence of AgNP-formation at high NH_3 concentrations is consistent with increased ONOO^- production during irradiation—enough ONOO^- is analogous to the original H_2O_2 problem—and its decay is accelerated post-irradiation in the 100 mM ammonia AgNO_3 solutions (Figure D.2b,c). Collectively, these results indicate that for optimal Ag^+ reduction, it is necessary to find a concentration of ammonia high enough to react with $\text{OH}\cdot$ allowing formation of the $\text{Ag}(\text{NH}_3)_2^+$ complex, but low enough to avoid excess peroxyxynitrite production. This concentration is ~ 1 mM NH_3 .

5.1.4 Summary

Having confirmed that it is possible and even practical to synthesize colloidal AgNPs using ultrafast laser-assisted methods by avoiding Ag back-oxidation with radical scavengers; the next project adapts this chemical modification to KAuCl_4 solutions. By adding $\text{OH}\cdot$ scavengers to gold precursor solutions, it is expected that the rate of *specifically* k_2 can be slowed, therefore producing smaller particles. An optimal concentration of ammonia (1 mM) added to the precursor solution produced AgNPs with 12.7 ± 4.9 nm diameter, but higher or lower ammonia concentrations resulted in poor dispersity if any AgNPs were formed at all.

5.2 Gold

As hydroxyl-radical scavengers decrease the concentration of hydrogen peroxide formed in irradiated, aqueous solutions, it follows that they might selectively slow autocatalytic particle growth, k_2 . If k_2 can be slowed sufficiently, gold particles would be allowed to reach a size where they are stable enough to avoid agglomerating, but excess growth might be prevented. Provided that k_1 is unhindered and many nuclei are able to form, a selectively slower k_2 might enable AuNP tailoring to optimize catalytic applications.

5.2.1 Acetate and Isopropyl Alcohol

It is already understood that AuNP formation follows the [two-step Finke-Watzky rate law](#). Nucleation relies on e_{aq}^- , and autocatalytic growth relies on H_2O_2 produced by $\text{OH}\cdot$ recombination. Details about these mechanisms are in Chapter 3.

Sodium acetate exists as a hydroxyl radical scavenger in biological contexts [174]. There was precedent that liquid ammonia might facilitate the photoreduction-synthesis, and the effects of AuNP formation in liquid ammonia solutions is a project currently underway in Dr. Tibbetts lab. For this study, we centered our attention on IPA and sodium acetate as $\text{OH}\cdot$ scavengers.

In this experiment, as in Chapter 4, gold concentration remained static at 0.1 mM. All solutions were irradiated with high-NA focusing-geometry and $I = 2.5 \times 10^{16}$ pulses. Precursor solutions were kept within a pH range of 6.7 ± 0.2 . All working solutions contained 0.1 mM KAuCl_4 , but the concentration of radical scavenger ranged between 0.1 and 100 mM, so KOH was added accordingly to correct the pH. The procedure is elaborated upon in Section 2.1 in Chapter 2. Irradiation times varied by scavenger concentration.

5.2.2 Results

Reduction Kinetics

As before, reaction kinetics for these experiments were computed by monitoring growth of the absorbance peak at $\lambda = 450$ nm. This peak is proportional to the Au^0 concentration and is minimally dependent on AuNP size, avoiding interference from KAuCl_4 absorption [124]. Complete conversion of $[\text{AuCl}_4]^-$ to AuNPs is considered achieved when the 450 nm absorbance peak stops growing. The corresponding absorbance value is used to normalize the fractional AuNP concentration at earlier irradiation times. Figure 5.8a,c shows the representative plots of fractional AuNP concentration versus irradiation time for selected concentrations of IPA and acetate, with fits to an integrated form of the Finke-Watzky rate law (eq 3.18) [123]

$$[A_t] = [A_0] - \frac{\frac{k_1}{k_2} + [A_0]}{1 + \frac{k_1}{k_2[A_0]} e^{(k_1 + k_2[A_0])t}} \quad (5.3)$$

with $[A_0]$ normalized to 1.0.

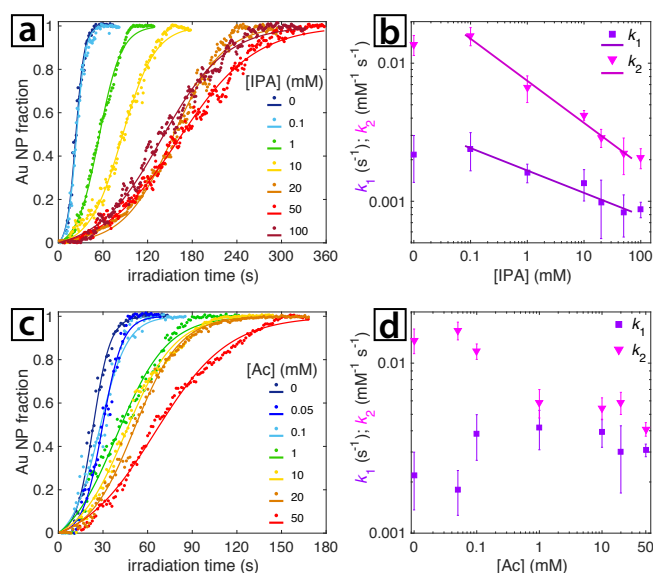


FIGURE 5.8: Representative plots of fractional growth of AuNPs versus irradiation time (circles \circ), with fits to eq 3.19 (solid lines), and obtained k_1 (purple \square) and k_2 (magenta ∇) for different concentrations of (a-b) IPA, (c-d) acetate. Corresponding scavenger concentrations given in the legend.

Rate constants k_1 and k_2 , extracted from fitting to eq 5.3, are shown in Figure 5.8b,d as functions of scavenger concentration (full tabulated values are given in Appendix E, Tables E.9 and E.10). When IPA is used as the scavenger (Figure 5.8b), both k_1 and k_2 decay with increasing IPA concentration at rates $k_1 \sim [\text{IPA}]^{-0.16}$ and $k_2 \sim [\text{IPA}]^{-0.31}$ over the range of 0.1 to 50 mM. Acetate behaves differently, k_1 rises but k_2 falls over the increasing acetate concentration range of 0.05 to 1 mM. For both scavengers, the decrease of k_2 is consistent with a decreasing concentration of H_2O_2 , as will be discussed in Section 5.2.3.

AuNP Products

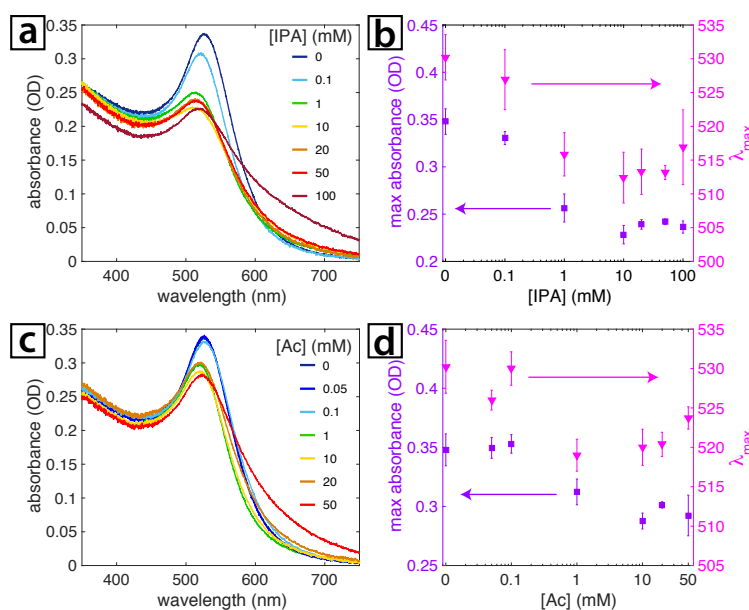


FIGURE 5.9: UV-vis spectra of final AuNP products synthesized with different scavenger concentrations, and the SPR absorbances and wavelengths for each spectrum as a function of scavenger concentration; for IPA (a–b), and acetate (c–d).

UV-vis spectra of AuNPs synthesized in different radical scavenger concentrations (Figure 5.9a,c) show that the localized SPR peak around 520 nm decreases as the scavenger concentration increases, for both IPA and acetate. The SPR absorbance reaches a minimum at 10 mM IPA (Figure 5.9b, purple axis)—indicating that the smallest AuNPs are produced at this concentration [124]—and increases again as scavenger concentration continues to increase to 20 and then to 50 mM. Exceedingly high IPA concentrations (~ 100 mM), cause the AuNPs to agglomerate, which is visualized through the SPR peak redshifting and broadening in the UV-vis spectra. Additional TEMs that further illustrate AuNP agglomeration at high IPA concentration are in Figure E.1, and AuNPs formed at the optimal, 10 mM IPA concentration are in Figure E.2 in Appendix E. A similar trend is observed for acetate (Figure 5.9d, purple axis), where 10 mM was also the optimal concentration. At increased acetate concentrations (20 mM) the SPR absorption increases, and at concentrations of 50 mM and higher, the NPs agglomerate. The average SPR wavelength (Figure 5.9b,d, magenta axis) follows the same trend for both IPA and acetate. The SPR peak blueshifts from 530 to 512 nm as more scavenger is added, meaning the products are likely smaller AuNPs [124]. It is evident from the comparative degree of blueshift in

the two sample sets that acetate does not have as strong an effect on particle size as IPA does.

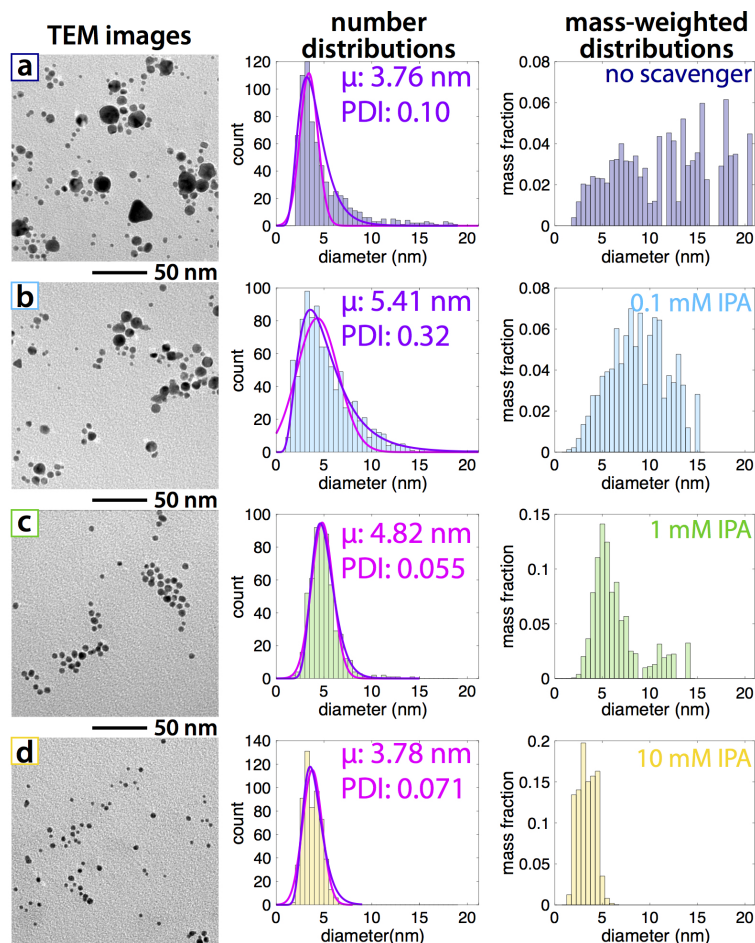


FIGURE 5.10: Representative TEM images and corresponding size distributions and mass-weighted distributions of AuNPs synthesized using (a) no IPA (b) 0.1 mM (c) 1 mM and (d) 10 mM IPA

TEM analysis confirms the expected trends in AuNP sizes predicted from the UV-vis spectra reported in Figure 5.9. Figures 5.10 and 5.11 show representative TEM images with histograms representing AuNP product sizes, each compiled using data from at least 500 particles examined with ImageJ software. The size distributions in the AuNPs were fit to both Gaussian and log-normal functions (solid magenta and purple curves, respectively) to determine the mean particle size (μ) and standard deviation (σ). For each distribution and fit function, the *polydispersity index* (PDI) was computed as $\frac{\sigma^2}{\mu^2}$ (Appendix E, Tables E.1–E.6). The PDI values reported in Figures 5.10 and 5.11 are taken from the function with the better fit to the experimental distribution (indicated in purple for log-normal and magenta for Gaussian). The AuNPs produced with 1 mM IPA (PDI 0.055), 10 mM IPA (PDI 0.071) and 10 mM acetate (PDI 0.069) have remarkably narrow Gaussian size distributions and are homogeneously spherical, as confirmed in TEM images. The Gaussian size distributions and lack of large particles distinguish our AuNPs from those reported from PLAL, which have small quantities of large NPs with log-normal distributions [56]. In general, using acetate as a scavenger produced larger, more dispersed (as expressed in the higher PDI) AuNPs than those from IPA. Although most nanoparticles were small

(<10 nm) even in the absence of scavengers, the population of *sub-5 nm* is considerably increased when IPA is added.

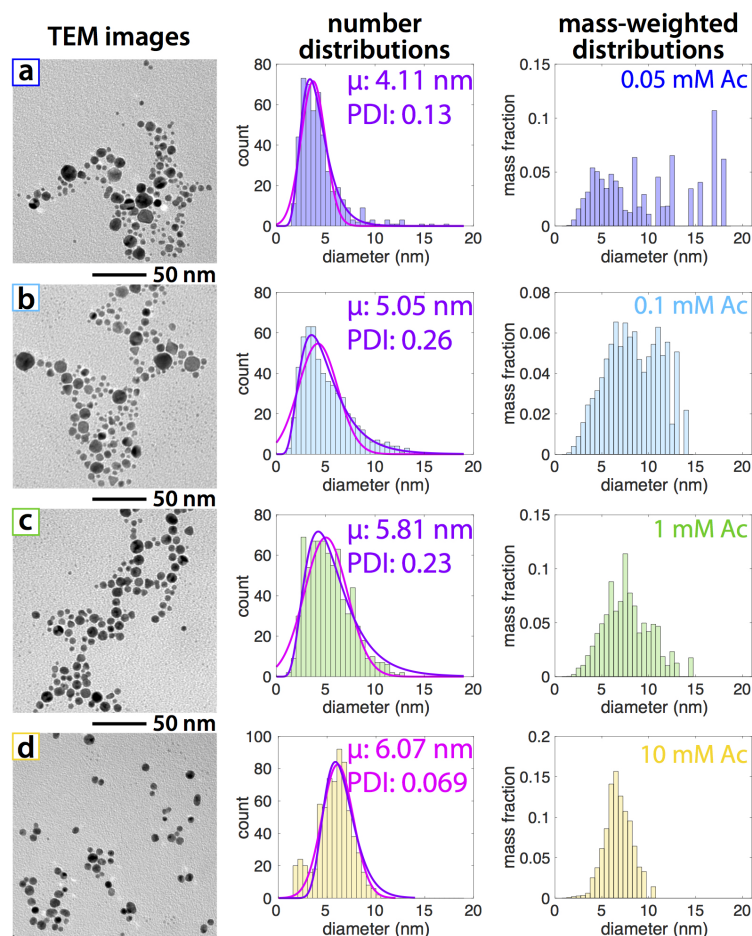


FIGURE 5.11: Representative TEM images and corresponding size distributions and mass-weighted distributions of AuNPs synthesized using (a) 0.05 mM (b) 0.1 mM (c) 1 mM and (d) 10 mM acetate.

Selected samples of AuNPs were characterized using XPS to ascertain the oxidation states of gold. Au 4f XPS spectra of samples synthesized with no scavenger, 10 mM IPA, and 10 mM acetate are shown in Figure 5.12. The experimental data with deconvoluted peak-binding energies, their corresponding proposed species [175–177], and relative atomic percentages, are on each plot. The AuNPs synthesized with 10 mM IPA contain a significantly higher percentage of low-coordinated Au⁰ atoms (binding energy near 83 eV) than both the scavenger-free and the 10 mM acetate samples. Simultaneously, the deconvoluted peaks near 84 eV corresponding to bulk Au⁰ are more dominant in the scavenger-free and 10 mM acetate samples (47.4% and 49.4%, respectively) than in the 10 mM IPA sample (37.3%). Finally, the peak near 86 eV, which corresponds to Au⁺¹, shows lower values for the scavenger-synthesized AuNPs (4.6% for IPA, and 6.5% for acetate) than for the scavenger-free sample (9%). Additional details are provided in Appendix E, Tables E.7-E.8.

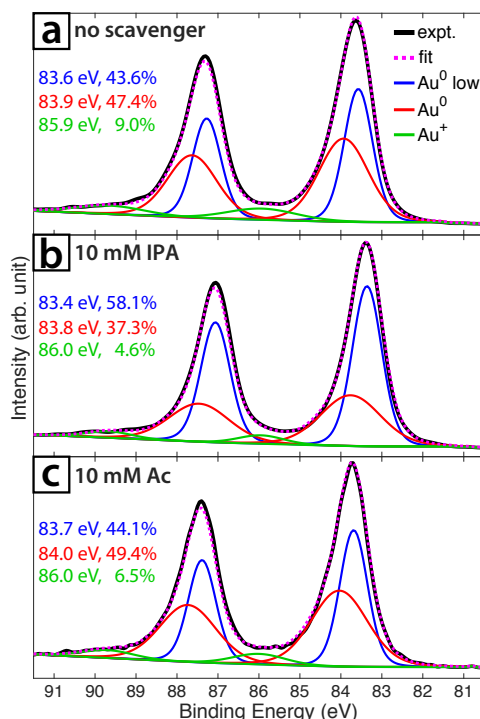


FIGURE 5.12: XPS spectra for Au 4f peak of AuNPs synthesized with (a), no scavenger (b), 10 mM IPA (c) 10 mM acetate with deconvoluted peaks for low-coordinated Au⁰ (blue), Au⁰ (red), and Au⁺¹ (green).

Catalysis

Figure 5.13 summarizes our results for AuNP catalytic activity using the model PNP reduction reaction [178–180]. The apparent rate constant (k_{app}) values presented in Figure 5.13a represent the averaged pseudo-first-order rate constant, and were obtained by extracting the slope of the line generated by plotting the natural logarithm of nitrophenolate absorbance PNP_t at time t divided by the initial absorbance PNP_0 ($\ln(PNP_t/PNP_0)$) [87]. The k_{app} values decrease by <10% for the no scavenger and IPA samples and by <20% for the acetate samples as the AuNPs aged over 3–6 months, indicating good AuNP stability even in the absence of capping agents. The reasons for the loss of catalytic activity in acetate samples will be discussed in Section 5.2.3. Figure 5.13b shows k_{Au} , which is the rate constant normalized to the moles of Au added to the reaction, and quantifies the efficiency of Au atoms present. AuNPs synthesized with 10 mM of scavenger are the most efficient catalysts, with IPA producing the best value. Lastly, Figure 5.13c illustrates the specific surface area (SSA)-normalized rate constant k_1 . This rate constant is indicative of the available surface sites driving the PNP reaction [87, 178–180]. The larger error bars come from the standard deviations (σ) derived from the size distribution analysis of TEM images. The k_1 values for all scavenger concentrations are within the error range of the AuNPs synthesized without scavengers. This SSA stagnancy indicates that adding scavengers does not passivate the AuNPs surface. Appendix E Tables E.12 and E.13 display the tabulated values for size, SSA, and catalytic rate constants of AuNPs synthesized in this work.

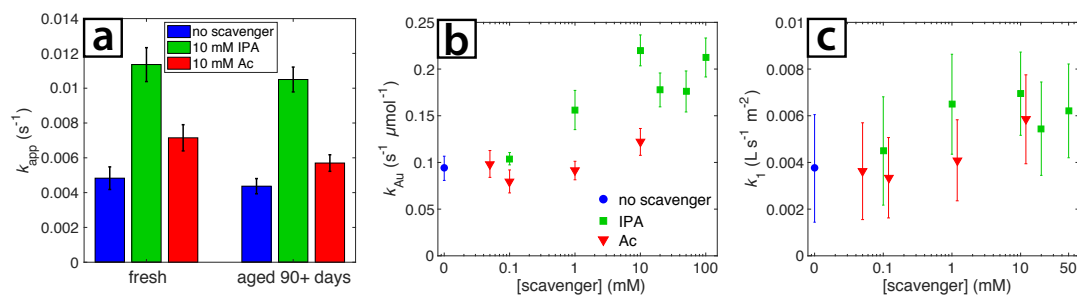


FIGURE 5.13: (a) Apparent rate constant k_{app} values of NPs within 0 to 2 days after synthesis (fresh) and more than 90 days after synthesis (aged 90 days). (b) Dependence of average Au normalized rate constant k_{Au} , and (c) SSA-normalized rate constant k_1 on scavenger concentration for IPA (green) and acetate (red).

5.2.3 Discussion

Hydrogen Peroxide

The reactions governing plasma formation in femtosecond-laser irradiated water (eqs 3.1 through 3.6 in Section 3.1) have been established by many investigations [22, 24, 25, 62, 63, 66, 69, 72, 73, 91–97]. Of these photolytic reactions, we sought to selectively inhibit reaction 3.5, in which hydroxyl radicals recombine to form H₂O₂ [92–97]. The Finke-Watzky autocatalytic growth rate constant, k_2 , is dependent on the concentration of H₂O₂; therefore its decrease with increasing OH· scavenger concentration (Figure 5.8) suggests that less H₂O₂ is produced. The established correlation between OH· and H₂O₂ production in aqueous solutions irradiated with femtosecond laser pulses [181] indicates that we can quantify scavenging efficiency by measuring the H₂O₂ yield in irradiated scavenger solutions devoid of KAuCl₄.

Figure 5.14 shows the fractional yields of H₂O₂ generated at different scavenger concentrations, relative to that generated in water—‘1’ indicating a H₂O₂ concentration of 1.21 ± 0.12 mM. The inset of Figure 5.14 depicts representative UV-vis spectra showing increased absorption of pertitanic acid at 407 nm, when no scavenger is present. Quantified peroxide yields are tabulated in Appendix E, Table E.14. In summary, hydrogen peroxide formation is inhibited as the concentration of scavenger in solution increases. Additionally, IPA appears to be the more efficient OH· scavenger, as a lower concentration is required to achieve the same level of suppression as acetate. These findings agree with the reported reaction rate of IPA with OH· ($k = 2.1 \times 10^9$ M⁻¹s⁻¹) compared to the reaction rate with acetate ($k = 7.0 \times 10^7$ M⁻¹s⁻¹) [182].

Scavenging Mechanism of Acetate

Acetate reacts with hydroxyl radicals exclusively by H-atom abstraction [182, 183], as seen in Scheme 5.1. Al-Sheikhly et al. [183] elaborate that it is also possible for the carboxymethyl radical produced in Scheme 5.1 to react with O₂ and form the acetic acid peroxy radical. At sufficiently high concentrations, this species can dimerize into an unstable tetroxide of acetic acid, which can subsequently decay into glyoxylate and H₂O₂. Details of this mechanism can be found in ref [183], eqs 16–18. This reported acetate

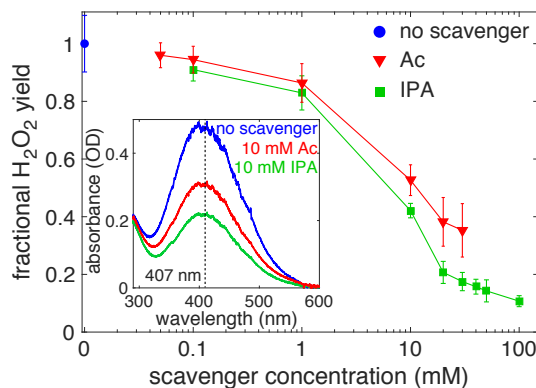
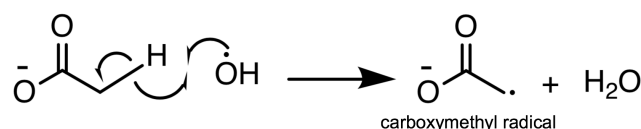


FIGURE 5.14: Absorption spectra of $\text{TiO}_2/\text{H}_2\text{O}_2$ in both water and 10 mM $\text{OH}\cdot$ scavenger solutions (a); formation of H_2O_2 generated in increasingly concentrated scavenger solutions, displayed as fractions of the amount formed in pure water (b). Solutions were irradiated for 180 s using the experimental conditions described in 2.2.

reaction pathway, producing H_2O_2 , is consistent with our findings and may help explain why acetate is less effective at inhibiting H_2O_2 formation than IPA (Figure 5.14).

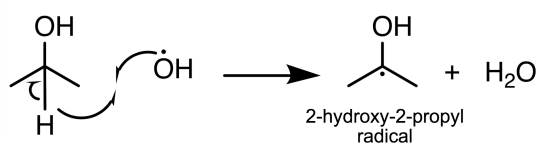


SCHEME 5.1: Radical-scavenging mechanism of acetate.

Despite its comparative effectiveness with hindering H_2O_2 formation, acetate could theoretically yield smaller nanoparticles because higher concentrations increase k_1 (Figure 5.8d), triggering gold nuclei generation. Meanwhile, the lower k_2 values are expected to inhibit the growth of existing nuclei and AuNPs. However, the size-distributions of AuNPs prepared with acetate are consistently larger than those for IPA (Figure 5.11). This incongruity could stem from the ionic nature of sodium acetate. It was shown by Sylvestre et al. [51] that at salt concentrations greater than 10 mM, AuNPs show signs of agglomeration and begin to precipitate within a few hours of synthesis. We observed very different behavior in our colloidal products prepared using 50 mM acetate compared to those prepared using 20 mM acetate and below. In these high-concentration cases, the product solutions were gray-tinted blue, a color usually associated with agglomeration [51], and they formed precipitate within minutes after irradiation. To assess the contribution of salt concentration to this agglomeration behavior observable with high concentrations of acetate, experiments were performed in which sodium acetate was replaced with sodium chloride (KCl). Appendix E Figure E.3 shows representative TEM images and corresponding size distributions of AuNPs synthesized with 0.1 and 1 mM KCl. It can be observed that there is no improvement in size dispersity. At concentrations of KCl exceeding 10 mM, AuNPs agglomerated and precipitated out of solution. The $[\text{AuCl}_4]^-$ conversion kinetics in the presence of KCl (Appendix E, Table E.11) are no different from the kinetics without additives. From these results, we conclude that the efficiency of acetate as a size-control agent is limited by both its lower $\text{OH}\cdot$ -scavenging ability; and its ionic structure, which promotes AuNP aggregation. Moreover, this induced aggregation likely contributes to the greater loss of catalytic activity for aged AuNPs synthesized with acetate as compared to the no scavenger and IPA samples (Figure 5.13a).

Scavenging Mechanism of Isopropyl Alcohol

Previous investigations into scavenging mechanisms for IPA indicate that 2-hydroxy-2-propyl (ketyl) radicals can be formed via intermolecular H-abstraction by $\text{OH}\cdot$ in solution—see Scheme 5.2 [72, 184, 185]. These sources also report that IPA acts as a reducing agent, aiding in AuNP formation through the ketyl radicals initiating a one-electron reduction of the $[\text{AuCl}_4]^-$ complex. The addition of another reducing species should increase the quantity of gold nuclei, which should reflect as an increased k_1 . However, k_1 actually *decreases* with increased IPA concentration (Figure 5.8b), which indicates that IPA does *not* act as a reducing agent under our experimental conditions. This result suggests that the hydrated electrons produced in the plasma are the more dominant reducing agent, which is consistent with their reported diffusion-limited reaction rate with $[\text{AuCl}_4]^-$ ($6.1 \times 10^{10} \text{ M}^{-1}\text{s}^{-1}$) [125]. Moreover, the decreased k_1 reveals that IPA may be scavenging a portion of the hydrated electrons, in accordance with the reported reaction between alcohols and solvated electrons to form deprotonated alkoxides and hydrogen atoms [186].



SCHEME 5.2: Radical-scavenging mechanism of IPA.

To assess the scope of IPA scavenging activity, we repeated the IPA concentration study while holding the solution pH fixed at 5.3 ± 0.2 , the value used in our Chapter 4, for easy comparison to the pH of 6.7 ± 0.2 used for the experiments reported here, in Section 5.2.2. These experiments showed that the trends of decreased AuNP sizes and k_2 seen in Figures 5.9, 5.10, and 5.8, both hold at lower solution pH (Appendix E Figure E.4). UV-vis spectra of AuNP products formed at higher concentrations of IPA exhibit broader peaks with lower SPR absorbances, and blueshift. The formation kinetics at high IPA concentrations are slower, with lower k_2 values. All of these indicators parallel those observed in the experiments at pH 6.7, implying smaller nanoparticles with narrow distributions. These results indicate that IPA is an effective scavenger regardless of pH, and suggests that the addition of IPA to control nanoparticle sizes in photochemical reduction experiments can be used over a range of pH values.

5.2.4 Summary

Overall, $\text{OH}\cdot$ scavengers are an effective tool for reducing particle diameters; however, as was also seen with silver, it is not a linear relationship in which more scavenger yields smaller particles. We found it necessary to determine an optimal concentration, beyond which products become unpredictable. Although at first glance, mean particle sizes seemed comparable whether we used a scavenger (3.78 nm with a PDI of 0.071) or not (3.76 nm with a PDI of 0.10), once we were able to look at a mass-weighted distribution of our colloidal products it was evident how much of a difference the presence of scavenger made—products synthesized in scavenger solutions were much more clustered toward a small range of sizes, where the particles that grew without a scavenger present covered a very wide mass range.

Chapter 6

Conclusions

Photoreduction of Au^{3+} follows a two-step mechanism in which k_1 , which describes the formation of gold nuclei, is reliant on free electron density; and k_2 , the autocatalytic growth of nuclei in metal-ion solution, relies on H_2O_2 generated from $\text{OH}\cdot$ recombination. Furthermore, the one-step mechanism of Ag^+ photoreduction into AgNPs is reversed by the presence of H_2O_2 . To facilitate laser-assisted metallic nanoparticle synthesis, we sought to further elucidate these mechanisms and determine product morphology-tuning strategies. First, in Chapter 4, we examined the effects of the laser beam itself. Then, in Chapter 5, we addressed the issue of Ag^0 back-oxidation by adding a $\text{OH}\cdot$ radical scavenger to our solution. Finally, in Chapter 6, we mimicked this second study with the two-step photoreduction mechanism of gold, to see how it affected product outcomes and colloidal stability.

	E_p (μJ)	τ_p (fs)	mean diameter (nm)	scavenger
Au	2400	30	3.5 ± 1.9	
Au	2400	1500	6.3 ± 2.4	
Au	150	30	6.4 ± 5.6	
Au	150	1500	4.4 ± 4.0	
Ag	1000	30	12.7 ± 4.9	1 mM NH_3
Au	1000	30	3.76 ± 1.19	
Au	1000	30	3.78 ± 1.01	10 mM IPA
Au	1000	30	6.07 ± 1.59	10 mM acetate

TABLE 6.1: Summary of MNP products.

Table 6.1 summarizes the trial conditions of each experiment and the average outcome of resultant nanoparticles. To convert PDI to standard deviation, I took the square root of the product of the mean diameter squared and PDI.

6.0.1 Pulse-Settings Experiments

The experiments in Chapter 4 first quantified the roles played by free electrons and H_2O_2 -formation in the photochemical reduction of Au^{3+} to AuNPs with femtosecond laser pulses. OB plasma volume grew with peak irradiance as $V \sim I^{1.5}$, which matched the growth of k_1 with peak irradiance, indicating that free electron formation from optical breakdown of water is directly proportional to the rate that gold atoms cluster into nuclei under our experimental conditions. By quantifying the formation rate of H_2O_2 as a function of pulse energy and pulse duration, we saw that the H_2O_2 formation rate was directly proportional to the irradiance at each pulse duration ($\text{H}_2\text{O}_2 \sim I$). The second-order

rate constant, k_2 , depended on peak irradiance through the relationship $k_2 \sim I^{0.5}$, and follows the same relationship of $k_2 \sim \text{H}_2\text{O}_2^{0.5}$ at all pulse durations. These results determined quantitative relationships between the Au^{3+} reduction rate and the two chemical species that have been proposed but not confirmed as the dominant reducing agents in femtosecond laser-assisted Au^{3+} reduction to AuNPs [22, 24, 25, 63–66, 70, 72, 73].

From our product characterizations, we found a stronger relationship between AuNP dimensions and pulse energy than with pulse duration. As pulse energy decreased, any initial, small AuNPs ($\sim 2 - 3$ nm) were found to agglomerate into larger $\sim 10 - 20$ nm particles, which had a dramatic effect on sample dispersity. However, the average AuNP diameter only doubled when pulse duration was increased from 750 fs to 1500 fs. These trends likely arise from the stronger dependence of the OB plasma volume on the peak irradiance, compared to the H_2O_2 formation, which does not rely as strongly on irradiance. At low pulse energy, the H_2O_2 concentration in OB plasma will be higher relative to the electron density, favoring formation of fewer Au nuclei and increasing sizes of existing AuNPs through autocatalytic growth and agglomeration. Understanding how the laser pulse parameters influence the chemical composition of the OB plasma may enable improved tuning of metal NP sizes and properties. For instance, these findings may facilitate optimization of NP synthesis conditions in other metal systems where the production of H_2O_2 in the OB plasma may play a more detrimental role (notably, oxidation of AgNPs to Ag^+ in the presence of H_2O_2).

6.0.2 Solution Experiments: Scavengers

Silver

The experiment in Chapter 5.1 investigated the radical-mediated chemistry induced by a femtosecond-laser plasma in aqueous solution. Adding liquid ammonia decreased the amount of H_2O_2 produced during water photolysis, and formed a species that was determined to be peroxyxynitrite, ONOO^- . The addition of NH_3 to aqueous solution was necessary to allow Ag^+ ions to reduce to form AgNPs, and 1 mM NH_3 was determined to be the optimal concentration for making spherical AgNPs with mean diameters of 12.7 ± 4.9 nm. The extreme sensitivity of Ag^+ reduction kinetics, and the AgNP morphology, demonstrates that understanding the reactions of the radical species produced in the laser plasma is crucial for nanoparticle synthesis using femtosecond laser irradiation methods. We anticipate that controlling the amounts of radical species in femtosecond-laser plasma by varying the amount of NH_3 added to aqueous solutions will help to better formation techniques for other metal NPs or alloyed metal NPs in the future.

Gold

Chapter 5.2 explored kinetic control over AuNPs synthesized by laser-induced photochemical reduction of aqueous Au^{3+} . Control was achieved through the addition of hydroxyl radical scavengers IPA and, to a less successful degree, sodium acetate. Size distribution analysis, TEM imaging, and XPS spectra agreed with the trends predicted by the reduction kinetics and the UV-vis spectra of final AuNP products, demonstrating that the addition of IPA effectively slowed the reaction rate and limited AuNP growth. The optimal concentration of 10 mM IPA resulted in an average particle diameter of 3.78 ± 1.01 nm. The catalytic activity of AuNPs synthesized with added IPA retain their catalytic activity 3-6 months after synthesis, showing that these colloidal solutions remain stable for months.

These results support a significant improvement in controlling the size-distributions of uncapped AuNPs synthesized by laser-induced photochemical reduction over our previous studies [63, 69], and the optimal conditions produce a size distribution comparable to those recently reported with a two-step PLAL-fragmentation procedure [58]. Finally, the small AuNP sizes and high fraction of low-coordinated Au atoms are expected to make these uncapped AuNPs suitable for catalytic applications such as CO oxidation.

6.1 Implications and Future Studies

The work performed for this thesis confirms that LPR is a tenable MNP synthesis route, offering avenues to NP-tuning and producing stable colloids capable of real-world applications. We were able to find ways to make this method work with silver, a metal whose chemistry was not compatible with the key reactive species produced during irradiation. I have also personally worked on projects involving other metals—like palladium, which has several catalytic and CO oxidation applications [187, 188]—and I have explored Au-Ag alloy NP LPR synthesis. Other potentially useful metals being examined in the lab include: platinum, which has been used in cancer treatment, fuel cells, automotive catalytic conversion, petroleum refining, and hydrogen production [189]; titanium, with uses in photocatalysis and environmental pollutant-removal [190]; iron, which is both cheap and highly stable, it has the capacity for magnetic applications [191]; cerium, with applications in environmental filtration, fuel cells, and oxygen sensing [192]; copper, with an array of catalytic applications owing to its many accessible oxidation states, and antimicrobial properties which make it appealing for biomedical use [193–195]; aluminum¹, which is abundant and cheap, and has an NP plasmon tuning range that is much wider than those of gold and silver [196]; and zinc, which is extremely adaptable to photovoltaics [197]. In addition to these applications, almost all of these also have biomedical, detection, and other catalytic applications as well. In all cases, it will be necessary to yield cost-efficient, stable, and monodisperse colloids with predictable morphologies and tunable diameters. On the basis of our research so far, I think we have a lot to feel optimistic about, as each individual trial demands less than half a microgram of metal, and takes no more than a few minutes to complete.

¹ Aluminum was discovered in 1808 by Humphry Davy as he was examining a crystal compound used in industry called *alum*. He called the element ‘aluminium’ at first, before changing his mind to ‘aluminum’. The formal name of the element was adopted as ‘aluminium’ because chemists, at the time, felt we ought to adhere to a pattern, and it seemed like most elements were ending with the -ium suffix. Eventually, some institutions (such as the American Webster’s Dictionary) decided to revert back to ‘aluminum’—again, for no real reason.

Appendix A

Beam Parameters

A.1 Measurement of Pulse Duration (FROG)

The pulse duration was varied by displacing the grating in the compressor to induce a linear chirp across the laser spectrum. The pulse durations selected for this study were 30 fs (the shortest pulse, zero displacement), 200 fs (we used both positive and negative chirp), 750 fs (negative chirp), and 1500 fs (negative chirp). A home-built *Frequency Resolved Optical Gating* (FROG) setup was used to measure the spectrograms and the time-dependent electric fields were retrieved with an open-source MATLAB code [198], based on the retrieval algorithm in ref [199]. Representative spectrograms and retrieved temporal electric fields are shown in Figure A.1 for pulses with durations 30 fs, 200 fs (positive and negative chirp), 750 fs, and 1500 fs. Observed deviations from a Gaussian intensity profile in the chirped pulses arise from [self phase modulation](#) in the compressor, caused by the high-input pulse energy of 6.5 mJ. Retrieved fwhm durations for pulses with the (labeled) durations, generated over several different days, had the following

	30 fs	27 – 32 fs
	750 fs	738 – 768 fs
ranges:	200 fs	189 – 212 fs
	1500 fs	1428 – 1545 fs

A.2 Focusing Geometry

The size of the focused beam after the lens in Figure 3.6a was measured with a CCD camera (ThorLabs, Inc., pixel width 5.2 μm) mounted on a linear translation stage. Twenty images of the beam were recorded over a propagation distance of 0.5 mm at an interval of 0.025 mm. The beam spot in each image was fit to a Gaussian function in both the x and y directions using a MATLAB code, and the average waist at intensity $1/e^2$ of the maximum recorded. This value is plotted as a function of beam propagation distance in eq A.1. The data were fit to the Gaussian beam propagation function

$$w(z) = w_0 \sqrt{1 + \frac{(z - a)^2}{z_R^2}} \quad (\text{A.1})$$

to obtain the fitting parameters $w_0 = 0.0006159$, $z_R = 0.007768$, and $a = -0.001525$ (all in cm). The a parameter represents a trivial shift of the focus along the propagation axis, while the parameters w_0 and z_R represent the beam waist and Rayleigh range, respectively.

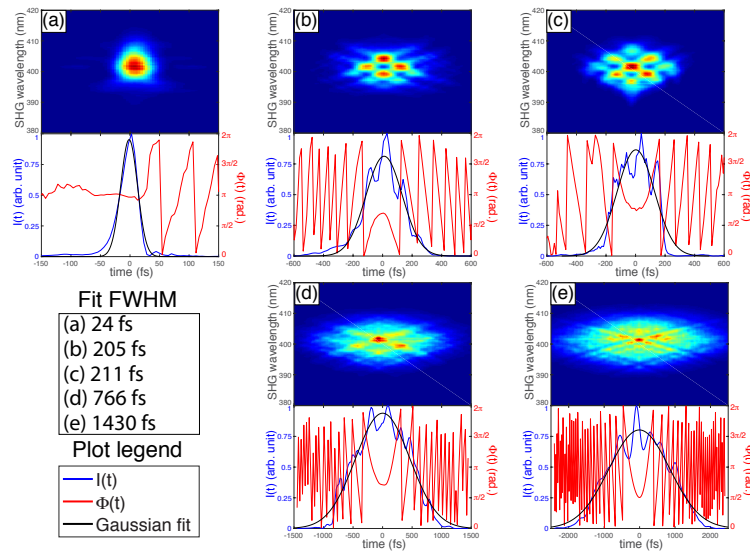


FIGURE A.1: Two-dimensional spectrograms recorded with Second Harmonic Generation (SHG)-FROG setup (top panels) and retrieved time-dependent electric fields (bottom panels).

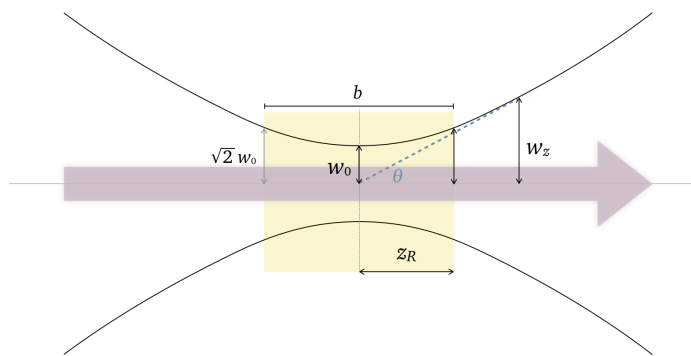


FIGURE A.2: In this diagram of a Gaussian beam, the focal point is at the center where the width is narrowest. The radius of this point is the beam waist w_0 . The Rayleigh range z_R is determined by the beam waist, where $z_R = \pi w_0^2 / \lambda$.

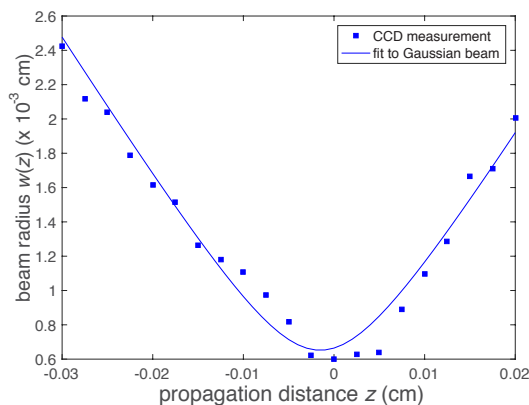


FIGURE A.3: Measured beam radius as a function of propagation distance (\square) and fit to eq A.1 (solid line). The beam propagation was in order of increasing z value.

This tight-focusing geometry resulted in no SCE in the quartz surface. Figure A.4 shows that the secondary bright spot (indicated by the blue arrows) near the focus for 30 fs, 2400 μJ pulses is a second focal point in the solvent before the main focus. This spot likely arises from some self-focusing of the beam in the quartz, but this first leads to SCE after propagating a short distance in the water.

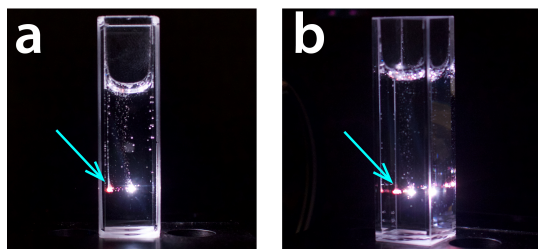


FIGURE A.4: Photographs of 30 fs, 2400 μJ pulses focused into a quartz cuvette: side view at 90° (a) and angled view from behind the focusing lens (b).

A.2.1 Electron Density Modeling

The theory of photoionization in dielectrics under strong field optical excitation was developed by Keldysh [98] and has been implemented in different ways in many different works [44, 46–48, 106, 107]. Here, we take the full Keldysh treatment of multiphoton and tunnel ionization (eqs 3.13 and 3.14); and in the regime where the Keldysh parameter $\gamma \sim 1$, we use a weighted average of the two expressions to ensure a smooth ionization rate over the full range of irradiances, as in ref [107]. Figure A.5 shows the ionization rate as a function of peak irradiance in the laser pulse using our full treatment (blue), as well as the constituent Keldysh multiphoton (red) and tunnel (yellow) expressions. For comparison, the Kennedy¹ approximation of the multiphoton ionization cross section $W = \sigma_5 I^5$ [47] is also shown (green).

¹The Kennedy approximation is a first-order computational model used to calculate intensity thresholds for laser-induced OB in condensed optical media.

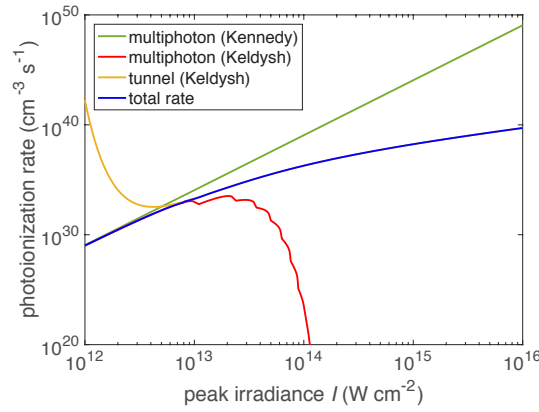


FIGURE A.5: Photoionization rate in water as a function of peak irradiance, calculated using Kennedy's multiphoton approximation (green), Keldysh treatment of multiphoton ionization (red), tunnel ionization (yellow), and the full treatment (blue) used in this work.

As discussed in Chapter 3, the peak electron density achieved as a function of z was calculated using a differential equation for electron density (eq 3.11) for each pulse energy and duration used in the experiments, shown in Figure A.6. The associated values of z_{crit} for each threshold determined at each pulse duration and energy. In each plot, the electron density threshold $\rho_e = 1.8 \times 10^{20} \text{ cm}^{-3}$ is denoted by a dashed line. The maximum electron density in the plots is capped at $\rho_e = 4 \times 10^{22} \text{ cm}^{-3}$ on the basis of the estimated ρ_e limits of optical breakdown plasmas in water from literature [107].

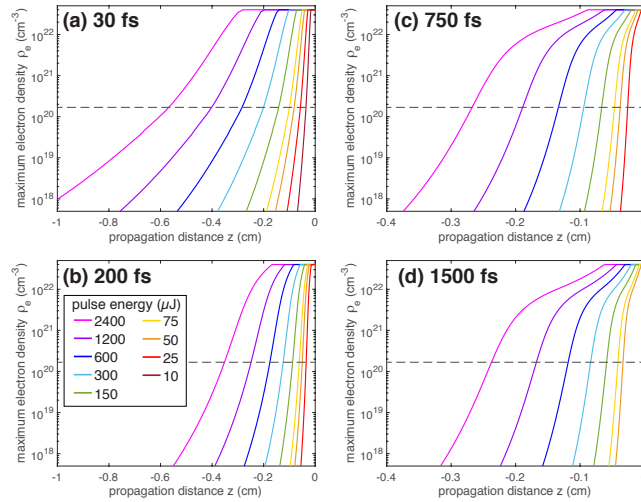


FIGURE A.6: Peak electron density as a function of propagation distance z for pulses with duration 30 fs (a), 200 fs (b), 750 fs (c), and 1500 fs (d), with pulse energies indicated by the colors in the legend of panel (b). In all panels, the dashed lines denote the electron density threshold of $\rho_e = 1.8 \times 10^{20} \text{ cm}^{-3}$.

Appendix B

Hydrogen Peroxide Quantification

B.1 Quantification of H_2O_2

Figure B.1 shows the UV-vis spectra of solutions containing approximately 3.3 mM titanium(IV) sulfate, with varying concentrations of previously standardized H_2O_2 . The absorbance at 407 nm for each solution was used to calibrate the amount of H_2O_2 produced upon laser irradiation of water at different E_p and τ_p . Synthesis of titanium(IV) sulfate and the experimental setup for quantifying H_2O_2 content in a solution is provided in Section 2.3.3 and was adapted from ref [88].

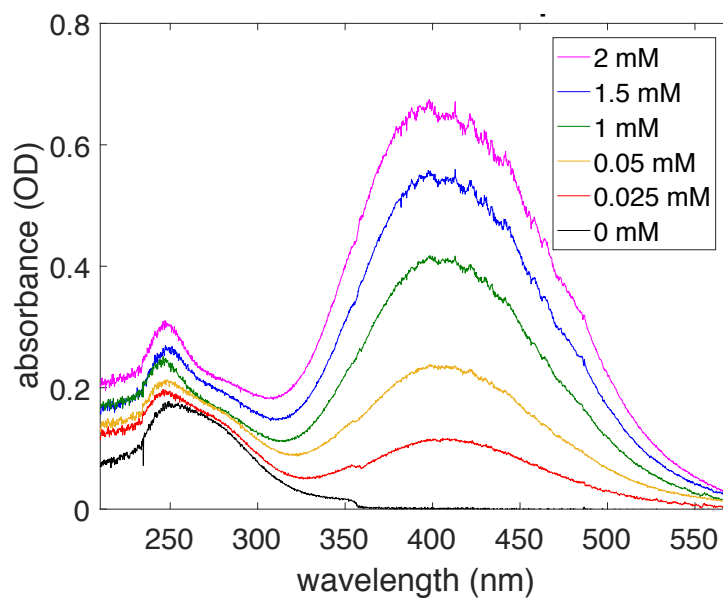


FIGURE B.1: UV-vis spectra of solutions containing standardized concentrations of H_2O_2 and the same amount of titanium sulfate added to the solution.

Figure B.2 shows the correlation between two methods of quantifying the formation rate of H_2O_2 , using different laser pulse energies and pulse durations. The parameters reported in Figure B.2 result from a linear fit of the data in log-log space, and agree with the amount of H_2O_2 quantified between the two methods (KMnO_4 titration vs. titanium(IV) sulfate addition, see Figure B.1). The pulse durations investigated are shown in the legend, and the pulse energies are 2400, 1200, 600, 300, and 150 μJ .

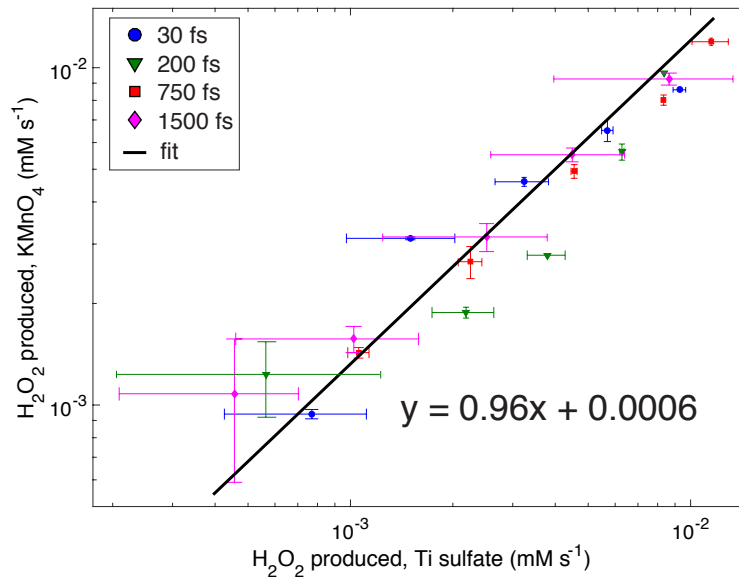


FIGURE B.2: Plot of H_2O_2 produced (mMs^{-1}) and quantified using two different quantification techniques, at different pulse energies and pulse durations (legend).

Appendix C

AuNP: Laser Parameters

C.1 Calculation of the Time-Dependent Concentration of $[\text{AuCl}_4]^-$

The following discussion summarizes the processing of the in situ UV-vis spectra used to determine the time-dependent concentration of $[\text{AuCl}_4]^-$. A more thorough discussion and justification of each processing step is provided in ref [63]. The absorbance of $[\text{AuCl}_4]^-$ is monitored at $\lambda = 280$ nm, with A_{280} defined as the average absorbance over the interval $279 \text{ nm} \leq \lambda \leq 281 \text{ nm}$. Because AuNPs also absorb across the UV range, their contribution to the measured absorbance at 280 nm at intermediate irradiation times when both $[\text{AuCl}_4]^-$ and AuNPs are present must be subtracted off to isolate the contribution from $[\text{AuCl}_4]^-$. The total absorbance at 280 nm is assumed to be the sum of the absorbance of $[\text{AuCl}_4]^-$ and AuNPs with no contribution from any other species;

$$A_{280} = A_{280}([\text{AuCl}_4]^-) + A_{280}(\text{AuNP}) \quad (\text{C.1})$$

To determine the contribution of AuNPs to the observed A_{280} in Section 4.2, the AuNP absorbance at 280 nm must be referenced to that at a wavelength where $[\text{AuCl}_4]^-$ does not absorb and where the AuNPs absorbance is not dependent on the specific SPR peak. Literature convention [124] puts the absorbance of AuNPs at 450 nm, A_{450} (average absorbance over $449 \text{ nm} \leq \lambda \leq 451 \text{ nm}$) is therefore used as our reference for AuNP. The absorbance ratio A_{280}/A_{450} is then taken for the [spectrum recorded](#) at the completion time $t = \tau$ when only AuNPs are present.

Because the ratio A_{280}/A_{450} for the absorbance of AuNPs is not expected to change significantly over the course of the reaction, we can use this ratio recorded at $t = \tau$ to determine the contribution of AuNPs to the measured $A_{280}(t)$ at any intermediate time t , leaving the contribution from $[\text{AuCl}_4]^-$,

$$A_{280}([\text{AuCl}_4]^- , t) = A_{280}(t) - A_{450}(t) \times \frac{A_{280}}{A_{450}} \Big|_{\tau} \quad (\text{C.2})$$

where the subscripts denote the irradiation times when each spectrum is measured.

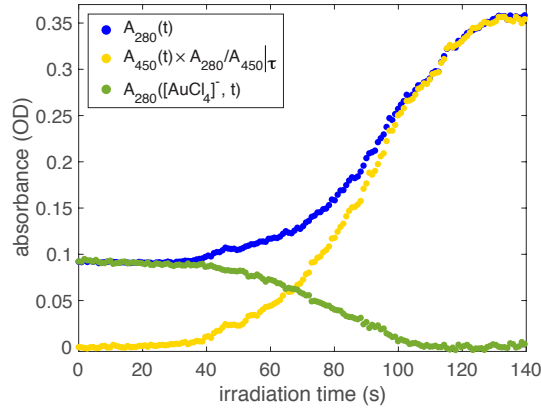


FIGURE C.1: Implementation of eq C.2 on the absorbance at 280 nm. The resulting quantity $A_{280}([AuCl_4]^-)$ represents absorbance only from $[AuCl_4]^-$.

The effect of implementing eq C.2 on the recorded value of A_{280} for an experiment conducted with $2400 \mu\text{J}$, 750 fs pulses in Figure C.1, which shows that $A_{280}([AuCl_4]^-)$ decreases to zero at $t = \tau$, indicating that this quantity effectively measures the concentration of $[AuCl_4]^-$. Finally, $A_{280}([AuCl_4]^-)$ is converted to the molar $[AuCl_4]^-$ concentration by normalizing to the initial concentration of 10^{-4} M at $t < 0$; before the laser is turned on. Figure C.2 shows the time-dependent $[AuCl_4]^-$ concentration with nonlinear

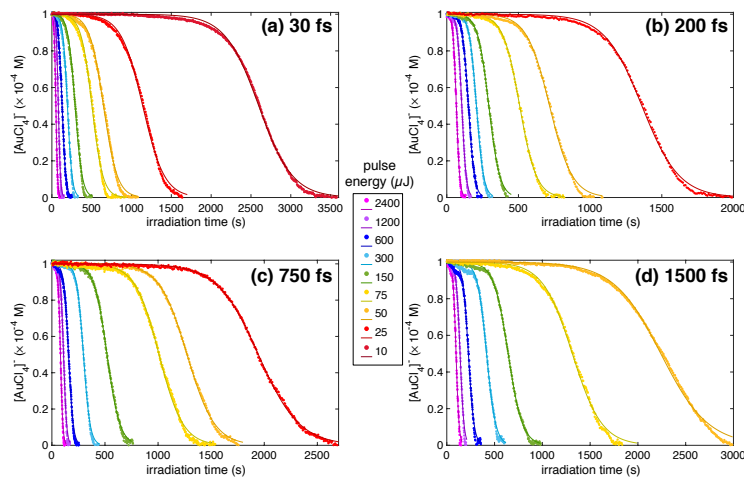


FIGURE C.2: Plots of $[AuCl_4]^-$ concentration versus irradiation time at each pulse energy for (a) 30 fs , (b) 200 fs (negative chirp), (c) 750 fs , and (d) 1500 fs pulses.

least-squares fits to eq 3.18 for representative experiments.

Figure C.3 show representative TEM images of the AuNPs formed under high laser energy (2400 μJ pulses) and low laser energy (150 μJ pulses). Panels (a,e) are AuNPs formed using 30 fs pulses; (b,f) used negative chirp 200 fs pulses; panels (c,g) used 750 fs pulses; and (d,h) are AuNPs formed using 1500 fs pulses.

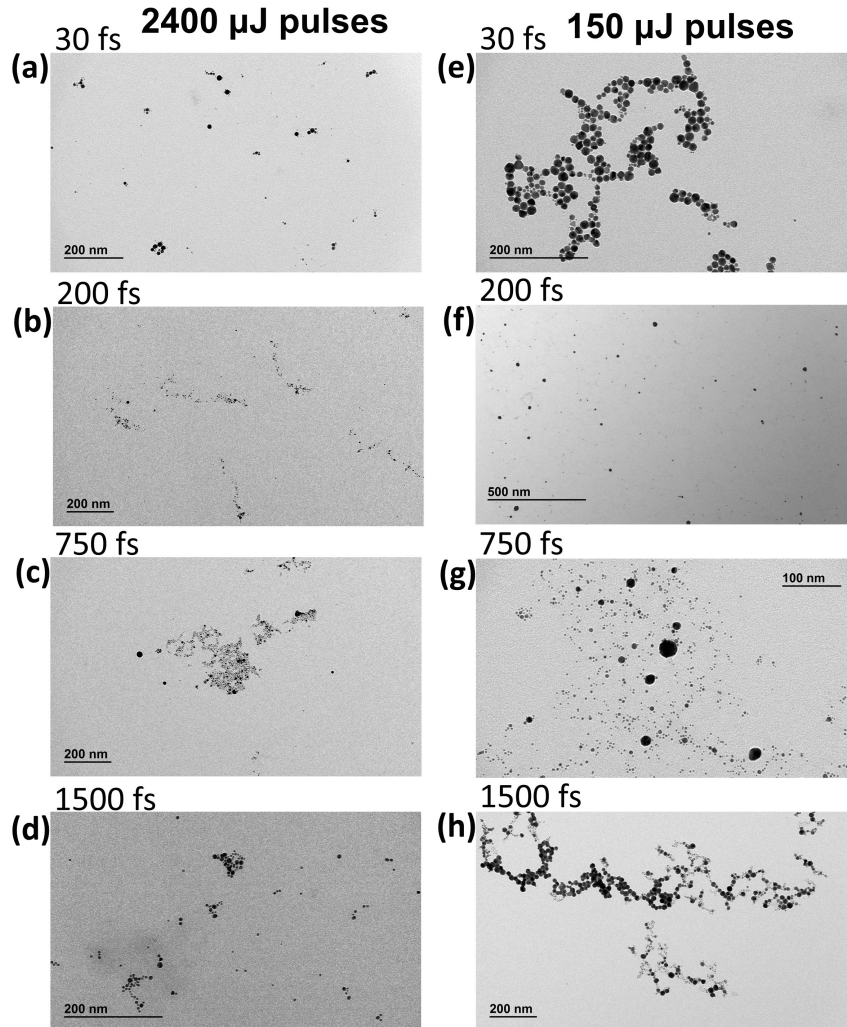


FIGURE C.3: Representative TEM images for AuNPs formed at two laser pulse energies, 2400 μJ (panels (a)–(d)) and 150 μJ (panels (e)–(h)) for 30 fs (a,e); 200 fs, negative (b,f); 750 fs (c,g); and 1500 fs (d,h).

Appendix D

Hydroxyl Scavenging: Silver

D.1 Liquid Ammonia

[NH ₃] (mM)	pH	fractional yield of H ₂ O ₂
0		1.00 ± 0.00
0.0625	5.71	
0.125	6.74	
0.25	6.98	
0.375	7.18	
0.5	7.67	
0.75	8.42	
1	9.47	0.91 ± 0.16
2.5	9.85	
5	10.25	0.61 ± 0.04
10	10.62	0.71 ± 0.05
20	10.93	
50	11.19	0.42 ± 0.05
75	11.34	
100	11.42	0.34 ± 0.03

TABLE D.1: Solution pH and fractional concentrations of H₂O₂ for different liquid ammonia-containing precursors.

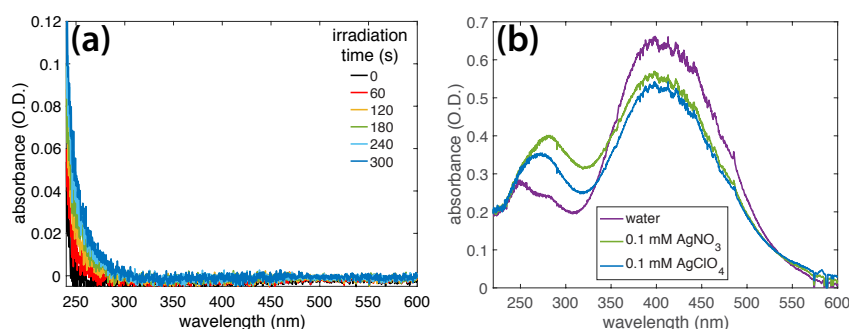


FIGURE D.1: For an AgNO₃ solution without NH₃ (a), in-situ spectra over time shows that no particles are formed in this solution. In panel (b), the (TiSO₄)/H₂O₂ spectra of AgNO₃ and AgClO₄ compared to a spectrum of just water irradiated under the same conditions. The fractional amount of H₂O₂ formed in the 0.1 mM AgNO₃ solution was 0.86 ± 0.11 and in the 0.1 mM AgClO₄ solution it was 0.85 ± 0.03.

$[\text{NH}_3]$ (mM)	pH	k (s^{-1})
0	5.71	
0.0625	7.12	0.026 ± 0.002
0.125	7.19	0.029 ± 0.007
0.25	8.13	0.02 ± 0.01
0.375	8.83	0.010 ± 0.007
0.5	8.93	0.0049 ± 0.0008
0.75	9.18	0.0040 ± 0.0008
1	9.53	0.0041 ± 0.0006
2.5	10.23	0.0038 ± 0.0007
5	10.51	0.0037 ± 0.0008
10	10.78	0.0040 ± 0.0006
20	10.96	0.0030 ± 0.0005
50	11.22	
75	11.36	
100	11.44	

TABLE D.2: All precursor solutions contained 0.1 mM AgNO_3 along with the indicated concentrations of NH_3 . The AgNP formation rate constant k , mirrored by the SPR-peak growth, is shown for samples in which AgNPs formed.

$[\text{NH}_3]$ (mM)	Ag salt	pH	k (s^{-1})
0	AgClO_4	6.67 ± 0.44	
0	AgNO_3	6.15 ± 0.14	
1	AgClO_4	9.71 ± 0.10	0.0033 ± 0.0004
1	AgNO_3	9.53 ± 0.14	0.0041 ± 0.0006

TABLE D.3: Solutions contained 0.1 mM of a particular silver salt, either AgClO_4 or AgNO_3 , and the indicated concentrations of NH_3 . The AgNP SPR growth rate constant k is shown where applicable, for samples in which AgNPs formed.

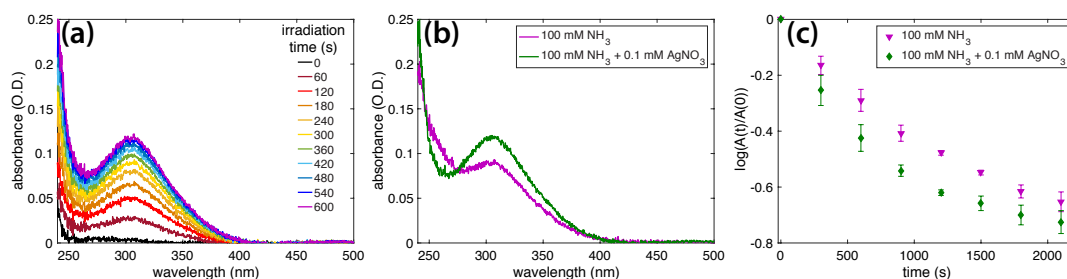


FIGURE D.2: Representative spectra of irradiated 100 mM NH_3 solutions, with (a) and without (b) silver. Average optical density (OD) after 600 s with no Ag is 0.09 ± 0.01 . With Ag, the average is 0.11 ± 0.02 . Comparative decay rates of the 302 nm peak over time are shown in panel (c).

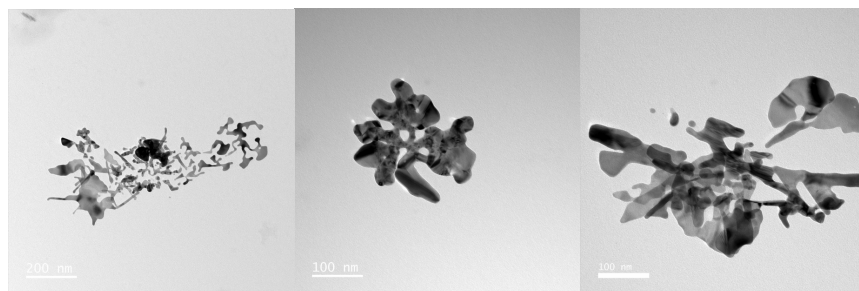


FIGURE D.3: A TEM image of AgNPs formed in 0.25 mM ammonia solution.

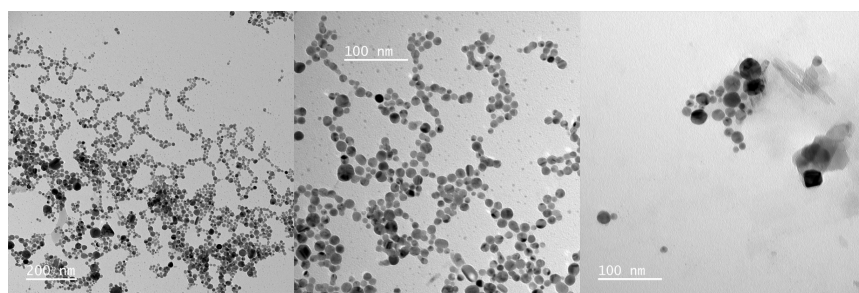


FIGURE D.4: A TEM image of AgNPs formed in 1 mM ammonia solution.

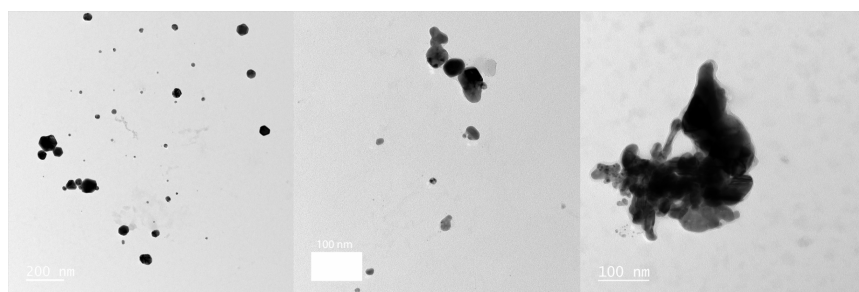


FIGURE D.5: A TEM image of AgNPs formed in 10 mM ammonia solution.

Appendix E

Hydroxyl Scavenging: Gold

E.1 Additional TEMs

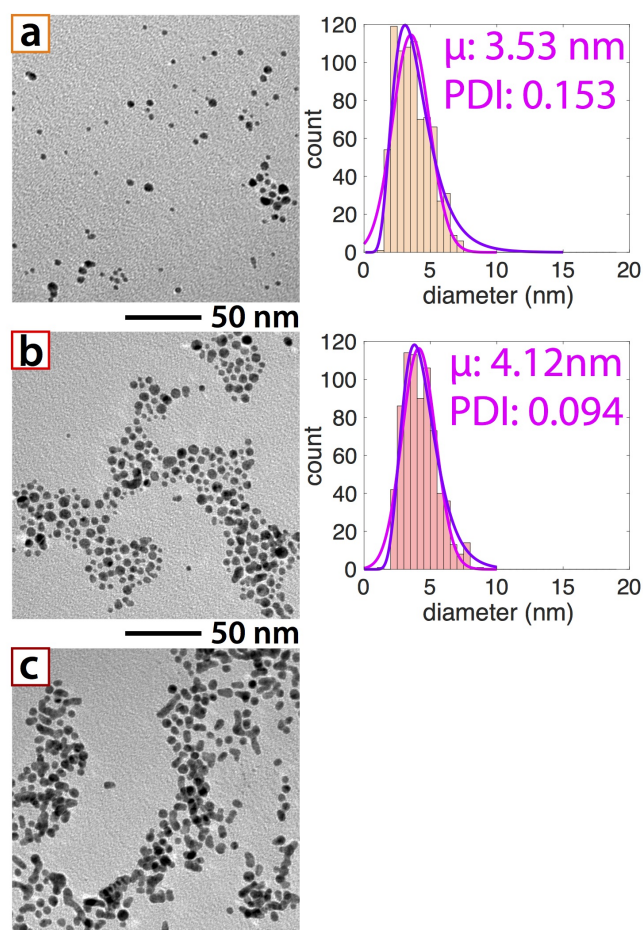


FIGURE E.1: Representative TEM images and corresponding size distributions of AuNPs synthesized using IPA; (a) 20 mM (b) 50 mM (c) 100 mM.

Size distribution analysis of samples produced with 100 mM IPA could not be analyzed with ImageJ because the NPs were agglomerated. Because the AuNPs synthesized under these conditions are catalytically active, it is likely that agglomeration is a result of TEM grid preparation.

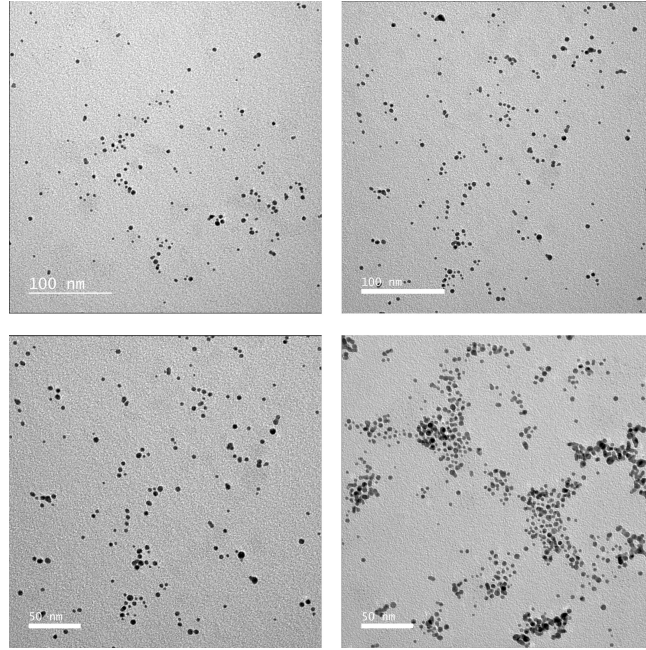


FIGURE E.2: Additional TEM images of gold products synthesized with 10 mM IPA.

The size distributions presented in these histograms, inferred from TEM images, were fitted to both a log-normal function and a Gaussian function using MATLAB. The PDI was computed as variance divided by the squared mean. For the Gaussian function, variance is expressed as σ^2 where σ is the standard deviation and mean¹ is μ . Thus, the PDI was computed as σ^2/μ^2 . For a log-normal function the mean is computed as $e^{\mu+\sigma^2/\mu^2}$ and variance is computed by $(e^{\sigma^2} - 1)(e^{2\mu+\sigma^2})$. The values marked with (*) are those reported on Figures 2 and 3 in the main work. The reported sample mean (\bar{x}) and PDI were selected taking into account both the R^2 values and the values that best fit the experimental mean obtained from the size distribution analysis of the TEM images.

mM	\bar{x} (nm)	PDI	R^2
0	3.42 ± 0.93	0.074	0.862
0.1	4.32 ± 2.17	0.252	0.840
1	4.81 ± 1.13	0.055*	0.980
10	3.78 ± 1.01	0.072*	0.900
20	3.53 ± 1.38	0.153*	0.831
50	4.12 ± 1.27	0.094*	0.925

TABLE E.1: Average particle dimensions obtained from Gaussian function-fitting to size distributions of AuNPs synthesized with IPA.

¹The mean and standard deviation of a population, or anyway the values symbolically represented in these equation, are symbolized with greek letters; however the sample values are expressed as \bar{x} for mean, and s_x for standard deviation.

mM	\bar{x} (nm)	PDI	R ²
0	3.76 ± 1.18	0.099*	0.931
0.1	5.41 ± 3.04	0.317*	0.949
1	5.05 ± 1.25	0.061	0.980
10	3.97 ± 1.10	0.077	0.938
20	3.97 ± 1.69	0.182	0.929
50	4.43 ± 1.46	0.108	0.962

TABLE E.2: Average particle dimensions obtained from log-normal function-fitting to size distributions of AuNPs synthesized with IPA.

mM	\bar{x} (nm)	PDI	R ²
0.05	3.73 ± 1.23	0.109	0.927
0.1	4.22 ± 1.98	0.221	0.828
1	5.02 ± 2.18	0.188	0.892
10	6.07 ± 1.60	0.069*	0.903

TABLE E.3: Average particle dimensions obtained from Gaussian function-fitting to size-distributions of AuNPs synthesized with acetate.

mM	\bar{x} (nm)	PDI	R ²
0.05	4.11 ± 1.50	0.133*	0.971
0.1	5.05 ± 2.59	0.262*	0.969
1	5.81 ± 2.81	0.233*	0.940
10	6.43 ± 1.66	0.067	0.847

TABLE E.4: Average particle dimensions obtained from log-normal function-fitting to size-distributions of AuNPs synthesized with acetate.

mM	\bar{x} (nm)	PDI	R ²
0.1	6.06 ± 3.14	0.269	0.783
1	3.41 ± 1.11	0.106	0.720

TABLE E.5: Average particle dimensions obtained from Gaussian function-fitting to size-distributions of AuNPs synthesized with KCl.

mM	\bar{x} (nm)	PDI	R ²
0.1	7.73 ± 4.84	0.392*	0.827
1	4.02 ± 1.62	0.162*	0.849

TABLE E.6: Average particle dimensions obtained from log-normal function-fitting to size-distributions of AuNPs synthesized with KCl.

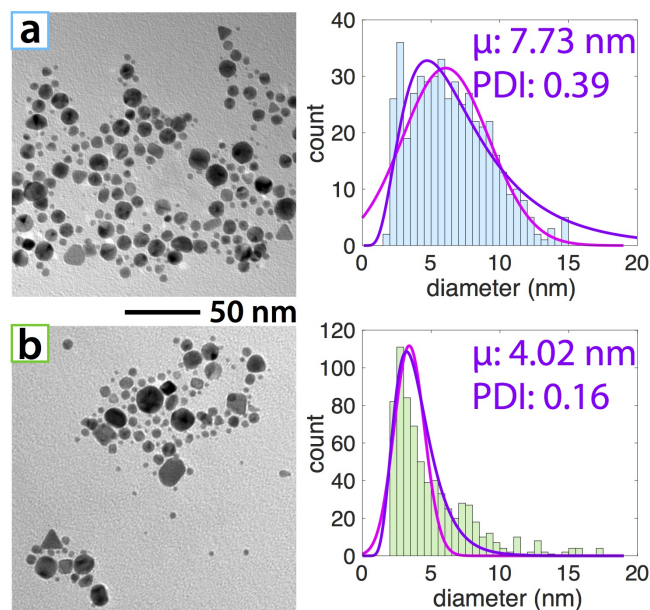


FIGURE E.3: Representative TEM images with corresponding size distributions of AuNPs synthesized with KCl: (a) 0.1 mM, (b) 10 mM.

E.2 XPS Data

species	no scavenger		10 mM IPA		10 mM acetate	
	E_B (eV)	% total	E_B (eV)	% total	E_B (eV)	% total
Au ⁰ (low)	83.48 ± 0.08	50 ± 7	83.57 ± 0.21	59 ± 1	83.58 ± 0.11	39 ± 5
Au ⁰	83.84 ± 0.03	41 ± 7	83.96 ± 0.20	36.4 ± 0.9	83.99 ± 0.05	56 ± 7
Au ⁺	85.92 ± 0.06	8.6 ± 0.3	86.01 ± 0.02	4.4 ± 0.2	86.00 ± 0.01	5 ± 2

TABLE E.7: Binding energy (E_B) and atomic percent of various species deconvoluted from XPS analysis. Assignments based on the binding energies reported in refs [175–177]. E_B is the binding energy in electron volts, and *low* indicates the low-coordination complex.

Determining the ratios of low-coordination Au helps approximate particle surface area, because low-coordinated Au is likely to be a surface atom.

element	no scavenger	10 mM IPA	10 mM acetate
	atomic %	atomic %	atomic %
C	45.5 ± 0.3	46 ± 10	37 ± 12
Au	26 ± 17	13.8 ± 0.7	34 ± 28
O	29 ± 17	40 ± 4	25 ± 12

TABLE E.8: Atomic percentages obtained by XPS for samples prepared with no scavenger, 10 mM IPA, and 10 mM acetate.

E.3 Rate Summaries

mM	k_1 (s^{-1})	k_2 ($M^{-1} s^{-1}$)	A_{max}	λ_{max} (nm)
0	0.0022(8)	0.14(2)	0.35(1)	530 ± 3
0.1	0.0024(7)	0.16(2)	0.330(7)	527 ± 4
1	0.0016(2)	0.07(1)	0.26(1)	516 ± 3
10	0.0013(3)	0.042(4)	0.23(1)	512 ± 4
20	0.0010(4)	0.029(4)	0.239(5)	513 ± 3
50	0.0008(3)	0.022(7)	0.242(3)	513 ± 1
100	0.0009(1)	0.021(3)	0.236(6)	517 ± 6

TABLE E.9: Kinetic data associated AuNP formation in IPA solutions.

mM	k_1 (s^{-1})	k_2 ($M^{-1} s^{-1}$)	A_{max}	λ_{max} (nm)
0	0.0022(8)	0.14(2)		
0.05	0.0018(5)	0.16(2)	0.350(9)	526 ± 1
0.1	0.004(1)	0.12(1)	0.353(8)	530 ± 2
1	0.004(1)	0.06(1)	0.31(1)	519 ± 2
10	0.0039(7)	0.054(8)	0.288(7)	520 ± 2
20	0.003(1)	0.062(6)	0.301(3)	520 ± 2
50	0.0031(3)	0.041(4)	0.29(2)	524 ± 1

TABLE E.10: Kinetic data associated AuNP formation in acetate solutions.

mM	k_1 (s^{-1})	k_2 ($M^{-1} s^{-1}$)	A_{max}	λ_{max} (nm)
0.1	0.0016(6)	0.14(2)	0.346(9)	530 ± 5
1	0.0004(2)	0.13(2)	0.359(14)	532 ± 2

TABLE E.11: Kinetic data associated with AuNP formation in KCl solutions.

E.4 Catalytic Data

mM	k_{app} (s^{-1})	k_1 ($\text{s}^{-1} \text{m}^{-2} \text{L}$)	k_{Au} ($\text{s}^{-1} \mu\text{mol}^{-1}$)	SSA ($\text{m}^2 \text{L}^{-1}$)
0	0.0047(6)	0.0037(23)	0.093(12)	1.25 ± 0.8
0.1	0.0052(3)	0.0045(23)	0.104(7)	1.16 ± 0.6
1	0.0078(10)	0.0065(21)	0.156(21)	1.20 ± 0.4
10	0.0109(8)	0.0069(18)	0.218(16)	1.58 ± 0.4
20	0.0089(9)	0.0054(20)	0.178(18)	1.63 ± 0.6
50	0.0088(11)	0.0062(20)	0.176(22)	1.42 ± 0.4
100	0.0106(10)		0.212(21)	

TABLE E.12: Catalytic data associated with IPA; k_{app} is the apparent rate of catalysis, and k_{SA} is the apparent rate normalized to the specific surface area (SSA). The apparent rate has also been normalized according to moles of Au, tabulated under k_{Au} .

mM	k_{app} (s^{-1})	k_1 ($\text{s}^{-1} \text{m}^{-2} \text{L}$)	k_{Au} ($\text{s}^{-1} \mu\text{mol}^{-1}$)	SSA ($\text{m}^2 \text{L}^{-1}$)
0.05	0.0049(7)	0.0036(21)	0.098(14)	1.36 ± 0.8
0.1	0.0040(6)	0.0033(17)	0.080(12)	1.19 ± 0.6
1	0.0046(5)	0.0041(17)	0.091(10)	1.12 ± 0.5
10	0.0066(9)	0.0063(21)	0.131(19)	1.04 ± 0.3

TABLE E.13: Catalytic data associated with AuNPs synthesized in acetate.

E.5 Hydrogen Peroxide

mM	IPA	acetate
0.05		0.96 ± 0.05
0.1	1.01 ± 0.04	0.94 ± 0.06
1	0.92 ± 0.07	0.86 ± 0.08
10	0.41 ± 0.16	0.53 ± 0.07
20	0.23 ± 0.04	0.38 ± 0.11
30	0.19 ± 0.03	0.35 ± 0.12
40	0.17 ± 0.03	
50	0.16 ± 0.04	
10	0.12 ± 0.02	
200	0.08 ± 0.02	

TABLE E.14: Fractional concentrations of H_2O_2 formed in water in the presence of IPA or acetate, after 180 seconds of irradiation at standard experimental conditions: $1000 \mu\text{J}$ pulse energy, 30 fs pulse duration. The concentration of H_2O_2 generated in pure water, unhindered by radical scavengers, was determined to be $1.21 \pm 0.12 \text{ mM}$, and it is set to '1'.

E.6 Solution-pH Effects

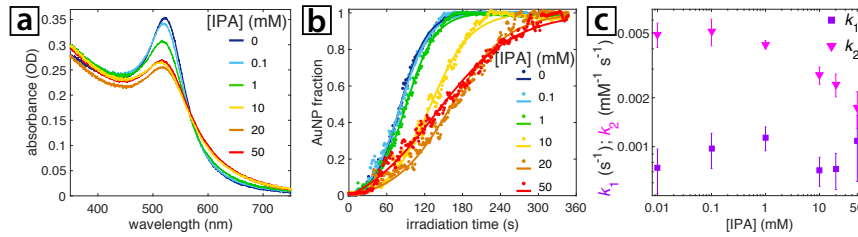


FIGURE E.4: Data for AuNPs synthesized at pH 5.3 (a) UV-vis spectra of final AuNP products, (b) Representative plots of fractional growth of AuNPs versus irradiation time and (c) obtained k_1 (purple circles) and k_2 (magenta triangles) for different concentrations of IPA.

Bibliography

- (1) Zhang, J. Z.; Noguez, C. *Plasmonics* **2008**, *3*, 127–150.
- (2) Dreaden, E. C.; Alkilany, A. M.; Huang, X.; Murphy, C. J.; El-Sayed, M. A. *Chem. Soc. Rev.* **2012**, *41*, 2740–2779.
- (3) Dreaden, E. C.; Mackey, M. A.; Huang, X.; Kang, B.; El-Sayed, M. A. *Chem. Soc. Rev.* **2011**, *40*, 3391–3404.
- (4) Bastús, N. G.; Comenge, J.; Puntès, V. *Langmuir* **2011**, *27*, 11098–11105.
- (5) Haynes, C. L.; McFarland, A. D.; Van Duyne, R. P. *Anal. Chem.* **2005**, *77*, 338–346.
- (6) Lepinay, S.; Staff, A.; Ianoul, A.; Albert, J. *Biosens. Bioelectron.* **2014**, *52*, 337–344.
- (7) Alkilany, A. M.; Lohse, S. E.; Murphy, C. J. *Acc. Chem. Res.* **2013**, *46*, 650–661.
- (8) Sztandera, K.; Gorzkiewicz, M.; Klajnert-Maculewicz, B. *Mol. Pharmaceutics* **2019**, *16*, 1–23.
- (9) Wu, X.; Jaatinen, E.; Sarina, S.; Zhu, H. Y. *J. Phys. D: Appl. Phys.* **2017**, *50*, 283001.
- (10) Mukherjee, S.; Libisch, F.; Large, N.; Neumann, O.; Brown, L. V.; Cheng, J.; Lassiter, J. B.; Carter, E. A.; Nordlander, P.; Halas, N. J. *Nano Lett.* **2013**, *13*, 240–247.
- (11) Linic, S.; Christopher, P.; Ingram, D. B. *Nat. Mater.* **2011**, *10*, 911–921.
- (12) Chopra, I. J. *Antimicrob. Chemoth.* **2007**, *59*, 587–590.
- (13) Rai, M.; Yadav, A.; Gade, A. *Biotechnol. Adv.* **2009**, *27*, 76–83.
- (14) Morones, J. R.; Elechiguerra, J. L.; Camacho, A.; Holt, K.; Kouri, J. B.; Ramírez, J. T.; Yacaman, M. J. *Nanotechnology* **2005**, *16*, 2346.
- (15) Xu, B.-B.; Ma, Z.-C.; Wang, L.; Zhang, R.; Niu, L.-G.; Yang, Z.; Zhang, Y.-L.; Zheng, W.-H.; Zhao, B.; Xu, Y.; Chen, Q.-D.; Xia, H.; Sun, H.-B. *Lab Chip* **2011**, *11*, 3347–3351.
- (16) Shin, Y.; Lee, C.; Yang, M.-S.; Jeong, S.; Kim, D.; Kang, T. *Sci. Rep.* **2014**, *4*.
- (17) Haruta, M.; Yamada, N.; Kobayashi, T.; Iijima, S. *J. Catal.* **1989**, *115*, 301–309.
- (18) Haruta, M. *Catal. Today* **1997**, *36*, Copper, Silver and Gold in Catalysis, 153–166.
- (19) Tai, Y.; Yamaguchi, W.; Tajiri, K.; Kageyama, H. *Appl. Catal., A* **2009**, *364*, 143–149.
- (20) Corma, A.; Garcia, H. *Chem. Soc. Rev.* **2008**, *37*, 2096–2126.
- (21) Qian, K.; Luo, L.; Bao, H.; Hua, Q.; Jiang, Z.; Huang, W. *Catal. Sci. Technol.* **2013**, *3*, 679–687.
- (22) Tangeysh, B.; Moore Tibbetts, K.; Odhner, J. H.; Wayland, B. B.; Levis, R. J. *J. Phys. Chem. C* **2013**, *117*, 18719–18727.
- (23) Ferreira, P. H. D.; Vivas, M. G.; Boni, L. D.; dos Santos, D. S.; Balogh, D. T.; Misoguti, L.; Mendonca, C. R. *Opt. Express* **2012**, *20*, 518–523.
- (24) Nakamura, T.; Mochidzuki, Y.; Sato, S. *J. Mater. Res.* **2008**, *23*, 968–974.
- (25) Odhner, J. H.; Moore Tibbetts, K.; Tangeysh, B.; Wayland, B. B.; Levis, R. J. *J. Phys. Chem. C* **2014**, *118*, 23986–23995.
- (26) Lu, W.-E.; Zheng, M.-L.; Chen, W.-Q.; Zhao, Z.-S.; Duan, X.-M. *Phys. Chem. Chem. Phys.* **2012**, *14*, 11930–11936.

- (27) Berciaud, S.; Cognet, L.; Tamarat, P.; Lounis, B. *Nano Lett.* **2005**, *5*, 515–518.
- (28) Male, K. B.; Li, J.; Bun, C. C.; Ng, S.-C.; Luong, J. H. T. *J. Phys. Chem. C* **2008**, *112*, 443–451.
- (29) Piella, J.; Bastús, N. G.; Puntès, V. *Chem. Mater.* **2016**, *28*, 1066–1075.
- (30) Wang, L.; Jiang, X.; Ji, Y.; Bai, R.; Zhao, Y.; Wu, X.; Chen, C. *Nanoscale* **2013**, *5*, 8384–8391.
- (31) Bartholomew, C. H. *eng Appl. Catal., A* **2001**, *212*, 17–60.
- (32) Casas, J.; Venkataramasubramani, M.; Wang, Y.; Tang, L. *Biosens. Bioelectron.* **2013**, *49*, 525–530.
- (33) Allen, J. M.; Xu, J.; Blahove, M.; Canonico-May, S. A.; Santaloci, T. J.; Braselton, M. E.; Stone, J. W. *eng J. Colloid Interface Sci.* **2017**, *505*, 1172–1176.
- (34) He, J.; Unser, S.; Bruzas, I.; Cary, R.; Shi, Z.; Mehra, R.; Aron, K.; Sagle, L. *eng Colloids Surf., B* **2018**, *163*, 140–145.
- (35) Smith, B. L.; Hutchison, J. E. *J. Phys. Chem. C* **2013**, *117*, 25127–25137.
- (36) Elliott, E. W.; Glover, R. D.; Hutchison, J. E. *ACS Nano* **2015**, *9*, 3050–3059.
- (37) Kandidov, V.; Kosareva, O.; Golubtsov, I.; Liu, W.; Becker, A.; Akozbek, N.; Bowden, C.; Chin, S. *Appl. Phys. B* **2003**, *77*, 149–165.
- (38) Stelmaszczyk, K.; Rohwetter, P.; Méjean, G.; Yu, J.; Salmon, E.; Kasparian, J.; Ackermann, R.; Wolf, J.-P.; Wöste, L. *Appl. Phys. Lett.* **2004**, *85*, 3977–3979.
- (39) Odhner, J. H.; McCole, E. T.; Levis, R. J. *J. Phys. Chem. A* **2011**, *115*, 13407–13412.
- (40) Shen, M.; Carey, J. E.; Crouch, C. H.; Kandyła, M.; Stone, H. A.; Mazur, E. *Nano Lett.* **2008**, *8*, 2087–2091.
- (41) Vitek, D. N.; Block, E.; Bellouard, Y.; Adams, D. E.; Backus, S.; Kleinfeld, D.; Durfee, C. G.; Squier, J. A. *Opt. Express* **2010**, *18*, 24673–24678.
- (42) Antkowiak, M.; Torres-Mapa, M. L.; Stevenson, D. J.; Dholakia, K.; Gunn-Moore, F. J. *Nat. Protoc.* **2013**, *8*, 1216–1233.
- (43) Linz, N.; Freidank, S.; Liang, X.-X.; Vogel, A. *Phys. Rev. B* **2016**, *94*, 024113.
- (44) Vogel, A.; Noack, J.; Hüttman, G.; Paltauf, G. *Appl. Phys. B* **2005**, *81*, 1015–1047.
- (45) Shen, Y. R., *The Principles of Nonlinear Optics*; Wiley: New York, 1984.
- (46) Sacchi, C. A. *J. Opt. Soc. Am. B* **1991**, *8*, 337–345.
- (47) Kennedy, P. K. *IEEE J. Quant. Electron.* **1995**, *31*, 2241–2249.
- (48) Noack, J.; Vogel, A. *IEEE J. Quant. Electron.* **1999**, *35*, 1156–1167.
- (49) Liu, W.; Kosareva, O.; Golubtsov, I.; Iwasaki, A.; Becker, A.; Kandidov, V.; Chin, S. *Appl. Phys. B* **2003**, *76*, 215–229.
- (50) Bergé, L.; Skupin, S.; Nuter, R.; Kasparian, J.; Wolf, J.-P. *Prog. Rep. Phys.* **2007**, *70*, 1633.
- (51) Sylvestre, J.-P.; Poulin, S.; Kabashin, A. V.; Sacher, E.; Meunier, M.; Luong, J. H. T. *J. Phys. Chem. B* **2004**, *108*, 16864–16869.
- (52) Zeng, H.; Du, X.-W.; Singh, S. C.; Kulinich, S. A.; Yang, S.; He, J.; Cai, W. *Adv. Funct. Mater.* **2012**, *22*, 1333–1353.
- (53) Zhang, D.; Gökce, B.; Barcikowski, S. *Chem. Rev.* **2017**, *117*, 3990–4103.
- (54) Boyer, P.; Meunier, M. *J. Phys. Chem. C* **2012**, *116*, 8014–8019.
- (55) Sylvestre, J.-P.; Kabashin, A.; Sacher, E.; Meunier, M. *Appl. Phys. A* **2005**, *80*, 753–758.
- (56) Rehbock, C.; Merk, V.; Gamrad, L.; Streubel, R.; Barcikowski, S. *Phys. Chem. Chem. Phys.* **2013**, *15*, 3057–3067.
- (57) Werner, D.; Furube, A.; Okamoto, T.; Hashimoto, S. *J. Phys. Chem. C* **2011**, *115*, 8503–8512.
- (58) Ziefuß, A. R.; Reichenberger, S.; Rehbock, C.; Chakraborty, I.; Gharib, M.; Parak, W. J.; Barcikowski, S. *J. Phys. Chem. C* **2018**, *122*, 22125–22136.

- (59) Kabashin, A. V.; Meunier, M.; Kingston, C.; Luong, J. H. T. *J. Phys. Chem. B* **2003**, *107*, 4527–4531.
- (60) Besner, S.; Kabashin, A. V.; Winnik, F. M.; Meunier, M. *J. Phys. Chem. C* **2009**, *113*, 9526–9531.
- (61) Essaidi, A.; Chakif, M.; Schops, B.; Aumman, A.; Xiao, S.; Esen, C.; Ostendorf, A. *English J. Laser Micro Nanoen.* **2013**, *8*, 131–136.
- (62) Rodrigues, C. J.; Bobb, J. A.; John, M. G.; Fisenko, S. P.; El-Shall, M. S.; Tibbetts, K. M. *Phys. Chem. Chem. Phys.* **2018**, *20*, 28465–28475.
- (63) Tibbetts, K. M.; Tangeysh, B.; Odhner, J. H.; Levis, R. J. *J. Phys. Chem. A* **2016**, *120*, 3562–3569.
- (64) Tangeysh, B.; Moore Tibbetts, K.; Odhner, J. H.; Wayland, B. B.; Levis, R. J. *Nano Lett.* **2015**, *15*, 3377–3382.
- (65) Tangeysh, B.; Tibbetts, K. M.; Odhner, J. H.; Wayland, B. B.; Levis, R. J. *Langmuir* **2017**, *33*, 243–252.
- (66) Zhao, C. J.; Qu, S. L.; Qiu, J. R.; Zhu, C. S. *J. Mater. Res.* **2003**, *18*, 1710–1714.
- (67) Nakamura, T.; Herbani, Y.; Ursescu, D.; Banici, R.; Dabu, R. V.; Sato, S. *AIP Adv.* **2013**, *3*, 082101.
- (68) Uwada, T.; Wang, S.-E.; Liu, T.-H.; Masuhara, H. *J. Photochem. Photobiol. A* **2017**, *346*, 177–186.
- (69) Meader, V. K.; John, M. G.; Rodrigues, C. J.; Tibbetts, K. M. *J. Phys. Chem. A* **2017**, *121*, 6742–6754.
- (70) Herbani, Y.; Nakamura, T.; Sato, S. *J. Colloid Interface Sci.* **2012**, *375*, 78–87.
- (71) Sarker, M. S. I.; Nakamura, T.; Herbani, Y.; Sato, S. *Appl. Phys. A* **2012**, *110*, 145–152.
- (72) Belmouaddine, H.; Shi, M.; Karsenti, P.-L.; Meesat, R.; Sanche, L.; Houde, D. *Phys. Chem. Chem. Phys.* **2017**, *19*, 7897–7909.
- (73) Nakashima, N.; Yamanaka, K.; Saeki, M.; Ohba, H.; Taniguchi, S.; Yatsushashi, T. *J. Photochem. Photobiol. A* **2016**, *319–320*, 70–77.
- (74) Xia, Y.; Xiong, Y.; Lim, B.; Skrabalak, S. E. *Angew. Chem. Int. Ed.* **2009**, *48*, 60–103.
- (75) Personick, M. L.; Mirkin, C. A. *J. Am. Chem. Soc.* **2013**, *135*, 18238–18247.
- (76) Papée, H. M.; Petriconi, G. L. *Nature* **1964**, *204*, 142.
- (77) Sreeja, S.; Venugopal Rao, S.; Radhakrishnan, P.; Tewari, S. P.; Prem Kiran, P. In *Proc. SPIE, SPIE LASE: San Francisco, California, USA, 2012*; Vol. 12, p 824718.
- (78) Sreeja, S.; Leela, C.; Kumar, V. R.; Bagchi, S.; Prashant, T. S.; Radhakrishnan, P.; Tewari, S. P.; Rao, S. V.; Kiran, P. P. *Laser Phys.* **2013**, *23*, 106002.
- (79) Milián, C.; Jarnac, A.; Brelet, Y.; Jukna, V.; Houard, A.; Mysyrowicz, A.; Couairon, A. *J. Opt. Soc. Am. B* **2014**, *31*, 2829–2837.
- (80) Kane, D. J.; Trebino, R. *IEEE J. Quant. Electron.* **1993**, *29*, 571–579.
- (81) Liu, W.; Petit, S.; Becker, A.; Aközbek, N.; Bowden, C.; Chin, S. *Opt. Commun.* **2002**, *202*, 189–197.
- (82) Oron, D.; Silberberg, Y. *Opt. Express* **2005**, *13*, 9903–9908.
- (83) Faccio, D.; Tamo šauskas, G.; Rubino, E.; Darginavi čius, J.; Papazoglou, D. G.; Tzortzakis, S.; Couairon, A.; Dubietis, A. *Phys. Rev. E* **2012**, *86*, 036304.
- (84) Minardi, S.; Gopal, A.; Tatarakis, M.; Couairon, A.; Tamošauskas, G.; Piskarskas, R.; Dubietis, A.; Trapani, P. D. *Opt. Lett.* **2008**, *33*, 86–88.
- (85) Minardi, S.; Gopal, A.; Couairon, A.; Tamošauskas, G.; Piskarskas, R.; Dubietis, A.; Trapani, P. D. *Opt. Lett.* **2009**, *34*, 3020–3022.
- (86) Besner, S.; Meunier, M. *J. Phys. Chem. C* **2010**, *114*, 10403–10409.
- (87) Wunder, S.; Polzer, F.; Lu, Y.; Mei, Y.; Ballauff, M. *J. Phys. Chem. C* **2010**, *114*, 8814–8820.

- (88) Eisenberg, G. *Ind. Eng. Chem. Anal. Ed.* **1943**, *15*, 327–328.
- (89) Huckaba, C. E.; Keyes, F. G. *J. Am. Chem. Soc.* **1948**, *70*, 1640–1644.
- (90) McBride, R. S. *J. Am. Chem. Soc.* **1912**, *34*, 393–416.
- (91) Belmouaddine, H.; Shi, M.; Sanche, L.; Houde, D. *Phys. Chem. Chem. Phys.* **2018**, *20*, 23403–23413.
- (92) Chin, S. L.; Lagacé, S. *Appl. Opt.* **1996**, *35*, 907–911.
- (93) Kurihara, K.; Kizling, J.; Stenius, P.; Fendler, J. H. *J. Am. Chem. Soc.* **1983**, *105*, 2574–2579.
- (94) Crowell, R. A.; Bartels, D. M. *J. Phys. Chem.* **1996**, *100*, 17940–17949.
- (95) Reuther, A.; Laubereau, A.; Nikogosyan, D. N. *J. Phys. Chem.* **1996**, *100*, 16794–16800.
- (96) Pommeret, S.; Gobert, F.; Mostafavi, M.; Lampre, I.; Mialocq, J.-C. *J. Phys. Chem. A* **2001**, *105*, 11400–11406.
- (97) Nikogosyan, D. N.; Oraevsky, A. A.; Rupasov, V. I. *Chem. Phys.* **1983**, *77*, 131–143.
- (98) Keldysh, L. *Sov. Phys. JETP* **1965**, *20*, 1307–1314.
- (99) Couairon, A.; Mysyrowicz, A. *Phys. Rep.* **2007**, *441*, 47–189.
- (100) Chin, S. L., *Femtosecond Laser Filamentation; Atomic, Optical, and Plasma Physics* 55; Springer: 2010.
- (101) Marburger, J. *Prog. Quant. Elec.* **1975**, *4*, 35–110.
- (102) Brodeur, A.; Chin, S. L. *Phys. Rev. Lett.* **1998**, *80*, 4406–4409.
- (103) Besner, S.; Kabashin, A. V.; Meunier, M. *Appl. Phys. Lett.* **2006**, *89*, 233122.
- (104) Besner, S.; Kabashin, A.; Meunier, M. *Appl. Phys. A* **2007**, *88*, 269–272.
- (105) Fan, C.-H.; Longtin, J. P. *Appl. Opt.* **2001**, *40*, 3124–3131.
- (106) Fan, C. H.; Sun, J.; Longtin, J. P. *J. Appl. Phys.* **2002**, *91*, 2530–2536.
- (107) Efimenko, E. S.; Malkov, Y. A.; Murzanev, A. A.; Stepanov, A. N. *J. Opt. Soc. Am. B* **2014**, *31*, 534–541.
- (108) Elles, C. G.; Jailaubekov, A. E.; Crowell, R. A.; Bradforth, S. E. *J. Chem. Phys.* **2006**, *125*, 044515.
- (109) Linz, N.; Freidank, S.; Liang, X.-X.; Vogelmann, H.; Trickl, T.; Vogel, A. *Phys. Rev. B* **2015**, *91*, 134114.
- (110) Sykora, S. Dawson Integral Approximations., DOI: 10.3247/SL4Soft12.001, 2012.
- (111) Sarpe, C.; Köhler, J.; Winkler, T.; Wollenhaupt, M.; Baumert, T. *New J. Phys.* **2012**, *14*, 075021.
- (112) Docchio, F. *Europhys. Lett.* **1988**, *6*, 407.
- (113) LaMer, V. K.; Dinegar, R. H. *J. Am. Chem. Soc.* **1950**, *72*, 4847–4854.
- (114) Yan, H.; Cingarapu, S.; Klabunde, K. J.; Chakrabarti, A.; Sorensen, C. M. *Phys. Rev. Lett.* **2009**, *102*, 095501.
- (115) Turkevich, J.; Stevenson, P. C.; Hillier, J. *Discuss. Faraday Soc.* **1951**, *11*, 55–75.
- (116) Takiyama, K. *Bull. Chem. Soc. Jpn.* **1958**, *31*, 944–950.
- (117) Esumi, K.; Hosoya, T.; Suzuki, A.; Torigoe, K. *Langmuir* **2000**, *16*, 2978–2980.
- (118) Finney, E. E.; Finke, R. G. *J. Colloid Interface Sci.* **2008**, *317*, 351–374.
- (119) Tatarchuk, V. V.; Sergievskaya, A. P.; Druzhinina, I. A.; Zaikovskiy, V. I. *J. Nanopart. Res.* **2011**, *13*, 4997–5007.
- (120) Streszewski, B.; Jaworski, W.; Paclawski, K.; Csapó, E.; Dékány, I.; Fitzner, K. *Colloids Surf., A* **2012**, *397*, 63–72.
- (121) Shields, S. P.; Richards, V. N.; Buhro, W. E. *Chem. Mater.* **2010**, *22*, 3212–3225.
- (122) Njoki, P. N.; Luo, J.; Kamundi, M. M.; Lim, S.; Zhong, C.-J. *Langmuir* **2010**, *26*, 13622–13629.
- (123) Watzky, M. A.; Finke, R. G. *J. Am. Chem. Soc.* **1997**, *119*, 10382–10400.
- (124) Haiss, W.; Thanh, N. T. K.; Aveyard, J.; Fernig, D. G. *Anal. Chem.* **2007**, *79*, 4215–4221.

- (125) Behar, D.; Rabani, J. *J. Phys. Chem. B* **2006**, *110*, 8750–8755.
- (126) Zayats, M.; Baron, R.; Popov, I.; Willner, I. *Nano Lett.* **2005**, *5*, 21–25.
- (127) McGilvray, K. L.; Granger, J.; Correia, M.; Banks, J. T.; Scaiano, J. C. *Phys. Chem. Chem. Phys.* **2011**, *13*, 11914–11918.
- (128) Wu, H.; Xu, X.; Ge, X.; Zhang, Z. *Radiat. Phys. Chem.* **1997**, *50*, 585–588.
- (129) He, D.; Garg, S.; Waite, T. D. *Langmuir* **2012**, *28*, 10266–10275.
- (130) Nakamura, T.; Magara, H.; Herbani, Y.; Sato, S. *Appl. Phys. A* **2011**, *104*, 1021.
- (131) Herbani, Y.; Nakamura, T.; Sato, S. *J. Phys. Conf. Ser.* **2017**, *817*, 012048.
- (132) Du, B. D.; Phu, D. V.; Duy, N. N.; Lan, N. T. K.; Lang, V. T. K.; Thanh, N. V. K.; Phong, N. T. P.; Hien, N. Q. *J. Exp. Nanosci.* **2008**, *3*, 207–213.
- (133) Zeng, H.; Zhao, C.; Qiu, J.; Yang, Y.; Chen, G. *J. Cryst. Growth* **2007**, *300*, 519–522.
- (134) Abid, J. P.; Wark, A. W.; Brevet, P. F.; Girault, H. H. *Chem. Commun.* **2002**, 792–793.
- (135) Du, B. D.; Phu, D. V.; Duy, N. N.; Lan, N. T. K.; Lang, V. T. K.; Thanh, N. V. K.; Phong, N. T. P.; Hien, N. Q. *J. Exp. Nanosci.* **2008**, *3*, 207–213.
- (136) Meader, V. K.; John, M. G.; Frias Batista, L. M.; Ahsan, S.; Tibbetts, K. M. *Molecules* **2018**, *23*, accepted; in press.
- (137) Mao, S.; Quéré, F.; Guizard, S.; Mao, X.; Russo, R.; Petite, G.; Martin, P. *Appl. Phys. A* **2004**, *79*, 1695–1709.
- (138) Goia, D.; Matijević, E. *Colloids Surf., A* **1999**, *146*, 139–152.
- (139) Wang, C.-H.; Liu, C.-J.; Wang, C.-L.; Chien, C.-C.; Hwu, Y.; Liu, R.-S.; Yang, C.-S.; Je, J.-H.; Lin, H.-M.; Margaritondo, G. *Appl. Phys. A* **2009**, *97*, 295–300.
- (140) Ni, W.; Kou, X.; Yang, Z.; Wang, J. *ACS Nano* **2008**, *2*, 677–686.
- (141) LaVerne, J. A.; Pimblott, S. M. *J. Phys. Chem.* **1991**, *95*, 3196–3206.
- (142) Gonzalez, M. C.; Braun, A. M. *Res. Chem. Intermed.* **1995**, *21*, 837–859.
- (143) Zepp, R. G.; Hoigne, J.; Bader, H. *Environ. Sci. Technol.* **1987**, *21*, 443–450.
- (144) Rémita, S.; Mostafavi, M.; Delcourt, M. O. *J. Phys. Chem.* **1996**, *100*, 10187–10193.
- (145) Texier, I.; Rémita, S.; Archirel, P.; Mostafavi, M. *J. Phys. Chem.* **1996**, *100*, 12472–12476.
- (146) Ershov, B. G.; Henglein, A. *J. Phys. Chem. B* **1998**, *102*, 10663–10666.
- (147) McGilvray, K. L.; Fasciani, C.; Bueno-Alejo, C. J.; Schwartz-Narbonne, R.; Scaiano, J. C. *Langmuir* **2012**, *28*, 16148–16155.
- (148) Saion, E.; Gharibshahi, E.; Naghavi, K. *English International Journal of Molecular Sciences* **2013**, *14*, Copyright - Copyright MDPI AG 2013; Last updated - 2018-10-05, 7880–7896.
- (149) Goia, D. V. *J. Mater. Chem.* **2004**, *14*, 451–458.
- (150) Hughes, M. N.; Nicklin, H. G. *J. Chem. Soc. A* **1968**, 450–452.
- (151) Edwards, J. O.; Plumb, R. C. In *Progress in Inorganic Chemistry*; John Wiley & Sons, Inc.: 1994; Chapter The Chemistry of Peroxonitrites, pp 599–635.
- (152) Getoff, N. *Radiat. Phys. Chem.* **1996**, *47*, 581–593.
- (153) Huang, L.; Li, L.; Dong, W.; Liu, Y.; Hou, H. *Environ. Sci. Technol.* **2008**, *42*, 8070–8075.
- (154) Wang, J.; Song, M.; Chen, B.; Wang, L.; Zhu, R. *Chemosphere* **2017**, *184*, 1003–1011.
- (155) Plumb, R. C.; Edwards, J. O. *J. Phys. Chem.* **1992**, *96*, 3245–3247.
- (156) Mahoney, L. R. *J. Am. Chem. Soc.* **1970**, *92*, 5262–5263.
- (157) Pagsberg, P. In *Aspects of Research at Risø*; Aspects of Research at Riso: 1972, pp 209–222.
- (158) Dey, G. *Radiat. Phys. Chem.* **2011**, *80*, 394–402.

- (159) Rigg, T.; Scholes, G.; Weiss, J. *J. Chem. Soc.* **1952**, 3034–3038.
- (160) Maurer, P.; Thomas, C. F.; Kissner, R.; Rügger, H.; Greter, O.; Röthlisberger, U.; Koppenol, W. H. *J. Phys. Chem. A* **2003**, *107*, 1763–1769.
- (161) Merényi, G.; Lind, J.; Goldstein, S.; Czapski, G. *J. Phys. Chem. A* **1999**, *103*, 5685–5691.
- (162) Thøgersen, J.; Kissner, R.; Nauser, T.; Koppenol, W. H.; Richter, B.; Jensen, F.; Keiding, S. R.; Jensen, S. J. K. *Chem. Phys. Lett.* **2015**, *641*, 187–192.
- (163) Goldstein, S.; Rabani, J. *J. Am. Chem. Soc.* **2007**, *129*, 10597–10601.
- (164) Staehelin, J.; Hoigne, J. *Environ. Sci. Technol.* **1982**, *16*, 676–681.
- (165) Crittenden, J. C.; Hu, S.; Hand, D. W.; Green, S. A. *Water Research* **1999**, *33*, 2315–2328.
- (166) Barker, G. C.; Fowles, P.; Stringer, B. *Trans. Faraday Soc.* **1970**, *66*, 1509–1519.
- (167) Leopold, N.; Lendl, B. *J. Phys. Chem. B* **2003**, *107*, 5723–5727.
- (168) Li, Y.; Wu, Y.; Ong, B. S. *J. Am. Chem. Soc.* **2005**, *127*, 3266–3267.
- (169) Radi, R.; Beckman, J. S.; Bush, K. M.; Freeman, B. A. *J. Biol. Chem.* **1991**, *266*, 4244.
- (170) Goldstein, S.; Lind, J.; Merényi, G. *Chem. Rev.* **2005**, *105*, 2457–2470.
- (171) Zhu, X.; Castleberry, S. R.; Nanny, M. A.; Butler, E. C. *Environ. Sci. Technol.* **2005**, *39*, 3784–3791.
- (172) Mack, J.; Bolton, J. R. *J. Photoch. Photobio. A* **1999**, *128*, 1–13.
- (173) Hughes, M. N.; Nicklin, H. G.; Sackrle, W. A. C. *J. Chem. Soc. A* **1971**, 3722–3725.
- (174) D'Souza, J. S.; Dharmadhikari, J. A.; Dharmadhikari, A. K.; Rao, B. J.; Mathur, D. *Phys. Rev. Lett.* **2011**, *106*, 118101.
- (175) Heimann, P.; van der Veen, J.; Eastman, D. *Sol. Stat. Commun.* **1981**, *38*, 595–598.
- (176) Weststrate, C.; Lundgren, E.; Andersen, J.; Rienks, E.; Gluhoi, A.; Bakker, J.; Groot, I.; Nieuwenhuys, B. *Surf. Sci.* **2009**, *603*, 2152–2157.
- (177) Klyushin, A. Y.; Rocha, T. C. R.; Hävecker, M.; Knop-Gericke, A.; Schlögl, R. *Phys. Chem. Chem. Phys.* **2014**, *16*, 7881–7886.
- (178) Aditya, T.; Pal, A.; Pal, T. *Chem. Commun.* **2015**, *51*, 9410–9431.
- (179) Gu, S.; Kaiser, J.; Marzun, G.; Ott, A.; Lu, Y.; Ballauff, M.; Zacccone, A.; Barcikowski, S.; Wagener, P. *Catal. Lett.* **2015**, *145*, 1105–1112.
- (180) Hervés, P.; Pérez-Lorenzo, M.; Liz-Marzán, L. M.; Dzubielia, J.; Lu, Y.; Ballauff, M. *Chem. Soc. Rev.* **2012**, *41*, 5577.
- (181) Simakin, A. V.; Astashev, M. E.; Baimler, I. V.; Uvarov, O. V.; Voronov, V. V.; Vedunova, M. V.; Sevost'yanov, M. A.; Belosludtsev, K. N.; Gudkov, S. V. *J. Phys. Chem. B* **2019**, *123*, 1869–1880.
- (182) Ervens, B.; Gligorovski, S.; Herrmann, H. *Phys. Chem. Chem. Phys.* **2003**, *5*, 1811–1824.
- (183) Al-Sheikhly, M.; Hussmann, M.; McLaughlin, W. *Radiat. Phys. Chem.* **1988**, *32*, 545–551.
- (184) Dey, G. R.; El Omar, A. K.; Jacob, J. A.; Mostafavi, M.; Belloni, J. *J. Phys. Chem. A* **2011**, *115*, 383–391.
- (185) Harada, M.; Kizaki, S. *Cryst. Growth Des.* **2016**, *16*, 1200–1212.
- (186) Baxendale, J. H.; Wardman, P. *J. Chem. Soc., Faraday Trans. 1* **1973**, *69*, 584–594.
- (187) Zamborini, F. P.; Gross, S. M.; Murray, R. W. *Langmuir* **2001**, *17*, 481–488.
- (188) Zhang, H.; Jin, M.; Xiong, Y.; Lim, B.; Xia, Y. *Accounts of Chemical Research* **2013**, *46*, 1783–1794.
- (189) Chen, A.; Holt-Hindle, P. *Chemical Reviews* **2010**, *110*, 3767–3804.
- (190) Chen, X.; Liu, L.; Huang, F. *Chem. Soc. Rev.* **2015**, *44*, 1861–1885.

- (191) Wu, W.; Wu, Z.; Yu, T.; Jiang, C.; Kim, W.-S. *Sci. Technol. Adv. Mater.* **Apr.** **2015**, *16*, DOI: [10.1088/1468-6996/16/2/023501](https://doi.org/10.1088/1468-6996/16/2/023501).
- (192) Sun, C.; Li, H.; Chen, L. *Energy Environ. Sci.* **2012**, *5*, 8475–8505.
- (193) Gawande, M. B.; Goswami, A.; Felpin, F.-X.; Asefa, T.; Huang, X.; Silva, R.; Zou, X.; Zboril, R.; Varma, R. S. *Chemical Reviews* **2016**, *116*, 3722–3811.
- (194) Raspolli Galletti, A. M.; Antonetti, C.; Marracci, M.; Piccinelli, F.; Tellini, B. *Appl. Surf. Sci.* **2013**, *280*, 610–618.
- (195) Das, D.; Nath, B. C.; Phukon, P.; Dolui, S. K. *Colloids and Surfaces B: Biointerfaces* **2013**, *101*, 430–433.
- (196) Knight, M. W.; King, N. S.; Liu, L.; Everitt, H. O.; Nordlander, P.; Halas, N. J. *ACS Nano* **2014**, *8*, 834–840.
- (197) Kumar, S. G.; Rao, K. S. R. K. *RSC Adv.* **2015**, *5*, 3306–3351.
- (198) Byrnes, S.; Wyatt, A. Frequency Resolved Optical Gating., MATLAB File Exchange, (accessed 2012).
- (199) Kane, D. J. *IEEE J. Quant. Electron.* **1999**, *35*, 421–431.

Vita

Victoria Kathryn Meader was born on Keesler Air Force Base in Biloxi, Mississippi, on July 18, 1989—ten days before relocating to Montana. She is an American and an Irish citizen. She graduated from Virginia Commonwealth University in 2011 with a bachelor of arts in analytical philosophy, and a minor in French; after which she taught English for a year in Bretagne. She graduated again from VCU in 2017 with a bachelor of science in chemistry, and began pursuing a master's degree while assisting research in Dr. Katharine Tibbetts' lab.